ANGIOGRAPHY AND MONITORING OF HEMODYNAMIC SIGNALS IN THE BRAIN VIA OPTICAL COHERENCE TOMOGRAPHY

by

Alana M. Soehartono

A Thesis Submitted in

Partial Fulfillment of the

Requirements for the Degree of

Master of Science

in Engineering

at

The University of Wisconsin-Milwaukee

December 2013

ABSTRACT

ANGIOGRAPHY AND MONITORING OF HEMODYNAMIC SIGNALS IN THE BRAIN VIA OPTICAL COHERENCE TOMOGRAPHY

by

Alana M. Soehartono

The University of Wisconsin-Milwaukee, 2013
Under the Supervision of Professor Ramin Pashaie

The brain is a complex network of interconnected neurons with each cell functioning as a nonlinear processing unit. Neural responses to stimulus can be described by activity in neurons. While blood flow changes have been associated with neural activity and are critical to brain function, this neurovascular coupling is not well understood. This work presents a technique for neurovascular interrogation, combining optogenetics and optical coherence tomography.

Optogenetics is a recently developed neuromodulation technique to control activity in the brain using light with precise spatial neuronal control and high temporal resolution. Using this method, cells act as light-gated ion channels and respond to photo stimulation by increasing or decreasing activity. Spectral-domain optical coherence tomography (SD-OCT) is a noninvasive imaging modality that has the ability to image millimeter range depth and with micrometer resolution. SD-OCT

has been shown to image rodent cortical microvasculature *in-vivo* and detect hemodynamic changes in blood vessels. Our proposed system combines optogenetics and SD-OCT to image cortical patches of the brain with the capability of simultaneously stimulating the brain. The combination allows investigation of the hemodynamic changes in response to neural stimulation. Our results detected changes in blood vessel diameter and velocity before, during and after optogenetic stimulation and is presented.

For my parents

TABLE OF CONTENTS

1. Introduction and Background 1
1.1 Motivation 2
1.2 Biological Overview of Neurons 4
1.3 Optogenetics 4
1.3.1 Light Delivery Methods 7
1.4 Fluorescence Microscopy 9
1.5 Optical Coherence Tomography 11
1.5.1 Time-Domain Optical Coherence Tomography 17
1.5.2 Fourier-Domain Optical Coherence Tomography 18
1.5.3 Doppler Optical Coherence Tomography 21

2. Principles of Optical Coherence Tomography 24
2.1 Theory of OCT 24
2.2 Spectral Domain Low Coherence Interferometry 28
2.3 Doppler OCT 29
2.4 Imaging Resolution 30
2.4.1 Axial Resolution 31
2.4.2 Lateral Resolution 32
2.5 Imaging Range 34

3. System Design: Hardware 39
3.1 Source 40
3.2 Interferometer 44
3.3 Sample Arm 46
3.3.1 OCT Scanning Path 46
3.3.1.1 Scanning Relay 48
3.3.1.2 Sample Arm Optics 50
3.3.2 Optogenetic Stimulation Path 52
3.3.3 Fluorescent Microscopy Path 53

3.4 Reference Arm 55
3.5 Detection Arm 56
3.5.1 Spectrometer Design 57
3.5.2 Diffraction Grating 61
3.5.3 Detector 62
3.5.4 Detection Optics 63
3.5.5 Data Acquisition 64
3.6 System Implementation 64

4. System Design: Software and Signal Processing 67
4.1 Pre-Processing 67
4.2 Wavelength to Pixel Mapping 69
4.3 Motion Compensation 70
4.4 Angiography 71
4.5 Doppler OCT 74
4.6 LabVIEW Software 77

5. System Design: Image Enhancement and Analysis 80
5.1 Shadow Removal 80
5.2 Artifact Removal 85
5.3 Depth Color-Coded Maximum Intensity Projection 86
5.4 Velocity and Flow Analysis 87

6. Experimental Results and Analysis 91
6.1 Animal Protocols 92
6.2 OCT Scanning Protocols 93
6.3 Optogenetic Experiments with a Rat 95
6.3.1 Doppler OCT and Angiography Imaging with Optogenetics 96
6.4 Transgenic Mouse Results 100
6.4.1 Mouse 1 Results 103
6.4.2 Mouse 4 Results 105

7. Future Work and Conclusion 116

LIST OF FIGURES

Figure 1 - (Left) Na^- ions entering the membrane through the ion channel, while K^+ ions exit when the cell is stimulated with blue light (470 nm). (Right) Chloride ions being transported through an ion pump when the cell is stimulated with yellow light (580 nm). Figure adapted from [7]. 5

Figure 2 - Activation spectra for ChR2 and NpHR, separated by 100 nm. Figure adapted from [8] 6

Figure 3 - Excitation and inhibition of spike trains based on blue and yellow light pulses. Figure adapted from [8] 7

Figure 4 – (Left) Drawing of an optical fiber implantation on the cortical surface of a mouse, and (Right) the actual implementation. Figure adapted from [7]. 8

Figure 5 - Jablonski diagram of a photon excited to a higher state, and its transitional period to ground state, resulting in the emission of light. Figure adapted from [11]. 10

Figure 6 - Schematic of a Michelson interferometer 12

Figure 7 - (Left) A-scan, or depth profile, (Middle) B-scan or cross-sectional image and (Right) C-scan or a volumetric image acquired from an OCT scan. Figure adapted from [12]. 14

Figure 8 - (Left) Alevoli structure in a rat lung. (Right) Angiogram of a cortical patch of a mouse brain. Both images are produced with the OCT system developed for the project. 15

Figure 9 - Comparison of imaging systems resolution and penetration depth range, scaled logarithmically. OCT fills the gap in imaging with micrometer resolution 16

Figure 10 - Schematic of a time-domain OCT system 18

Figure 11 - Schematic of a spectral-domain OCT system. 20

Figure 12 - Schematic of a Doppler OCT system..... 22

Figure 13 - Depiction of frequency shift caused by moving particles for Doppler OCT velocity measurement..... 30

Figure 14 – Inversely proportional relationship between OCT axial resolution and source bandwidth of a system..... 32

Figure 15 – Inversely proportional relationship between lateral resolution and depth of field 33

Figure 16 – The effects of numerical aperture in relation to the beam spot size and depth of field. 34

Figure 17 - Relationship between spectral range captured and imaging range in the spatial domain. 36

Figure 18 - Schematic of the designed SD-OCT system. 38

Figure 19 - Absorption coefficient in biological constituents [16]..... 40

Figure 20 - Combined channel emission of the extended broadband SLD source. Figure adapted from [20]. 42

Figure 21- Beam spot size in relation to collimated beam spot size 48

Figure 22 – Schematic of sample arm optics and spatial resolution relations..... 50

Figure 23 - Transmission profile of dichroic filter MD515, reflection band = 490 – 510 nm and transmission band = 520 – 700 nm. Figure adapted from [10]. 52

Figure 24 - Schematic of a fluorescent microscope..... 53

Figure 25 - Schematic of the reference arm. 55

Figure 26 - Schematic of the spectrometer in the system. 57

Figure 27 - Transmission diffraction grating. 58

Figure 28- Maximum imaging depth for a detector with 1024 pixels. 60

Figure 29 - Efficiency versus wavelength for the diffraction grating. Figure adapted from [22]. 61

Figure 30 - Typical quantum efficiency of the line CCD camera. Figure adapted from [23]. 62

Figure 31 - OCT system during an optogenetic experiment in surgery bay. 64

Figure 32 - Signal processing chain for SD-OCT images 67

Figure 33 - λ-Pixel Mapping 69

Figure 34 - Angiography processing flow chart 72

Figure 35 - LabVIEW interface of the developed OCT software. 77

Figure 36 - (A, top left) Original angiogram image (B, top right) Deshadowed with *n* = 0.3 and a clipping limit of 0.04 (C, bottom left) Deshadowed with *n* = 0.03, with the same clipping limit and the final image is taken to the 0.5^{th} power. (D, bottom right) Deshadowed with *n* = 0.8, with minimal deshadowing. 81

Figure 37 - Corresponding lateral A-scan for images in Fig. 35 from the same location. 82

Figure 38 – Comparison of original (left) and deshadowed (right) angiogram. 83

Figure 39 - (A, left) original (B, middle) deshadowed n = 0.28 (C, right) deshadowed n = 0.6, both with thresh = 0.05 84

Figure 40 - Comparison of vertical artifact movement correction with varying radius size. 85

Figure 41 - Depth color-coded maximum intensity projection 86

Figure 42 - (Top) Vessel map and (Bottom) velocity line profile of the vessel, indicated by the red line across the vessel. 87

Figure 43 - Vessel map of a mouse brain scan 88

Figure 44 - Velocity line profile for the vessel circled in red. 89

Figure 45 - OCT scan head titlted at an angle for Doppler scanning. 94

Figure 46 - Bright-field image of the 2 x 2 mm cranial region. 95

Figure 47 – (Top) 3D angiogram of the rodent brain surface (Bottom) Cross-sectional OCT image of the cortical surface. 96

Figure 48 - Vessel map of Doppler image. 97

Figure 49 - Velocity line profile for Vessel 1. 98

Figure 50 - Velocity line profile of Vessel 5. 99

Figure 51 - Angiogram, Doppler velocity image and overlaid image of the two. 100

Figure 52 – Bright-field observations for (Left) pre-stimulus and (Right) intra-stimulus. 101

Figure 53- The sequential process of generating angiograms, (A) A cross-sectional angiogram (B) A set of angiograms (C) Volumetric rendering of the set of angiograms. 102

Figure 54 - Sample of a 2D scan path, indicated by the red line, for Doppler imaging. 103

Figure 55 - 3D angiogram projection (left) pre-stimulus and (right) post-stimulus. 105

Figure 56 - 3D blood flow projection (left) pre-stimulus and (right) post-stimulus. 105

Figure 57 - (Left) Bright-field image and (Right) overlaid OCT and velocity image. 106

Figure 58 - Microscope image of the cortical patch. The red box indicates the 2 mm x 2mm OCT field of view. 107

Figure 59 - Comparison of Recording 2 and 3 of pre-, intra- and post-stimulus data. 109

Figure 60 - Angiogram and Doppler-angiogram overlay for pre-, intra- and post-stimulus. 110

Figure 61 - Diameter change ratio in the main MCA 111

Figure 62 - Diameter changes in branch 1 of MCA. 112

Figure 63 - Diameter changes in the MCA branch 2 113

Figure 64 - Changes in flow and velocity for the vessel circled in red on the vessel map..... 114

Figure 65 - Changes in flow and velocity for the vessel circled in red on the vessel map..... 115

LIST OF ABBREVIATIONS

1D – One-dimensional

2D – Two-dimensional

3D – Three-dimensional

A-Line/A-Scan – Axial Line/Axial Scan

B-Scan – Cross-sectional Scan

CCD – Charge-Couple Device

ChR2 – Channelrhodopsin-2

Cl^- - Chloride Ions

CMOS – Complementary Metal-Oxide-Semiconductor

C-Scan – Volumetric Scan

DAC – Data Acquisition Card

deoxy-Hb – Deoxygenated Hemoglobin

D-OCT – Doppler Optical Coherence Tomography

EcOG – Electrocorticography

EEG – Electroencephalography

FC/APC – Fiber Connectors with Angled Physical Contact

fMRI – Functional Magnetic Resonance Imaging

fNIRS – Functional Near-Infrared Spectroscopy

FWHM – Full Width at Half Maximum

H_2O – Water

HbO_2 – Oxygenated Hemoglobin

InGaAs – Indium Gallium Arsenide

IR – Infrared

LED – Light Emitting Diode

LED – Light-emitting Diode

MEMS – Microelectromechanical Systems

MRI – Magnetic Resonance Imaging

NA – Numerical Aperture

Na^+ - Sodium Ions

NpHR – Halorhodopsin

PET – Positron Emission Tomography

PR-DOCT – Phase-Resolved Doppler Optical Coherence Tomography

SD-OCT – Spectral-Domain Optical Coherence Tomography

SLD – Superluminescent Diode

SNR – Signal-to-Noise Ratio

SS-OCT – Swept Source Optical Coherence

Tomography

STFFT – Short Time Fast Fourier Transform

TD-OCT – Time-Domain Optical Coherence Tomography

YFP – Yellow Fluorescent Protein

ACKNOWLEDGEMENTS

I would like to thank my advisor, Dr. Ramin Pashaie, for the opportunity to pursue this research. His guidance, support and insight was instrumental towards accomplishing the goals of this project and his mentorship has made me a better researcher. I would also like to thank Dr. Rani El-Hajjar, who while working in his lab, inspired me to continue pursuing graduate studies. I would also like to thank my committee members, Dr. Jun Zhang and Dr. David Heathcote for their time and input into this thesis. I am also grateful for the support from the Electrical Engineering Department during my studies.

This project would not have been possible without our collaborators at NITRO Laboratory at the University of Wisconsin-Madison who provided the transgenic mice for our experiments. Tom Richner and Sarah Brodnick were instrumental in conducting the experiments, and provided valuable insight and discussion.

I am fortunate to have worked with a talented group of individuals on the project: Seth Frye, Farid Atry and Dr. Amy Kaczmarowski. Our discussions were always insightful and helped me gain a better understanding and approach for the task at hand. This team, and the supporting BIST Lab members, Mehdi Azimipour, Ryan Baumgartner and Rex Chen, have made working in the lab a pleasure.

I would not be here if not for the continuous support from my family and friends. I would like to thank my parents for their love and support, and my sister,

Dhany, for her continued encouragement. I am grateful for my friends in Milwaukee who have become like family to me. I would like to thank Marissa Jablonski, whose friendship, encouragement, and laughter has made my time here a joy. Finally, I would like to thank Aaron Mueller for his patience, support and understanding during this undertaking.

Thank you all.

Chapter 1

Introduction and Background

Chapter 1: Introduction and Background

1.1 Motivation

The brain is a complex network of interconnected neurons with each cell functioning as a nonlinear processing unit. Neural responses to stimulus can be described by activity in neurons. Neurons are the cells which function to control activity within the cerebral cortex. The cortex is comprised of six layers categorized by connectivity patterns and cellular composition [1]. Throughout the cortex, neurons are surrounded by capillaries, supplying the neurons with blood. The neural hemodynamic response, namely, the increase or decrease of blood flowing to the brain tissue, will determine the activation or suppression of neuron activity [2]. While blood flow changes have been associated with neural activity and are critical to normal brain function, this neurovascular coupling is not well understood.

To understand the effects of continuous and interrupted blood flow on the pathology of neurologic diseases such as Alzheimer's disease, Parkinson's disease and mental illnesses such as drug addiction and depression, quantification of the associated changes is essential. Hemodynamic response monitoring benefits from the ability to control neural stimulus in addition to locating and characterizing the blood flow signal quantitatively. A number of neural imaging and hemodynamic response monitoring techniques are in existence for clinical neuroscience studies, with varying degrees of spatial and temporal resolution. Current methods of neural imaging include magnetic resonance imaging (MRI), position emission tomography (PET), and two-photon microscopy, with a trade-off between imaging range and

resolution. Neural activity probing has been shown externally with electrocorticography (ECoG), electroencephalography (EEG) and functional near-infrared spectroscopy (fNIRS), fluorescence microscopy, functional MRI (fMRI) and PET. As with imaging, resolution and range of these techniques are dependent on the geometry and invasiveness of the method [3].

The aim of this project is to develop a device to perform neural imaging and hemodynamic response monitoring in regions of an animal brain *in-vivo* and provide the ability to control neuron stimulation simultaneously. Optogenetics is a recently developed neuromodulation technique that can stimulate and suppress activity in the brain with high spatial and temporal resolution with light.

The project will primarily focus on imaging cortical vasculature post-optogenetic stimulation in rodents. The vessel and capillary sizes in a rodent vary from tens to hundreds of micrometers [4]. Thus, a high resolution imaging system is needed to resolve features such as capillary beds.

Spectral-domain optical coherence tomography (SD-OCT) is a noninvasive optical imaging method that has been demonstrated to image rodent cortical microvasculature on the order of micrometers. Additionally, Doppler optical coherence tomography (D-OCT) has been shown to estimate blood flow velocity *in-vivo*. In this project, a device is developed to image blood vessels and monitor corresponding blood flow changes to study the effect of optogenetic stimulation in hemodynamic signals. This will be implemented by coupling a high-speed and high-resolution SD-OCT system with an optical path for optogenetic stimulation.

1.2 Biological Overview of Neurons

To understand the mechanism of optogenetics, this section briefly covers the biological background of neural anatomy and signaling. Neural activity is characterized by changes in electric potential across neurons to induce membrane action potentials. Neurons are one of two main classes of cells in the nervous system. The neuron structure consists of the cell body, dendrites, the axon hillock, myelin sheath, axon and axon terminals. The cell body holds components to maintain the cell's metabolic processes.

Dendrites are the branch-like structures extending out of the cell body responsible for receiving synapses, or inputs, from other cells. Axons extend away from the cell body in a similar manner to dendrites.

When a dendrite receives a chemical or physical signal, it begins a chain of events that facilitates neuron communication. The input signal induces a change, resulting in electrical current flow in and around the neuron. Action potentials are generated in the region of neurons called the spike triggering zone [5].

1.3 Optogenetics

Optogenetics is a new modality to manipulate neural activity with light using the tools of molecular genetics and photonics. The hallmarks of utilizing optogenetics are precise spatial neuronal control with high temporal resolution, on the millisecond time-scale, cell-type specificity and rapid reversibility [6].

In order to make neurons sensitive to light, specific genes are delivered to targeted cells to express light-sensitive ion channels or ion pumps. Once corresponding proteins are expressed in cells, the activity of the cell can be controlled by exposing the cell to appropriate wavelengths. The proteins that are used for optogenetic stimulation are adapted from algae, e.g. *chlamydomonas reinhardtii* Channelrhodopsin-2 (ChR2), or bacteria, e.g. N*atronomonas pharaonis* halorhodopsin (NpHR). When stimulated with blue light (470 nm), ChR2 acts as a light-gated cation channel. Here, the channel permits entry of sodium (Na^+) ions into the intracellular space of the cell, while potassium (K^+) ions exit through the channel to the extracellular space. Conversely, NpHR acts as a chloride pump, responding to yellow light (580 nm). When stimulated with yellow light, transport of chloride ions (Cl^-) is facilitated by overcoming the membrane potential of the cell. Stimulation of NpHR hyperpolarizes the cell and suppresses neural activity. The ion exchange mechanism is illustrated in Figure 1.

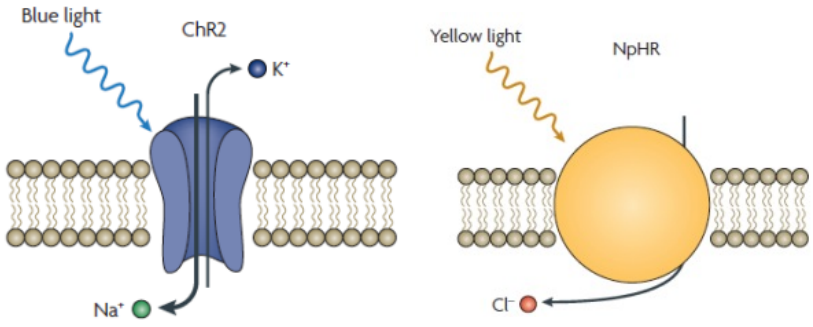

Figure 1 - (Left) Na^- ions entering the membrane through the ion channel, while K^+ ions exit when the cell is stimulated with blue light (470 nm). (Right) Chloride ions being transported through an ion pump when the cell is stimulated with yellow light (580 nm). Figure adapted from [7].

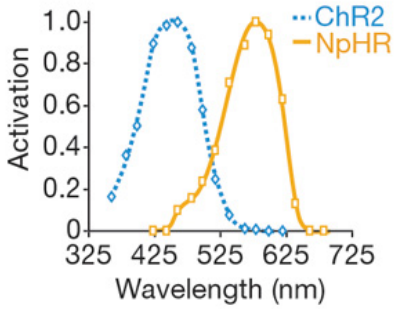

Figure 2 - Activation spectra for ChR2 and NpHR, separated by 100 nm. Figure adapted from [8].

Cell-type specificity permits the targeting of cell-types and avoids stimulation of surrounding cells, a process attributed to the microbial opsin gene delivery method [7]. This targeted method provides researchers with a tool to systematically interrogate neural circuits, and functions of cell-types.

Bi-directional control of cells is possible due to the differences in activation wavelengths of light-gated proteins. Thus, it is possible to stimulate and inhibit activity in the cell by a controlled pulsing pattern of light. A neuron spiking pattern of excitation and inhibition is shown in Figure 3 for cell-attached and whole-cell recording, demonstrating bi-directional control with single spike precision [8]. Blue light stimulation pulses at 15 ms intervals are shown, corresponding to spiking with each period and pulse. A continuous yellow light is then simultaneously illuminated with blue light pulses. When the blue light is pulsed, the continuous yellow light suppresses the rising spike, effectively suppressing stimulation. Thus, when stimulated with blue light pulses, the spike amplitude is suppressed before reaching

its peak. This switching demonstrates the bi-directionality advantage of an optogenetic stimulation mechanism.

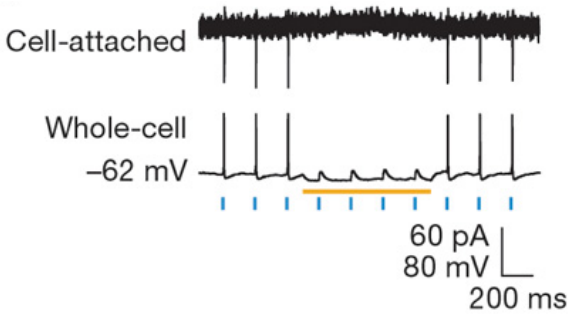

Figure 3 - Excitation and inhibition of spike trains based on blue and yellow light pulses. Figure adapted from [8].

The advent of optogenetics offers a precise method of controlling stimulus in the brain. The use of genetic tools in this method allows cell-specific targeting and avoids involuntary stimulation in neighboring cells, unlike electrical stimulation methods [7]. Electrode implantation for electrical stimulation is limited in its precision and may stimulate nearby cells. In contrast, optical stimulation provides a systematic approach to determine neural interconnections and effectively removes ambiguity of unrelated activity that may be caused by electrical stimulation.

1.3.1 Light Delivery Methods

Light delivery methods vary depending on the requirements of the application [3]. Some common delivery methods include using waveguide systems or direct illumination of light onto the surface of the cortex using spatial light modulation.

Optical fibers provide an efficient method for light delivery, permitting precise targeting of the cortical region for stimulation. For implantation on to a mouse brain, light is sent through an optical fiber with a diameter of 100 – 200 μm to the cortex surface. A cannula situated atop the house head holds the fiber in place to deliver light to an area close to the fiber tip. When the waveguide is situated above the motor sensory region of the brain, a freely moving mouse was directed to only move in a counterclockwise direction when the region of light-sensitive cells was stimulated with blue light. The drawback to a waveguide system is the limited field of stimulation due to the light absorption and scattering inside tissue. Without waveguides, high intensity LEDs can be used to directly illuminate the cortical region without using an optical fiber.

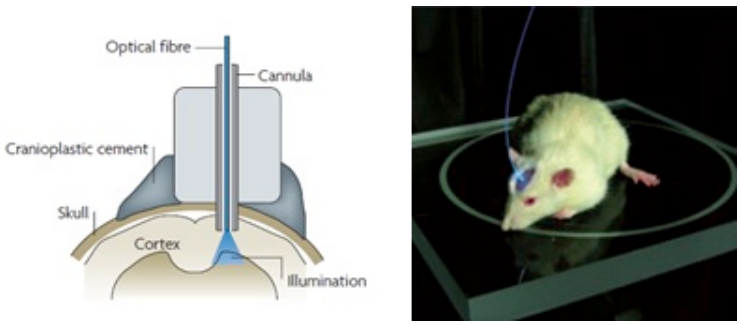

Figure 4 – (Left) Drawing of an optical fiber implantation on the cortical surface of a mouse, and (Right) the actual implementation. Figure adapted from [7].

Spatial modulators provide a larger field of view for stimulation, classifiable as MEMS based or liquid crystal based designs. An example of a MEMS-based system is a digital micromirror device, which uses a computer controlled array of mirrors to

project filtered light onto the surface of the brain. Such designs provide room for imaging using bright-field or fluorescent imaging in addition to stimulation.

1.4 Fluorescence Microscopy

Fluorophores are routinely used as biomarkers, and the increasing prevalence of their use as biomarkers has furthered the advancement of fluorescent protein technology in fluorescent microscopy [9]. Prior to fluorescence imaging, external dyes were used to discriminate between cells. However, the working time of these dyes posed some limitations, in addition to the toxic hazard presented. Protein-based fluorophores were introduced through cloning of a jellyfish, and are used as biomarkers as an alternative to external dyes [10].

The basis of fluorescence is photon emission due to absorption of photons with a high energy state, or shorter wavelength. A fluorophore is a molecule that produces fluorescence. When molecules in the resting state are excited by a source, some absorb the energy before moving to an unstable excited energy state. Release of a photon during a transitional period (from 10^{-15} to 10^{-9} s) causes the molecule to return to a lower energy state, becoming stable again. The emitted photon, which is in a lower energy (longer wavelength) than the excited state, can be captured on a photodetector. The Jablonski diagram in Figure 5 shows the excitation and emission process in a molecule.

Fluorescent markers are well-suited for serving as biomarkers in optogenetics, because they can be genetically encoded into the protein. Fluorescent

proteins (FP) can be engineered for sensitivity to membrane potentials, ions and neurotransmitters. One of the uses of fluorophores in neural imaging is for visualization of synaptic transmission and activity-based signaling. In optogenetics, fluorescent proteins are used as a reporter when illuminated with blue light.

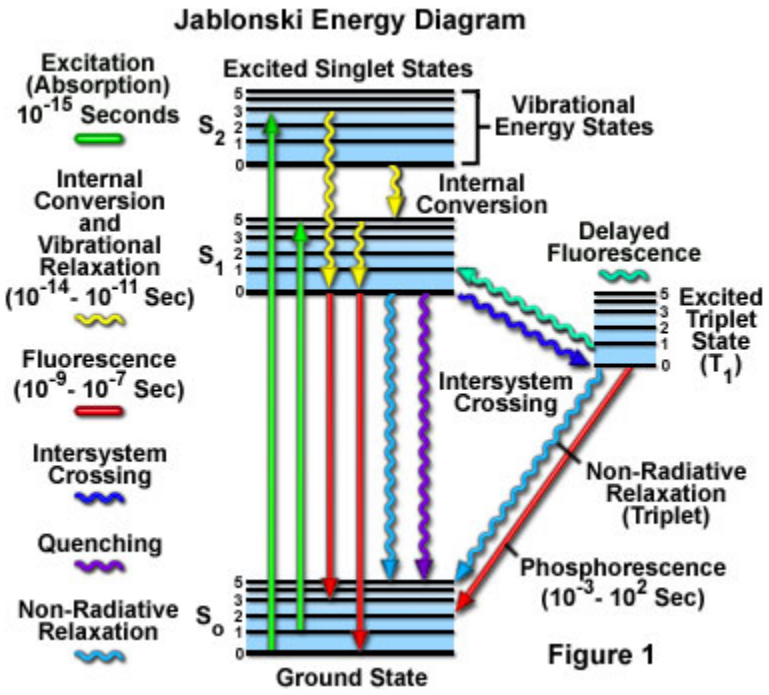

Figure 5 - Jablonski diagram of a photon excited to a higher state, and its transitional period to ground state, resulting in the emission of light. Figure adapted from [11].

In our optical coherence tomography system, a fluorescence microscope is also integrated to detect fluorescence markers such as yellow fluorescent protein (YFP). The optogenetically targeted cells in our studies were marked with YFP. When exposing the YFP to blue light (470 nm), a bright green (530 nm) fluorescent emission is captured with the fluorescent microscopy branch of the device in parallel.

1.5 Optical Coherence Tomography

Optical coherence tomography (OCT) is a non-invasive light based imaging modality with the ability to yield high-resolution three-dimensional images. The basis of OCT imaging stems from low-coherence reflectometry techniques, which were previously demonstrated for ranging measurements. This imaging modality enables cross sectional imaging of biological tissue based on its optical reflectivity. The principle behind OCT is analogous to ultrasound imaging, although instead of acoustic waves, backscattered light is measured.

Interferometry facilitates the measurement of the magnitude and echo time delay of backscattered light from a sample, in this case, biological tissue. A Michelson-type interferometer is used, as shown in Figure 6.

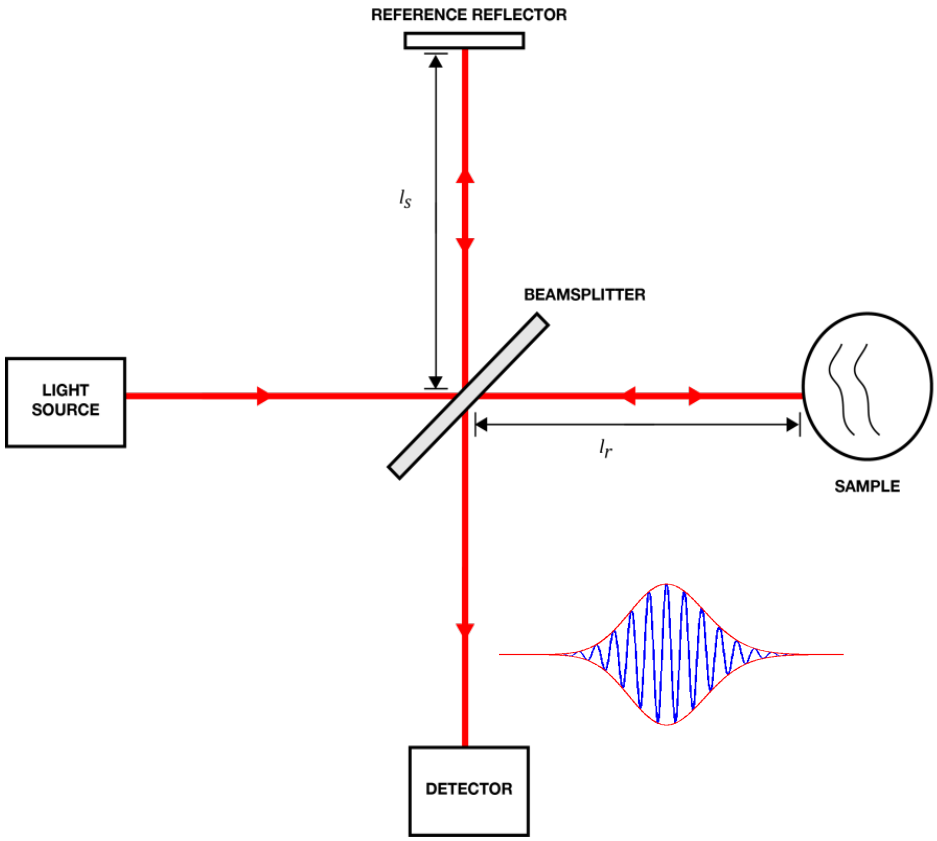

Figure 6 - Schematic of a Michelson interferometer.

Interferometry aims to determine the interference pattern produced by light reflecting back from a sample and reference arm. Incident light is illuminated from a low-coherence source with a broad bandwidth and transmitted into an equally splitting beam splitter. Part of the beam travels the length of a known distance to a reflective surface, such as mirror, and sent back to the beam splitter. The remaining beam travels through the sample arm, and illuminates a sample, which can be modeled as a discrete set of reflectors. The backscattered signal from the sample is sent to the beam splitter. Light from sample and reference arm is recombined, creating an interference pattern. This interference pattern is the correlation of light

from both sample and reference arms. Interference occurs when the reference and sample arms are within the coherence length of the source. Coherence length is the autocorrelation of the full width at half maximum (FWHM) of the source spectrum. The highest interference occurs when both sample and reference arms have the same path, resulting in total constructive interference, with light in phase at all points.

OCT data can be represented in three forms. A-scans or A-lines are one-dimensional (1D) axial, or depth scans of a position. The reflectivity profile is the spatial interference pattern of one point in the sample. Peaks in the reflectivity profile denote a change in the refractive index, and the higher peaks are commonly attributed to the surface of a sample. Adjacent A-scans form two-dimensional (2D) cross-sectional images, also known as B-scans. A cross-sectional image is obtained from scanning along a lateral direction. C-scans span both lateral and axial directions, forming a three-dimensional (3D) data set from sequential B-scan frames. The set of C-scans can be rendered to visualize a volumetric image. A sample of the various scan protocols are shown in Figure 7**.**

Distinction of OCT modalities is determined by the interferometry detection technique used. The earliest OCT modality is the time-domain OCT (TD-OCT). In time-domain systems, a mirror is translated in the reference arm during data acquisition to create the zero-path length difference in the interference pattern. The returned beam is captured using a single photodetector. TD-OCT systems are limited in its acquisition speed due to the moving mirror of the reference arm, and susceptible to motion due to the moving mechanical parts. Growth in OCT research

benefited from technology advancements such as high rate CCD cameras and advanced diffraction gratings, leading to the development of Fourier-domain OCT (FD-OCT). FD-OCT provides video rate imaging, suitable for imaging biological tissue. Doppler OCT (DOCT) is the application of the Doppler principle in OCT imaging to achieve high resolution images of moving scatterers in tissue.

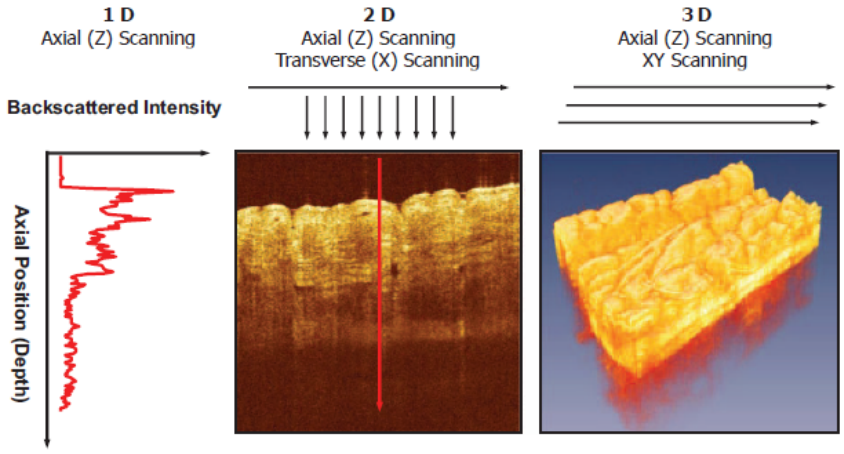

Figure 7 - (Left) A-scan, or depth profile, (Middle) B-scan or cross-sectional image and (Right) C-scan or a volumetric image acquired from an OCT scan. Figure adapted from [12].

In its formative stages, OCT research flourished in ophthalmologic applications, where its introduction in 1991 saw OCT imaging of the retina at the inner surface of the eyeball. OCT is an effective imaging system for transparent tissue, making the eye particularly well-suited for OCT imaging. Some of the earliest *in*-vivo images obtained from OCT included retinal images from clinical studies in mid 1990s. The studies were aimed at diagnosis and monitoring of a series of macular diseases including macular edema, and age-related macular degeneration. Dense tissues, such as the lungs and kidneys, limits the OCT imaging range due to

beam attenuation as it propagates through the tissue. Imaging of nontransparent tissue using OCT rose in prevalence with the introduction of longer wavelengths to increase imaging range, through the reduction of scattering.

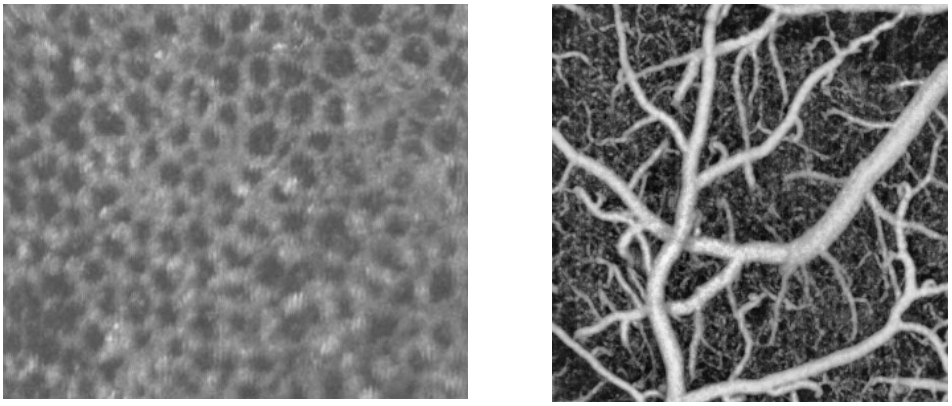

Figure 8 - (Left) Alevoli structure in a rat lung. (Right) Angiogram of a cortical patch of a mouse brain. Both images are produced with the OCT system developed for the project.

The first commercial system introduced provided 400 axial scans per second with an axial resolution of 10 μm. Since its introduction, OCT technology has made considerable strides in the biomedical field, and has expanded its reach since in its early uses [13] [12] [4] [14]. The increasing demand for broadband sources with higher power stemmed from the realization of OCT imaging of dense tissue is possible with longer wavelengths.

The high spatial and temporal resolution of the imaging method allows sub-micrometer resolution detection, useful for highly scattering media, such as biological tissue and a penetration depth in the millimeter range. OCT fares well in comparison to other non-invasive imaging techniques currently in use, such as ultrasound and MRI. MRI achieves resolution on the order of 1 mm, thus finer details of a structure will not be resolved well. However, MRI is useful for imaging

structures on a relatively large scale with its penetration depth on the order of 10 cm. Its operation and maintenance requires specialized training, and bulky packaging makes it impractical to transport. Clinical ultrasound has the ability to penetrate deeper tissue, with depths up to 10 cm reported, but suffers from low resolution on the order of millimeters as a tradeoff. High frequency ultrasound in the ranges of 100 MHz can achieve up to 15-20 micrometers in resolution but imaging is limited to the millimeter range. On the other part of the spectrum, confocal microscopy has the ability to provide high resolution on the order of 1 micrometer. However, the penetration depth is limited to a range of a few hundred micrometers. X-ray imaging and MRI approaches expose the subject to radiation. While the levels of radioactive exposure in these imaging modalities are closely monitored, OCT avoids unnecessary radiation exposure.

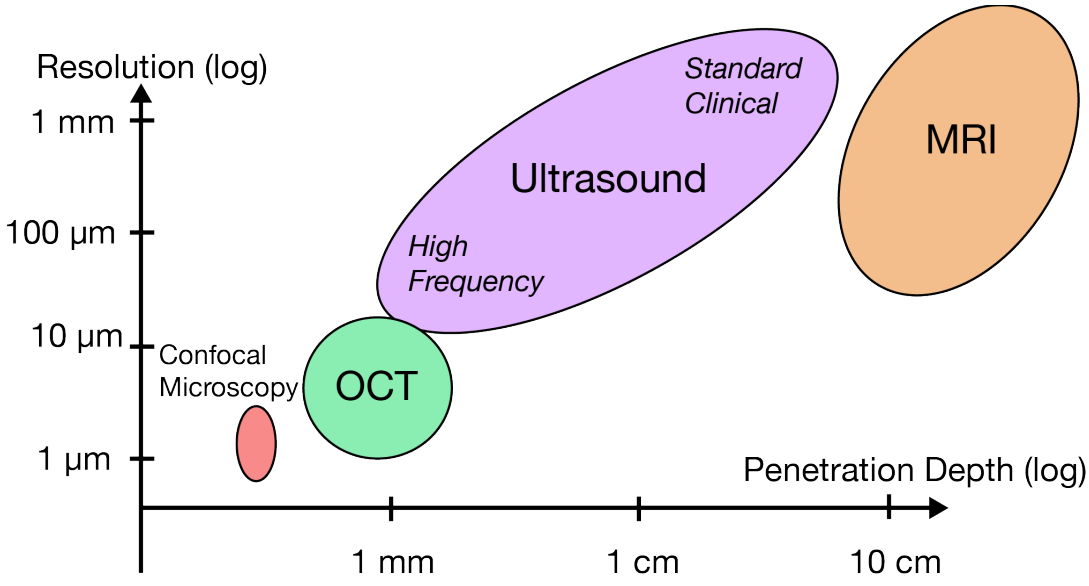

Figure 9 - Comparison of imaging systems resolution and penetration depth range, scaled logarithmically. OCT fills the gap in imaging with micrometer resolution.

1.5.1 Time-Domain Optical Coherence Tomography

TD-OCT obeys the Michelson interferometry, where incident light beam is split through a beam splitter to a reference and sample arm to measure the electric field. The sample is scanned to obtain a cross-sectional image using scanning mirrors to move across each transversal point. At each point, the reference mirror is translated along a path to determine an interference pattern between the sample and reference arms. The mirror moves across a length within the field of view of the OCT system, creating a Doppler shift in the reference field.

The light produced from the source is split by a 50:50 fiber coupler. Then the two beams are recombined, where the interference of the sample and reference arms are measured using a balanced photodetector. The signal is then demodulated. The measured photoelectric current is used to quantify the optical power, and the result is an axial reflectivity profile of a transversal position [15]. The process of time-domain detection is shown in Figure 10.

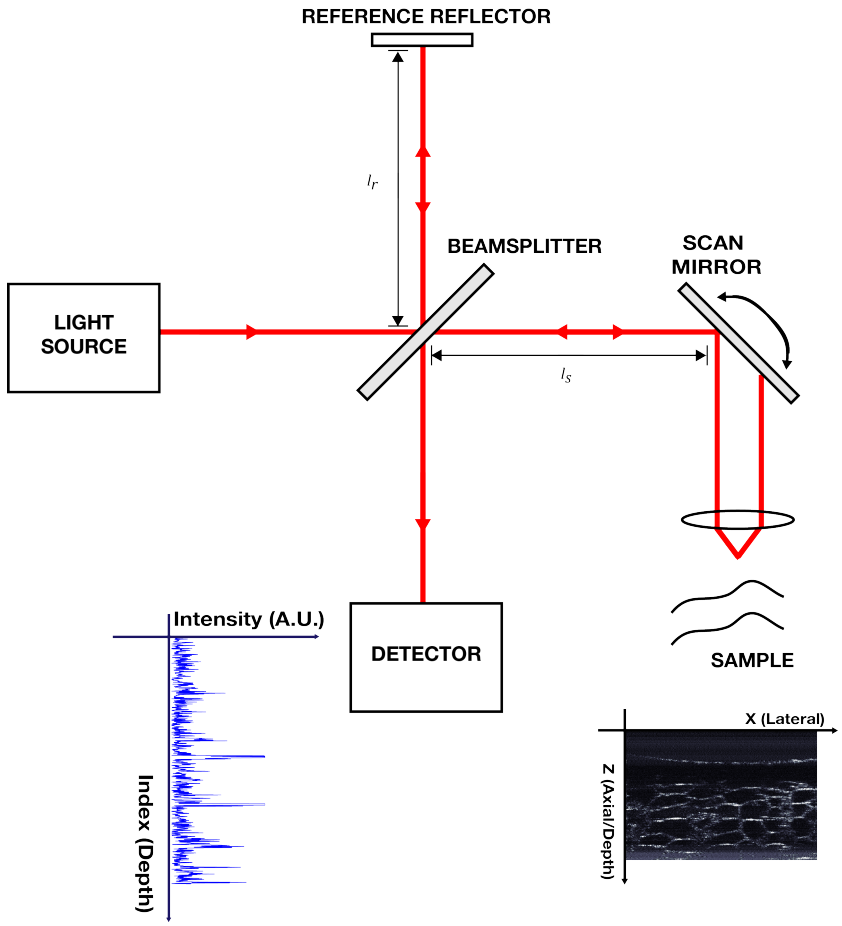

Figure 10 - Schematic of a time-domain OCT system.

1.5.2 Fourier-Domain Optical Coherence Tomography

Fourier domain OCT has attracted the attention of researchers as an alternative to TD-OCT. First introduced in 1995, FD-OCT operates based on low-coherence interferometry similar to its time-domain counterpart, with a different detection technique. Also known as frequency-domain OCT, interference occurs in the frequency domain, and allows simultaneous capture of the interference spectrum, significantly increasing imaging speed. FD-OCT offers a faster acquisition time and a higher signal-to-noise (SNR) ratio in comparison to its TD-OCT, and is well suited for low light recording. The reference arm does not require a moving

mirror, enabling an increase in acquisition speed. The sensitivity enhancement is the ratio of axial resolution to axial imaging depth and frequency-domain detection has an increase of 50-100 times [12]. FD-OCT systems rely on signal post-processing to reconstruct the interference spectrum into an axial profile, using a Fourier transform. While the computation requirements are higher, the benefit of faster imaging is essential in the study of biological systems. Based on the detection method used, two branches of FD-OCT exist: the spectrometer-based SD-OCT and swept-source OCT (SS-OCT).

SD-OCT detection uses a spectrometer and a high-speed line CCD camera to record the interference spectrum. Figure 11 shows the schematic of a typical SD-OCT system. Incident light from a broadband source is split into the reference and sample arms. The beams are modulated as a function of frequency. A dispersive element, such as a diffraction grating, disperses the recombined fields and the interference spectrum is captured on a line CCD camera as a function of wavelength. The axial profile is attained by converting the independent variable, from wavelength to frequency domain, through a Fourier transformation of the interference spectrum. The resulting axial profile is a logarithmically compressed magnitude of the complex signal. The CCD camera counts photoelectrons to measure the optical energy, which depends on exposure time. Sample motion may result in the averaging of interference fringes for slow acquisition speeds, thus high speeds are typically used in this imaging. High-speed imaging is advantageous for high-quality imaging, by increasing the number of scans over time.

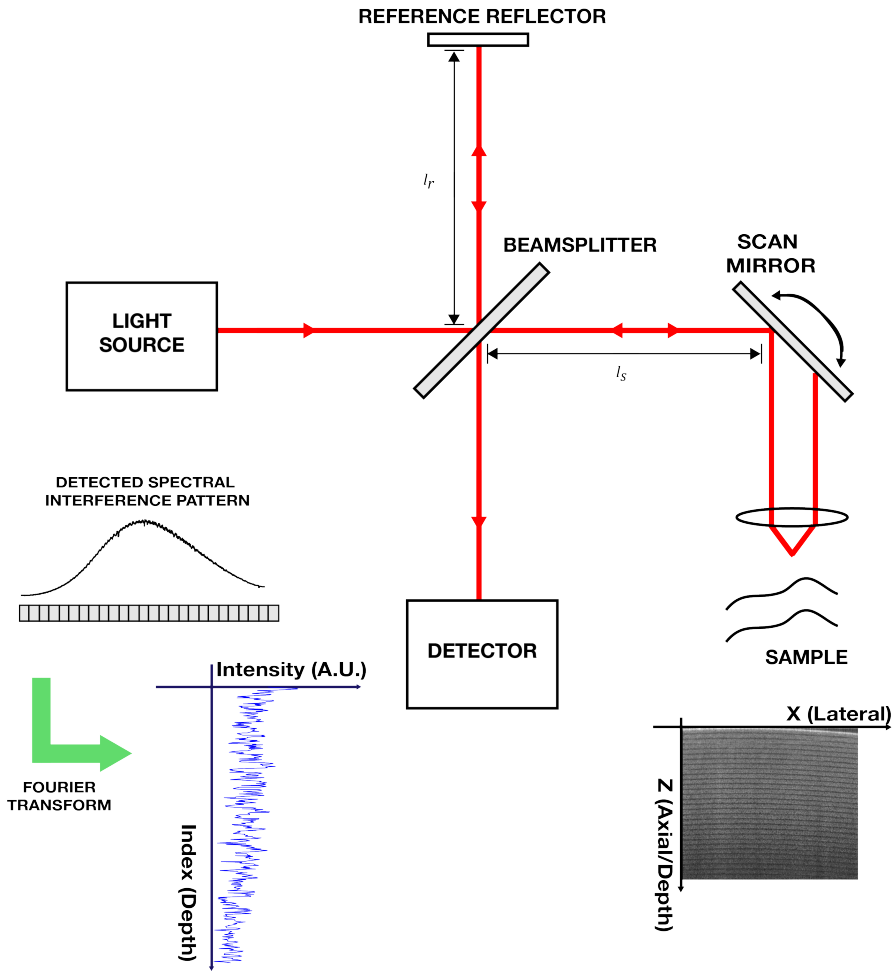

Figure 11 - Schematic of a spectral-domain OCT system.

SS-OCT detection uses a photodetector to capture the intensity spectrum while the source is tuned. In SS-OCT, a narrow-band frequency-swept laser source is used to perform interferometry. The beam is split into a reference and sample arm, similar to SD-OCT, where the mirror at the reference arm is fixed. The interference spectrum is captured as individual spectral components sequentially using a single detector. Due to source tuning, the reference arm causes a frequency offset. Interference of the sample and reference arms result in a beat seen in the interference pattern, with a frequency determined by the offset frequency. Finally,

the axial profile is obtained by taking the Fourier transform, similar to the process in SD-OCT systems [13] [12] [14].

1.5.3 Doppler Optical Coherence Tomography

OCT imaging relies on optical properties of tissue, namely scattering and refractive index, to create contrast in the cross-sectional images. However, disease pathology cannot easily be characterized on contrast alone. Vasculature-based disease pathology is well-documented, spanning from ocular to dermal diseases. The ability to track physiological changes noninvasively is valuable for biomedical research and diagnostics. Doppler OCT (D-OCT) provides a functional extension of OCT that has the ability to detect changes in blood vessels.

D-OCT combines the Doppler Effect with OCT imaging to quantitatively measure changes in fluid flow. The Doppler Effect describes the observed changes in the frequency of a wave from a moving object. By using the observed frequency shift, the velocity of moving particles, such as red blood cells, can be determined through OCT imaging. Moving particles interfering with a reference beam induces a Doppler frequency shift in the interference pattern, based on the incident light beam and the outgoing scattered light [1] [12] [14].

Several velocity estimation methods based on D-OCT have been developed. The time-domain implementation follows a spectrogram method where a short time Fast Fourier transform (STFFT) or wavelet transform is used to determine the interference spectrum. However, this method is limited in its resolution, based on

the window size of the STFFT and is compatible with high-speed imaging only. Alternately, phase-resolved Doppler OCT (PR-DOCT) was proposed to provide an improvement in velocity sensitivity. However, one of the limiting factors in D-OCT imaging is its sensitivity to flow direction. The Doppler shift is detectable only for vessels parallel to the scanning beam. Any perpendicular flow to the beam is not registered. This parameter makes flow determination challenging since the direction of blood flow is generally not known in live tissue.

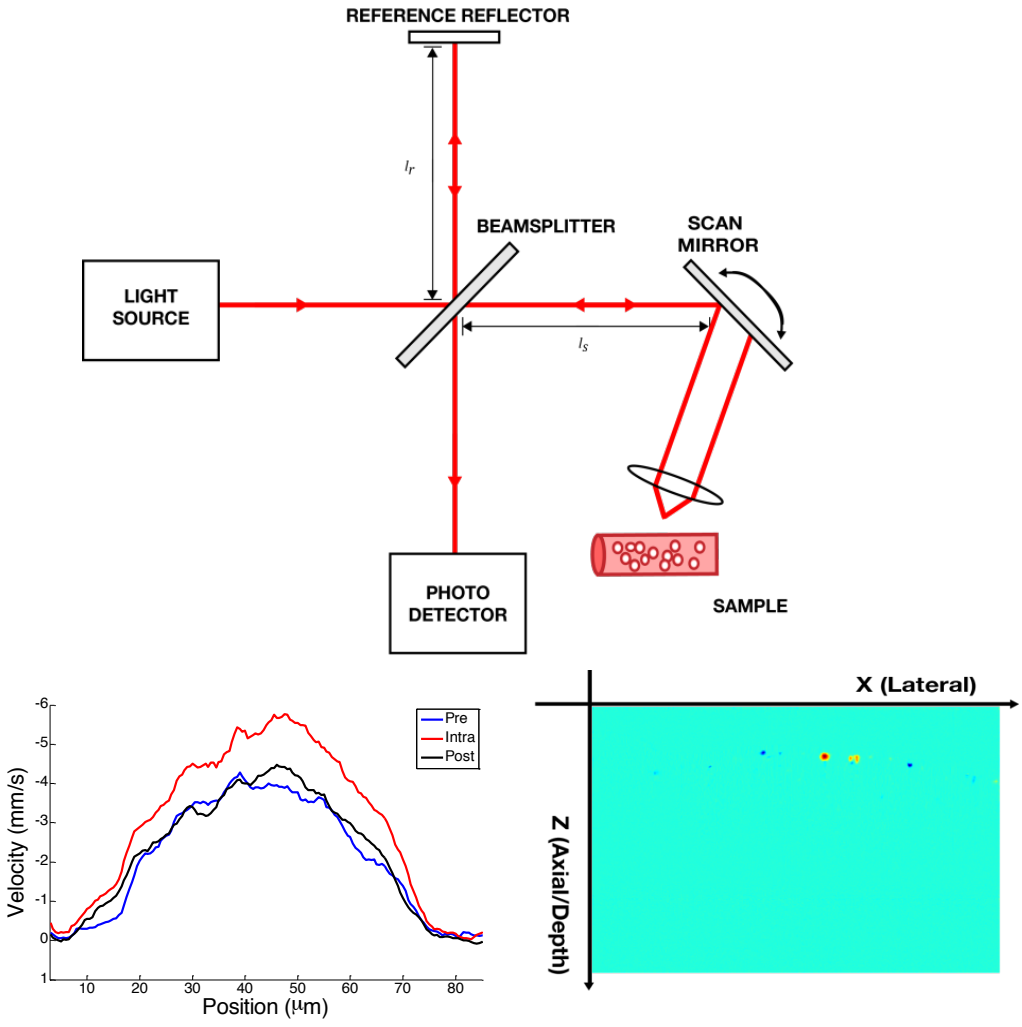

Figure 12 - Schematic of a Doppler OCT system

Chapter 2

Principles of Optical Coherence Tomography

Chapter 2: Principles of Optical Coherence Tomography

Optical coherence tomography (OCT) is a noninvasive imaging technique, with sub-micrometer resolution, making OCT suitable for *in-vivo* visualization of the vasculature network in the cerebral cortex. The main principle underlying OCT is low-coherence interferometry, and here the theoretical basis, particularly for spectral-domain OCT and Doppler OCT is explored. The theoretical basis looks at relationships that affect system design are considered, including beam spot size, depth of focus, resolution and spectral response. Trade-offs between resolution and depth of penetration is also considered towards an optimized system design.

2.1 Theory of OCT

The underlying principle of operation for OCT is low-coherence interferometry. Interferometry facilitates the measurement of the magnitude and echo time delay of backscattered light from a sample, in this case, biological tissue. Biological tissue can be considered to be multiple discrete reflectors of varying reflectance. Michelson interferometry is used to perform the measurements, where a typical set-up seen in OCT is shown in Figure 6. Interferometry requires a source, a reference arm, sample arm and a beam splitter. Incident light is illuminated from a low-coherence source with a broad bandwidth. Partial beams are sent to the reference and sample arms through an equally splitting beam splitter. The electric field representing an OCT signal can be expressed mathematically as a complex phasor, as a function of the wavenumber and angular frequency, in the form:

$$E = E_0 e^{i(kl-\omega t)}$$

where E_0 is the amplitude, $k = \frac{2\pi}{\lambda}$ is the propagation constant, l is the distance of light traveled, $\omega = 2\pi f$ is angular frequency and t representing time. The reference and sample arm beams, E_R and E_S respectively, are represented by the complex phasors:

$$E_R = E_{R,0} e^{i(kl_R - \omega t)}$$

$$E_S = E_{S,0} e^{i(kl_S - \omega t)}$$

The reference beam E_R, is sent to a mirror located at the terminal point of the reference arm. The sample beam E_S is sent to the arm consisting of the object under test, such as biological tissue. The recombined field, E_{OUT}, which is captured by a detector is a superposition of the sample and reference arms. E_{OUT} can be expressed as:

$$E_{OUT} = E_R + E_S$$

The interference pattern is the correlation of sample and reference arm electric fields, which are time-averaged on a photodetector. This detected intensity can be written as:

$$I(t) = \langle |E_R + E_S|^2 \rangle = \langle E_S E_S^* \rangle + \langle E_R E_R^* \rangle + 2Re\{\langle E_S E_R^* \rangle\}$$

The interference is a combination of self-interference and cross-interference terms. Self-interference, also referred to as the autocorrelation of the signal, is the observed interference between reflectors in the sample. These terms are independent components and are represented as $\langle E_S E_S^* \rangle$ and $\langle E_R E_R^* \rangle$ for the sample and reference arms respectively. The first term, square of the magnitude of the

sample arm $\langle E_S E_S^* \rangle = E_{S,0}^2$ is negligible. Typically, the sample arm reflectance is small in comparison to the sample arm reflectance. The second term, which is the autocorrelation of the reference arm, is the magnitude of the reference arm squared $\langle E_R E_R^* \rangle = E_{R,0}^2$. This term can be adjusted by subtracting a reference arm reflection from the acquired signal. The cross-correlation terms are components that describe the interference between the reference and sample arms. This term contains the information on the reflectivity profile along the depth of the sample. The cross-correlation is represented by the term $2Re\{\langle E_S E_R^* \rangle\}$, and can be described as the time-average of the sample and conjugate of the reference reflections. The real term can be written as:

$$2Re\{\langle E_S E_R^* \rangle\} = 2\cos(\Delta\phi)$$

where

$$\Delta\phi = k_S l_R - k_R l_R = 2\pi \frac{n(\Delta l)}{\lambda_0}$$

$$\Delta l = l_S - l_R$$

In this signal, phase modulation and the envelope of the autocorrelation function is represented by rapid oscillations and a Gaussian envelope, respectively. Variations on the interference create fringes that are resultant of changing phase difference, $\Delta\phi$, dependent on the length mismatch Δl. The length mismatch represents the difference between the reference and sample arm.

Interference is dependent on the coherence length of the light source. Source coherency and the path length difference for the reference and sample arm dictates the minimum detectable interference signal. Low-coherence, or broad bandwidth sources, detect interference when the sample and reference arm path lengths are within the coherence length of light. For coherent sources with a narrow linewidth, interference occurs across a larger path length difference (on the order of centimeters or meters) between the reference and sample arm. Low-coherent, or broad bandwidth sources, detects interference when the sample and reference arm path lengths are within the coherence length of the light.

Coherence length is the product of the velocity of light in vacuum, and the coherence time is a measure of the degree of coherency over time. In other words, this can be found as $l_c = ct_c = \frac{c}{\pi\Delta\lambda}$ where c is the speed of light in vacuum, and $\Delta\lambda$ is the bandwidth of the source, or the full width at half-maximum (FWHM) of the source spectrum.

In its practical implementation, Michelson interferometry can be performed in both free space and waveguides, such as the optical fiber. Optical fibers are favorable due to its portability, economic value and availability due to the development in telecommunication technologies. Many telecommunication components are available for source wavelengths used in OCT. Furthermore, the fiber optic coupler is not always split equally at a 50:50 ratio. Our OCT system takes advantage of variable fiber optic coupler in order to direct more power to the weakly reflecting sample arm in order to achieve a higher signal to noise ratio.

2.2. Spectral Domain Low Coherence Interferometry

In spectral-domain OCT (SD-OCT) using a low-coherence source, the intensity is captured through a spectrometer. The recombined beams from the sample and reference arms are recaptured as the spectral interferogram, $I(\lambda)$ as a function of wavelength, λ. The detected signal is a superposition of DC terms, cross-correlation and auto-correlation terms.

A common detector choice in SD-OCT configurations is a line CCD camera. Prior to illuminating detector surfaces, the recombined reference and sample arm beams are dispersed into wavelength components where a prism or a diffraction grating may be employed. Sample reflection information is carried in the cross-correlation terms.

The sample reflectivity profile is attained through taking the inverse Fourier transform of the spectral interferogram. Due to Hermitian symmetry from the Fourier transform of a real spectral interferogram, the reflectivity profile is a mirror image of the positive and negative distance from the zero path length.

The autocorrelation and DC terms of the detected spectrum result in undesirable image artifacts. The DC terms cause a bias in the spectrum, by shifting its amplitude. To compensate for this effect, the reflectivity profile without any reflector in the sample arm can be subtracted with the sample reflectivity profile to mitigate the amplitude bias.

Autocorrelation terms may appear as “ghosting” and appear in the image to mimic the structure of the sample under test. An uneven distribution of power to the

sample and reference arms reduces the likelihood of more obstructive autocorrelation terms in the image.

2.3 Doppler OCT

Doppler OCT (DOCT) is the amalgamation of principles of the Doppler effect with OCT imaging to measure changes in fluid flow. The Doppler frequency shift detected is the interference of backscattered signals from moving particles in the sample with a reference beam [1] [12] [14]. The observed frequency shift is used to determine the velocity of the moving particles. The Doppler shift is characterized by the equation:

$$\boldsymbol{f_D = \frac{1}{2\pi}(k_s - k_i) \cdot v} \qquad \textbf{Equation 1}$$

where $\boldsymbol{k_s}$ and $\boldsymbol{k_i}$ represent wave vectors for incoming and outgoing (or scattered) light respectively, and $\boldsymbol{v}$ the velocity vector of a moving particle. In DOCT, interference is measured for an incoming light beam at a Doppler angle θ. Velocity can be related to the Doppler shift by the equation:

$$\boldsymbol{f_D = \frac{2Vcos\theta}{\lambda_0}} \qquad \textbf{Equation 2}$$

where V is the velocity and λ_0 is the source center wavelength. The schematic portraying the relationship between the incoming light beam and velocity is shown in Figure 13**.**

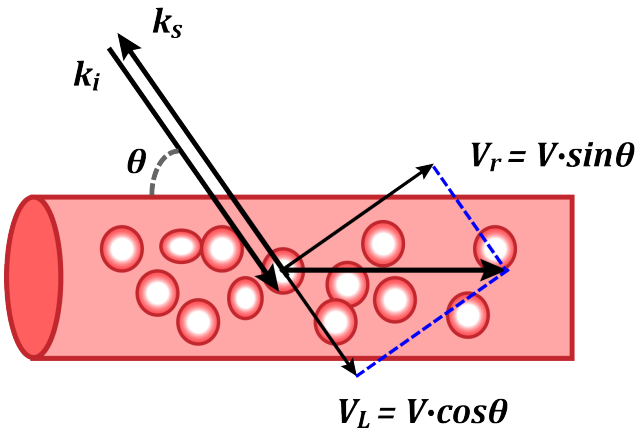

Figure 13 - Depiction of frequency shift caused by moving particles for Doppler OCT velocity measurement.

In practice, DOCT scanning is performed with a TD- or FD-OCT system with the incident source from the scan lens is set at an angle. Processing for Doppler OCT requires additional steps to determine the velocity, in addition to standard signal processing for imaging.

2.4 Imaging Resolution

Each depth profile is constructed from the A-scan recorded during data acquisition and scanning. Resolution continues to be an important consideration in imaging, and high resolution is especially valuable in resolving cellular boundaries often seen in biological tissue. In high-resolution imaging, both axial and lateral resolution is of significant importance. The advantage of OCT systems is that the axial and lateral resolutions are independent of each other. Axial resolution depends on the source, while lateral resolution depends on the sample arm objective. Thus, this resolution decoupling allows for easier system optimization.

Imaging nontransparent biological tissue ideally uses sources ranging from 1250 nm to 1350 nm. This wavelength will maximize the effective imaging range. However, axial resolution is limited by the source bandwidth of the OCT system. Maximum lateral resolution can be considered in enhancing the system design due to the independence of the axial and lateral scanning components. In the next two sections we discuss the relationship and factors determining the system resolution.

2.4.1 Axial Resolution

Axial resolution, known also as depth or longitudinal resolution, is defined by the source coherence length. It is particularly susceptible to depth-dependent distortion, as effects of scattering degrades the signal in deeper structures. The maximum axial resolution can be characterized as the coherent length of the laser source. Coherence length is defined as the FWHM of the autocorrelation of the source spectrum, for a Gaussian spectral distribution [12]. This yields the definition of axial resolution Δz as:

$$\boldsymbol{\Delta z = \frac{2 \ln 2 \lambda_0^2}{\pi \Delta \lambda}} \qquad \textbf{Equation 3}$$

with λ_0 defined as the source center wavelength and $\Delta\lambda$ as the source bandwidth. As indicated with the equation, the axial resolution is dependent on the source bandwidth. From the relationship in Equation 3, the axial resolution and source bandwidth of the system has an inversely proportional relationship.

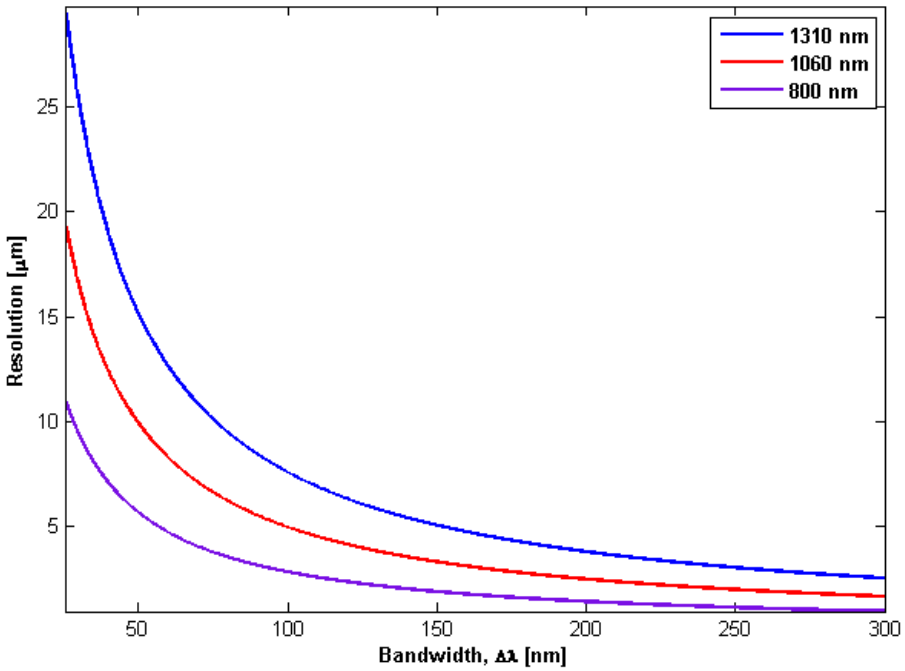

Figure 14 – Inversely proportional relationship between OCT axial resolution and source bandwidth of a system.

For a higher axial resolution, a wider source bandwidth is necessary. In its practical application, care must be exercised in selecting the source for the maximum axial resolution. Figure 14 demonstrates the inversely proportional relationship for varying source center wavelengths.

2.4.2 Lateral Resolution

Lateral resolution provides resolution in the transversal direction of scan and is characterized by the beam spot size. The lateral resolution Δx is dependent on the diffraction limited spot size, as in microscopy, and defined by the equation shown:

$$\Delta x = \frac{4\lambda f}{\pi d} = \frac{2\lambda}{\pi NA_{obj}} \qquad \text{Equation 4}$$

where f is the focal length of the objective lens and d is the beam diameter from the objective lens.

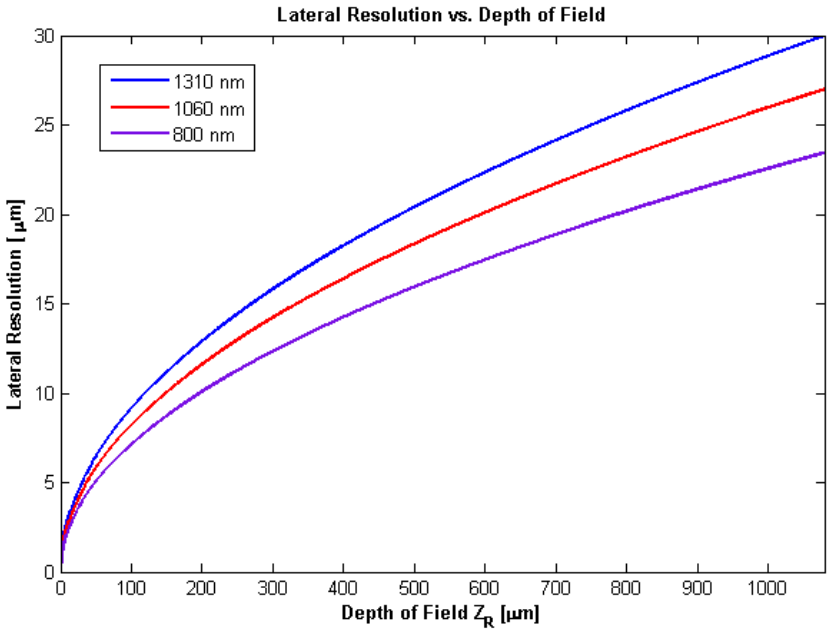

Figure 15 – Inversely proportional relationship between lateral resolution and depth of field

Optical design of the lateral resolution is governed by the inversely proportional relationship between the minimum spot size of the beam and the numerical aperture (NA) of the objective lens. The numerical aperture describes the beam focusing angle. Furthermore, lateral resolution of the OCT system is constrained in its depth of field due to a confocal parameter, which defines depth of field as twice the Rayleigh range of the beam by the equation [12]:

$$2z_R = \frac{\pi \Delta x^2}{\lambda} \qquad \text{Equation 5}$$

Figure 16 shows the relationship between the depth of focus and lateral resolution.

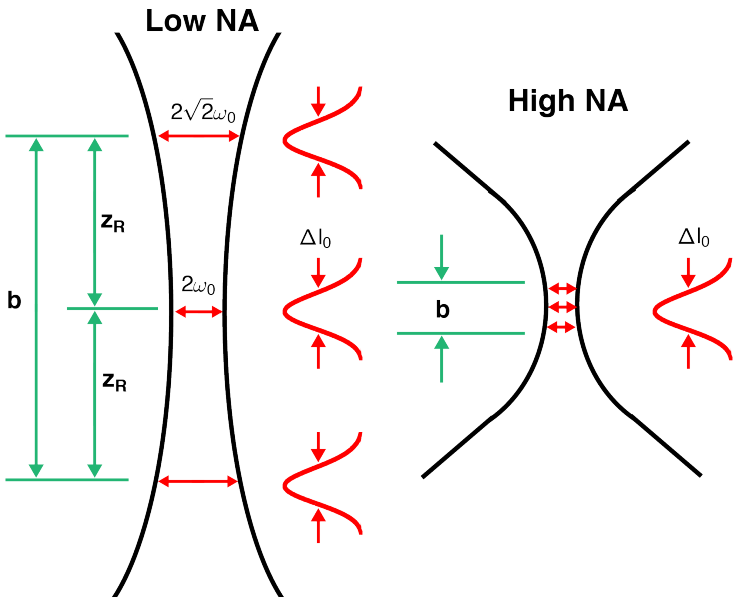

Figure 16 – The effects of numerical aperture in relation to the beam spot size and depth of field.

The effect results in a trade-off for the lateral resolution of the system. A high transversal resolution can be attained by selecting a lens with a higher NA value. This will provide a smaller beam spot size, at the cost of depth of field. Thus, a shorter range of the sample will be in focus and the remainder will be blurred. A lower NA lens provides a larger depth of field; however the spot size limits the finest transversal resolution. In other words, the spot size would be less focused in comparison with a higher NA lens.

2.5 Imaging Range

In an SD-OCT system, the spectral interference pattern is recorded on a spectrometer in the detection arm of the system. The pixel size on the spectrometer dictates the maximum depth that the SD-OCT system can capture. As we will see in

the software section, the spectral interference pattern in the frequency-domain is Fourier-transformed to attain the sample reflectivity profile in the spatial domain. Ideally, the detector would have an infinite number of detector infinitesimal pixels and will not limit the maximum imaging range. However, the spectrometer has a finite number of pixels with some physical dimensions to record the spectral response, limiting sampling and frequency resolution. Theoretically a Gaussian laser source will have tails to the infinity in the wavelength domain which cannot be captured by the spectrometer. This will reduce the practical resolution of the SD-OCT system from the theoretical maximum resolution (Equation 3). The spectral range recorded by the line CCD detector depends on the hardware design and will determine the practical axial resolution of the system.

On the other hand when the spectral range that the spectrometer captures is fixed in the hardware, the spectrometer pixel size will play the major role in the imaging range. Based on the spectral range that the spectrometer captures and its pixel size, each pixel is covering a spectral band which is basically the sampling rate of the spectrum. The smaller the pixel size the deeper the system can capture. This factor another trade-off in the design consideration, with an inversely proportional relationship between the spectral ranges recorded on the spectrometer and OCT imaging range, represented by pixel spacing in the axial direction. This trade-off should be considered in design, between a highly resolved shorter imaging range is desired or a less resolved longer imaging range, as is shown in Figure 17.

When the spectrometer detector captures a larger spectral range (shown in Figure 17(c)), the Fourier-transformed axial profile imaging range is limited.

However, features within the depth are more resolved due to a larger number of pixels that are assigned to the region. Conversely, if the spectral range captured on the detector is limited, therefore assigning a high frequency resolution, a larger imaging range is achieved. The trade-off is that features in the deeper region imaged cannot be resolved as well due to the finite number of pixels assigned for the entire depth.

Figure 17 demonstrates the relationship between frequency and spatial resolution for all three cases. In other words, when frequency resolution is high, spatial resolution is reduced. Conversely, when frequency resolution is lower, spatial resolution increases.

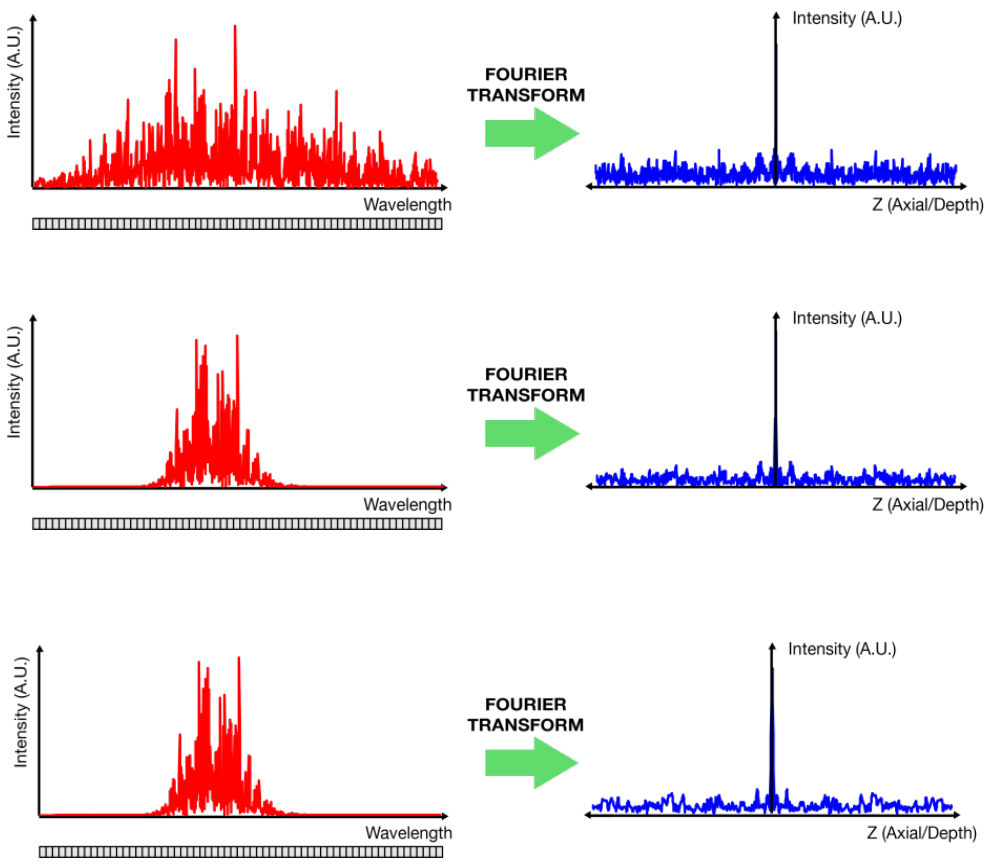

Figure 17 - Relationship between spectral range captured and imaging range in the spatial domain.

Chapter 3

System Design: Hardware

Chapter 3: System Design: Hardware

As described earlier, the OCT system design comprises a series of trade-offs in imaging and performance. This chapter documents the hardware considerations of the system design, including source selection, optical path design for reference and sample arms, and the detection arm, including the spectrometer and data acquisition system which detects and records the interference spectrum, respectively. The schematic and optical design of the OCT system which is discussed in this chapter is displayed in Figure 18.

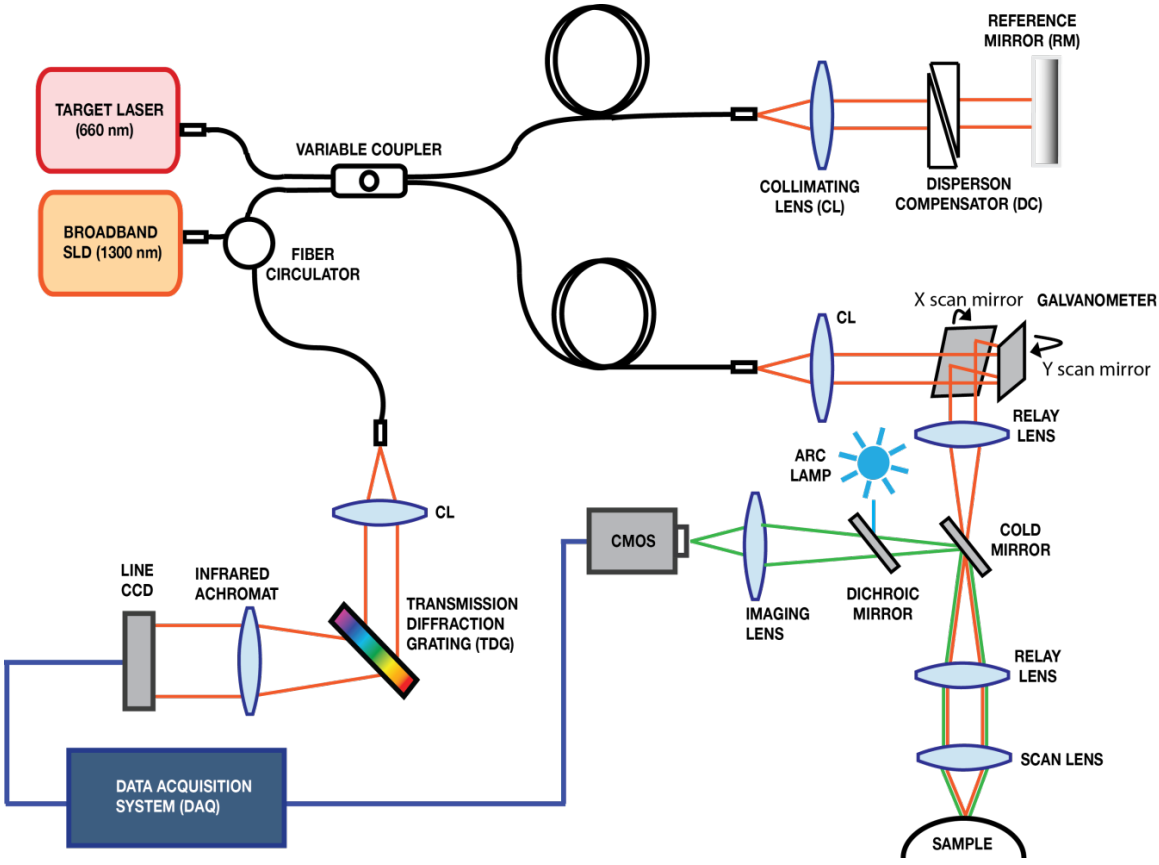

Figure 18 - Schematic of the designed SD-OCT system.

Design goals are three-fold in performance, flexibility, and ease of use. In terms of performance, a high-speed scanning and fast acquisition system is necessary for biological imaging with an acceptable imaging range on the order of millimeters with the ability to resolve few micrometer resolution vessels. Regarding flexibility, the mechanical design is considered for portability so that the system can be moved in surgery settings. The nature of brain scanning requires the system to be adaptable to surgery bays for small animals. The system design should be mechanically sound to reduce the vibration effects that may detract the quality of system calibration. Finally, user-friendly interface software should be developed for the system. Components were selected based on the calculated design parameters from readily available products in the market.

3.1 Source

The source plays a crucial role in the OCT system performance and should be elaborated on as a practical point for design considerations. Axial resolution of the system is dependent on the source bandwidth. Absorption and scattering of light, specifically biological tissue in this application, degrades signal strength with depth. Penetration depth suffers from weak reflection due to material attenuation. Scattering is largely dependent on the wavelength, and in higher wavelengths less scattering is observed [12]. Penetration depth is determined by the source central wavelength. The absorption coefficient as a function of light wavelength is shown in Figure 19 for biological tissue constituents in the brain. Those shown in the plot include oxygenated hemoglobin HbO_2, deoxygenated hemoglobin *deoxy-Hb*, bulk

lipids and water H_2O. This range exhibits the optical window for wavelengths that are less absorbed within tissue. The window where the least absorption for all occurs is approximately between 780 – 820 nm. In ophthalmic imaging, a source wavelength between 800 – 850 nm is commonly used. This band is particularly useful for eye imaging due to the low absorption of light. Ophthalmic applications aim to image the retina, located in the posterior of the eye. Light must pass through ocular media, including the fluid region of the vitreous of the eye before reaching the retina. To maintain scanning reliability, minimal absorption is desirable. For dense materials, imaging in the 800-850 nm region limits the achievable penetration depth due to scattering. In transparent tissue such as the eye, scattering is not as prevalent and as a result, this band is useful for ophthalmic imaging.

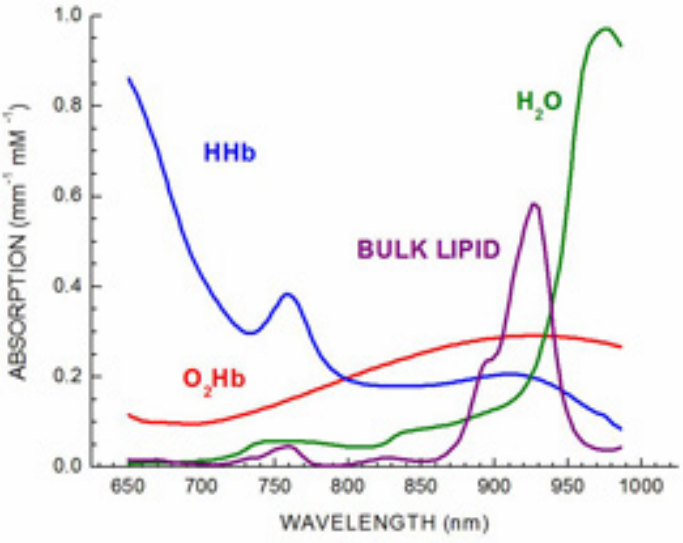

Figure 19 - Absorption coefficient in biological constituents [16]

As wavelength increases, absorption also begins to increase for most biological constituents. Water absorption rises steeply as the wavelength increases

above 950 nm. Scattering in higher wavelength bands; however, is decreased which allows longer imaging ranges in the tissue. This consideration is important for nontransparent tissue suffering from scattering in shorter wavelength. Sources in the near-infrared range, such as 1310 nm, are often used in OCT for the benefit of an increased imaging range, despite higher water absorption. Wavelength compatible components are readily available in the 800-850 nm range as well as 1310 nm, making implementation equally accessible for either source selection.

As mentioned previously, the interference spectrum is the autocorrelation of the source electric fields. The autocorrelation of a Gaussian function is another Gaussian, thus an approximately Gaussian source spectrum is ideal. The coherence length for a Gaussian-distributed type source determines the axial resolution defined previously in Equation 3. The axial resolution depends on the FWHM of the source, which is the coherence length. From the inversely proportional relationship, it was understood that higher resolution imaging requires broad source bandwidths in low-coherent interferometry. Low coherent sources, such as SLDs are readily available in the market with sufficient output power on the mW range for a fairly low cost. Femtosecond lasers are known for their broad bandwidths, and are another viable source option, though at a much higher cost considering today's technology.

SLDs are attractive sources for implementation of OCT systems due to their low cost, compact geometry, availability and reliability. This is instrumental in the signal processing and detection of interference in OCT. Lasers traditionally produce a high output power over narrow spectral widths. Light-emitting diodes (LED) are

forward based *p*-*n* junctions, providing light via spontaneous emission. Injecting current into an LED causes a recombination of electrons and holes in the *p*- and *n*-type regions respectively, resulting in spontaneous emission [17]. The emission occurs over the entire bandwidth of the gain medium, resulting in a broad spectrum.

SLD combines the reliable output seen in laser diodes while having a broad optical spectrum. The intensity on the produced optical power is based on the bias current of the diode. SLD power output holds two dependencies, with an exponential relationship for optical gain and a linear relationship for spontaneous emission [18]. In SLDs, gain occurs due to higher injection currents; and higher modal gain is observed in comparison to laser diodes.

Often to increase the bandwidth of the source, the beam of two SLDs are combined to achieve a broader bandwidths [13] [12] [19]. Coupling two SLD outputs has been demonstrated to improve the axial resolution, as demonstrated in the plot of Figure 20.

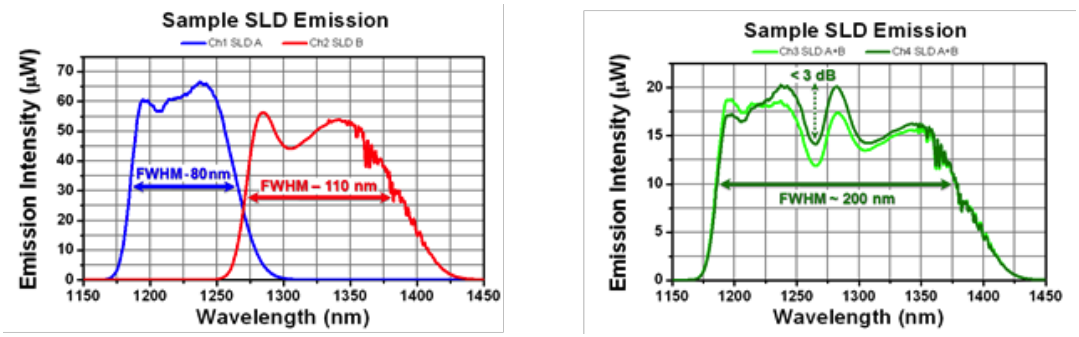

Figure 20 - Combined channel emission of the extended broadband SLD source. Figure adapted from [20].

The spectrum can be extended to achieve a wider bandwidth for high-resolution imaging. Combining dual sources yields a higher output power, and each source may also be operated independently, based on the source architecture.

A source in the near-infrared range was selected for the system to attain deeper penetration depth of dense brain tissue. SLDs with nominal wavelengths of 1300 nm usually have a bandwidth between 90-100 nm. An extended broadband SLD light source (LS2000B, Thorlabs, Inc., Newton, NJ, USA) was chosen for the project. Combining two SLDs with a central wavelength of 1225 nm and 1340 nm, with a bandwidth of 80 nm and 110 nm respectively, yields a center wavelength of 1300 nm and a typical combined bandwidth of 200 nm with an output power of 10 mW. Theoretically, the axial resolution of the system can be found using the following formulation:

$$\Delta z = \frac{2\ln(2)\lambda_0^2}{\pi\Delta\lambda} = \frac{2\ln(2)\times(1310\ nm)^2}{\pi\times 200\ nm} = 3.787\mu m$$

A sample spectral emission of the source is shown in Figure 20. In the first image, emitted power of the independent sources are shown, and in the second image, a larger bandwidth is synthesized by combining sources.

3.2 Interferometer

The interferometer lies at the heart of the OCT system to relay the light beams from the source, reference and sample arms to the detection and data acquisition module. Interferometry can be achieved by transmitting the light beams through free space or optical fibers. Fiber optic connectors reduce the potential for misalignment in both arms because of it is a modular optical wave guide. Using

fibers also increase the system's mobility to be transported with minimal risk of misalignment. Fiber optic cables in the 1310 nm wavelength range are readily available since these fibers are widely used in optical telecommunication systems. The module connectors seen in the system are single mode fiber connectors with angled physical contact (FC/APC) patch cables, with 8° angled fiber ends, to minimize back reflections. Insulation for the conveyance cables provide further protection to ensure system performance reliability and protection from optical interference that may potentially affect measurements.

A variable coupler was used as a beam splitter in the configuration, for adjustable power to be directed to equidistant sample and reference arms. A variable coupler is used to divide the optical power between the sample and reference arms to optimize interference power ratios, where a majority of the power is directed to the sample arm. A variable coupler (Model 905 Variable Ratio Coupler, Evanescent Optics, Inc., ON, Canada) was chosen with one micron of motion per 0.001 inch division. An unbalanced configuration compensates for the significantly weaker sample arm signal. An optical circulator (CIRC1310-APC, Thorlabs, Inc., Newton, NJ, USA) was added and serves to isolate beam based on their inherent characteristic of being non-reciprocal devices. In addition, the circulator will protect the SLD from back reflections by sending signals through one direction only. The reference and sample arm beams are recombined at the variable coupler and to the diffraction grating, which projects onto the line CCD camera.

Polarization of the transmitted light was maintained using polarization controllers along the interferometric path. Birefringence in optics may potentially

alter the polarization of the electric field, and maintaining a uniform polarization states for electric fields in both arms are required for interference to occur. Elliptically polarized light is converted by looping taught fibers around spools to create a wave plate, where each spool is representative of a wave plate. This stress-induced birefringence maintains polarization of the transmitted light. Birefringence is a function of the fiber cladding diameter, spool diameter, the number of loops per spool and the wavelength of light, which is adjustable accordingly. The diameter is fixed and equal for all spools.

3.3 Sample Arm

The sample arm consists of multiple elements within its path. The scanning path sends light to the sample, and also is the return path of the backscattered signal for interference. The optical system of the scanning path is common to SD-OCT imaging modalities and is limited by constraints of the axial and lateral resolution. An additional light path adjacent to the scanning path was added for optogenetic stimulation. The combined optogenetic path allows simultaneous stimulation and imaging. A cold mirror operates to transmit light infrared (IR) light while reflecting visible light. This filter is used to filter the IR light from visible light in the sample arm. Fluorescent imaging was added to the path in conjunction with the optogenetic stimulation. A dichroic mirror has the ability to reflect or transmit light above or below a specified wavelength. To capture images from the sample path for verification purposes, a dichroic mirror was added behind the cold mirror.

3.3.1 OCT Scanning Path

The sample arm, equidistant to the reference arm, encapsulates the optical path within a scanner head used for scanning the sample. The arm is mounted on a six-axis double arm boom stand (Diagnostic Instruments, Inc., Sterling Heights, MI, USA) to provide flexibility in varying experimental environments. The scanner head is mounted on a removable custom base plate secured to the boom. The plate can be removed for placement in an alternate stand. The sample path includes the OCT scanning elements, actuated by galvanometer scanning mirrors, and focusing optics to relay sample backscatterers to the variable coupler for recombination with the reference arm beam. Inside the sample arm, collimated light enters two single axis x- and y- scanning mirrors (GVS002, Thorlabs, Inc., Newton, NJ, USA) to produce a two-dimensional raster scanning pattern. The scan pattern is projected through relay lenses (CaF_2 Bi-Convex Lenses, LB5284, Thorlabs, Inc., Newton, NJ, USA) and a 10X scan lens (LSM02 10X, Thorlabs, Inc., Newton, NJ, USA). The back reflected beam is transmitted through the same path for interference with the reference beam, and then circulated before being sent to a collimator lens that is the gateway for the detection arm. The collimated beam is diffracted through a transmission grating and projected onto a high speed line CCD InGaAs camera (SU-LDH2 Goodrich Digital Line Scan Camera, Sensors Unlimited, Inc., Princeton, NJ, USA). A high resolution USB CMOS camera (DCC1645C, Thorlabs, Inc., Newton, NJ, USA) is attached to the scanner head and captures fluorescent images through a dichroic cube within the lens system. For optogenetic stimulation, 470 nm excitation light (Lambda DG-4, Sutter Instrument Company, Novato, CA, USA) is pulsed through the

dichroic filter onto the sample while simultaneously acquiring tomographic scanning and fluorescence imaging.

3.3.1.1 Scanning Relay

In all optical design considerations, a high coupling efficiency of the lenses is desirable; in other words, a lower power loss between connection points of the system. Furthermore, the consistent relay of a clear sample spot profile is also considered. A clear sample spot profile is instrumental due the spot scanning nature of OCT [12].

An incident beam initially enters the sample arm through a collimated lens. Collimating the light beam reduces divergence and power loss of the light beam. A smaller beam diameter permits the use of smaller scan mirrors, beneficial to attain high-speed scanning. With increasing scan mirror size, imaging is inherently slowed due to mechanical limitations of rapidly moving a larger mirror. The mirror dimensions should exceed the maximum beam diameter size to ensure complete beam transmission, while selecting the smallest size possible to maintain speed.

Using Gaussian beam optics, the beam waist size can be determined. The collimating lens (F280APC-C, Thorlabs, Inc., Newton, NJ, USA) has a focal length $f = 18.67\ mm$ and $NA = 0.15$. The beam spot size is defined as:

$$\boldsymbol{w(z) = \sqrt{w_0^2 + \left(\frac{\lambda_0 z}{\pi w_0^2}\right)^2}} \qquad \textbf{Equation 6}$$

where z is the axial distance from the beam waist radius, λ_0 is the source center wavelength and w_0 is the beam waist radius [21]. The beam waist radius is determined from the $\frac{1}{e^2}$ point or 86% of the diameter at one focal length from the lens. It is assumed that the beam will travel the maximum distance of the OCT imaging range of 1.6 mm. The beam waist radius is 1.65 mm. The spot size at 1.6 mm is 15.7 mm. The relationship between beam spot size and distance is plotted in Figure 21.

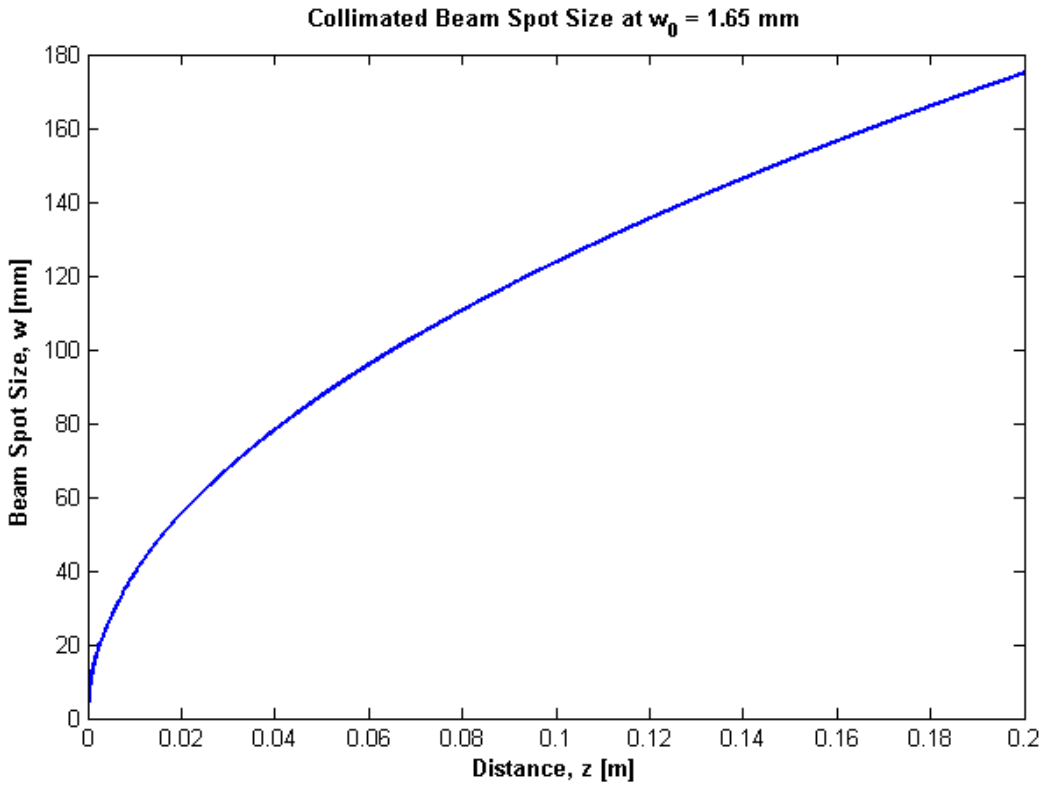

Figure 21- Beam spot size in relation to collimated beam spot size

The scan mirrors are fitted for beams diameters less than 5 mm, with the x-axis mirrors measured at 10 mm x 8 mm and the y-axis mirror at 8.5mm x 14.5 mm.

At the 1310 nm wavelength range, the silver coated scan mirrors are rated for more than 98% reflectivity. Galvanometer considerations include the angular acceleration of the rotational shaft for mirror positional control and the size and shape of the mirror. To ensure high-speed compatibility, a galvanometer was selected with angle response times in the 300 – 400 μs range. The mirrors in the system do not exceed moving more than $\pm 3°$, though the mirrors rated for a maximum scan angle of $\pm 12.5°$. To relay the image, a pairing of bi-convex lenses are used with $f = 50\ mm$ and a diameter of$25.40\ mm$. With positive bi-convex lenses, focusing of a collimated beam occurs behind the lens. Using a two-lens relay system, a cold mirror lies between the focal point of both relay lenses. The beam moving towards the sample arm optics is then a collimated beam.

3.3.1.2 OCT Scanning Path: Sample Arm Optics

The sample arm optics was selected accordingly to maximize the lateral. Axial resolution is not considered since it is only dependent on the source and will not affect the optical design path for scanning. Careful selection of the source will provide the smallest axial resolution possible.

The depth of focus and lateral resolution are related inversely; however, a high lateral resolution and depth of focus is desirable. The governing equations (Equation 4) show the depth of focus is twice the Rayleigh range and the numerical aperture of the selected objective lens affects the resolution, assuming a Gaussian OCT beam. A smaller spot size will decrease the depth of focus. Figure 22 shows an

image of the sample arm beam passing through the objective lens towards the sample.

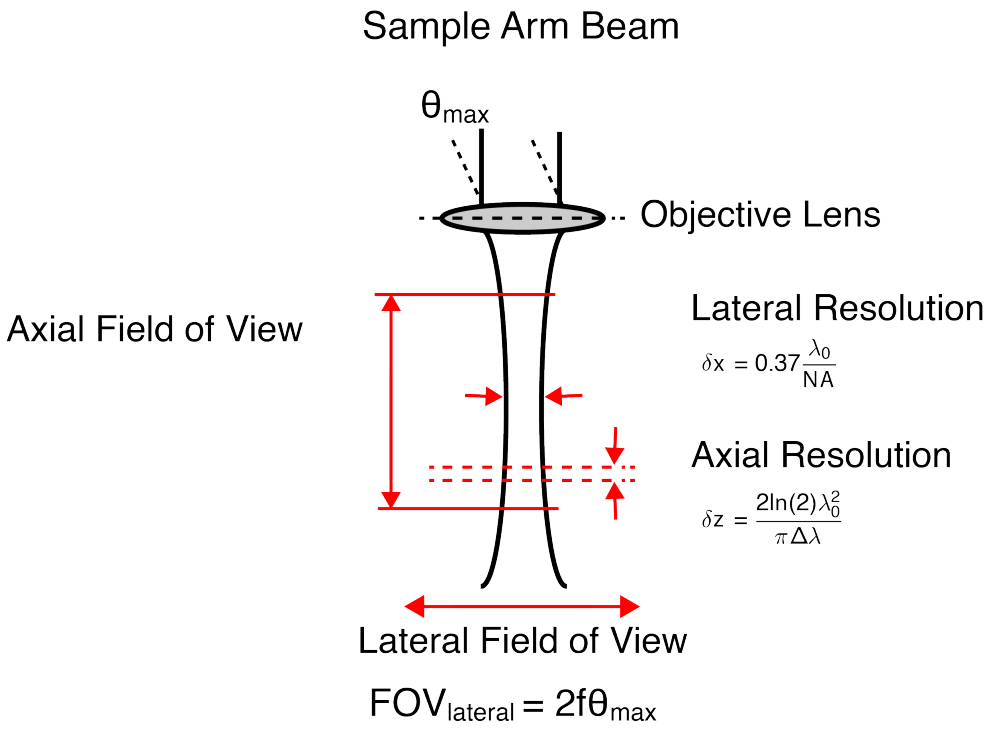

Figure 22 – Schematic of sample arm optics and spatial resolution relations.

The aperture of the lens needs to be sufficiently large to capture the full beam. The attained lateral field of view can be characterized by the following equation:

$$\boldsymbol{FOV_{lateral} = 2 \cdot f \cdot \theta_{max}} \qquad \textbf{Equation 7}$$

In lieu of an objective lens, a telecentric 'scan' lens was used to focus the beam at the sample. The hallmark of a telecentric optical system is the resultant spatial conservation of the imaging plane, minimizing the need for additional image

processing. The scan lens does not produce spatial aberrations along the imaging plane that would otherwise be caused by a regular objective lens. The scan lens provides constant magnification over the field of view and holds a constant spot size. A smaller spot size corresponds to a higher NA of the lens. However, a higher lateral resolution, with a larger NA will result in a shallower depth of field.

The scan lens selected, LSM02, provides 10X magnification with maximum scan angle is 7.5° and an effective focal length of 18.02 mm. This provides a lateral field of view of 4.3 mm. Based on Equation 4, the theoretical system lateral resolution is found to be6.39 μm:

$$\Delta x = \frac{4\lambda f}{\pi d} = \frac{2\lambda}{\pi NA_{obj}} = 6.39\ \mu m$$

3.3.2 Optogenetic Stimulation Path

The optogenetic path serves to relay light through the same path as the OCT scanning to simultaneously stimulate the brain during SD-OCT image acquisition. Optogenetic stimulation uses light in the visible range to activate neuron ion pumps to induce activity in the brain. Depending on the ion pump stimulated, the neuron action potential is excited or suppressed. Any change induced in the hemodynamic signal as the result of stimulation will be detected in processing using the SD-OCT system software. The system was designed to detect excited neurons using ChR2. The path accommodates the propagation of blue light (470 nm), selected based on

the opsin response to this wavelength. The microbial opsin gene is tagged with a YFP as its biomarker.

The optogenetic stimulation path is adjacent to the SD-OCT sample arm path. Since the light will need to reach the sample, the stimulation path is combined with the sample arm. Light from an arc lamp is pulsed and passed through a dichroic filter (MD515, Thorlabs, Inc., Newton, NJ, USA). With a transition wavelength of 515 nm, wavelengths below are reflected and wavelengths above are transmitted. This transmission profile is shown in Figure 23. The filter is placed in a dichroic cube, angled at 45°. The reflected beam travels to a cold mirror, which is at the focal point of the relay lenses of sample arm scanning optics. This beam propagates alongside IR light to pass through a relay lens and a scan lens before being illuminated onto the cortical surface.

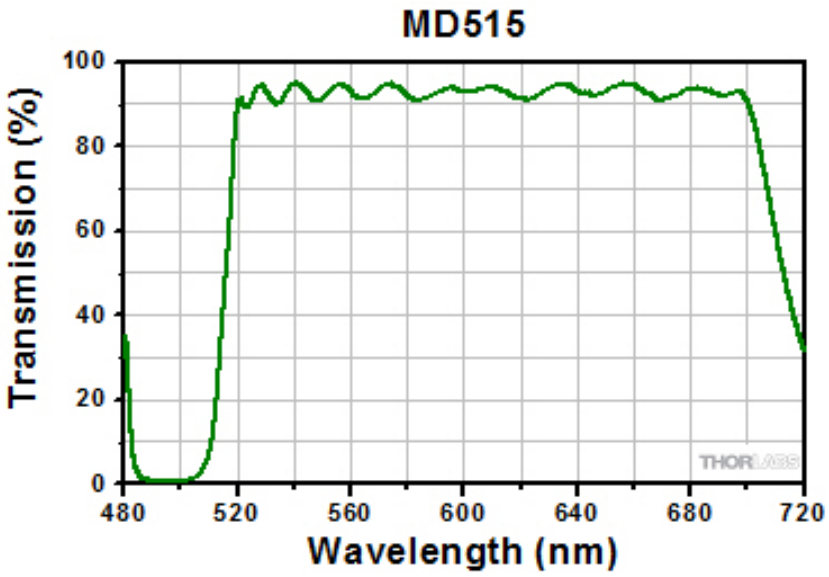

Figure 23 - Transmission profile of dichroic filter MD515, reflection band = 490 – 510 nm and transmission band = 520 – 700 nm. Figure adapted from [10].

3.3.3 Fluorescent Microscopy Path

The fluorescent proteins used in the microbial opsins are fluorophores that emit green light when illuminated with blue light. The presence of fluorescence provides verification during optogenetic experiments, providing another degree of verification.

Fluorescent microscopy utilizes an excitation filter, emission filter and dichroic filter. The excitation filter grants passage of a band of wavelengths, depending on the design, where wavelengths within the bandpass are transmitted. The emission filter allows the desired wavelength to be transmitted to the photodetector. The reflection and transmission spectrum is dependent on the dichroic mirror. The dichroic mirror reflects light up to the transition wavelength, and transmits other wavelengths. The diagram for a fluorescent microscope is shown in Figure 24.

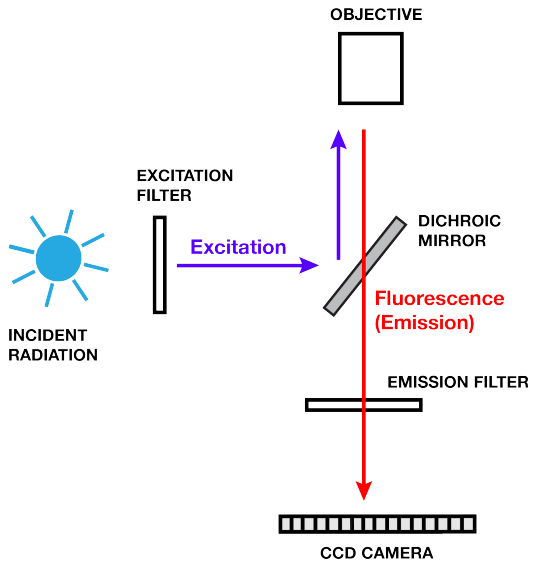

Figure 24 - Schematic of a fluorescent microscope.

The fluorescent microscopy path in the OCT scanning path uses a filter with a transition wavelength of 515 nm. The transmitted wavelength is passed through a green emission filter. The light is sent through an imaging lens, after which is captured on a CMOS camera. The camera is operated outside the LabVIEW interface with proprietary software included with the camera. The camera can be used for fluorescent or bright-field imaging. Bright-field imaging does not use blue light stimulation, but captures the broadband image, which can be used for comparison of OCT images after processing.

3.4 Reference Arm

The reference arm serves to create a path length difference between the interference of sample and reference arms. The reference arm is used to align the system into focus. The reference arm is used in alignment where the path between the mirror and dispersion compensator can be adjusted using a micro-positioner to focus the beam. Optics of the reference arm do not need to meet any design criteria of the beam, so the optical design in the reference arm mimics those of the sample arm to reduce the blurring effect due to mismatch.

Light from an optical fiber is sent to a collimating lens with a focal length of 20mm, collimating the diverging beam. The beam passed through a 45° angled slab of glass, then sent to a dispersion compensating lens to minimize the effects of dispersion and avoid additional processing loading by compensating for dispersion

numerically. The 1mm glass located at the entry of the light path works to compensate the cold mirror in the reference arm, where the cold mirror is essentially a 1mm slab of glass with special coating. After the dispersion compensator, light is reflected from a gold mirror at the end of the arm.

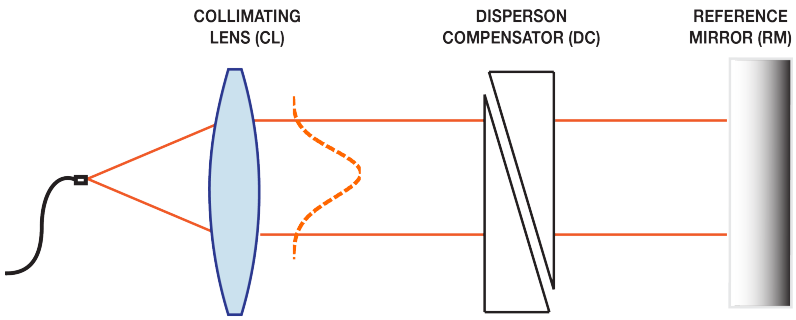

Figure 25 - Schematic of the reference arm.

The signal is typically stronger in the reference arm than the sample arm, causing a tendency of the signal to saturate due to the highly-reflective mirror. The reference signal is essential in post-processing to serve as a point of reference, which is described in later chapters. A lower amount of power can be directed to the reference arm using the variable coupler to reduce optical power. This also benefits the sample arm by increasing the amount of optical power, providing amplification to weakly backscattered signals.

3.5 Detection Arm

The detection arm provides the framework for recording the spectral interference pattern from scanning, where a spectrometer captures the interference

for wavelengths within the source bandwidth. The detection arm consists of a spectrometer, whose design will be described further, and a data acquisition card installed into the OCT computer.

3.5.1 Spectrometer Design

The spectrometer measures the optical energy, which is the interference spectrum. The wavelength components of the incident beam are separated using a dispersive device, such as s prism or diffraction grating. Once separated, the components are projected and captured on to a photodetector, in this case a line CCD camera.

For the spectrometer, a collimating lens, transmission diffraction grating, IR achromat lens and line CCD camera is used. Selection of these components can be customized to the system. The beam is collimated through a collimating lens before passing through the grating. An infrared achromat is used to parallelize the spectrum before being recorded on the camera. The schematic for the spectrometer is shown in Figure 26.

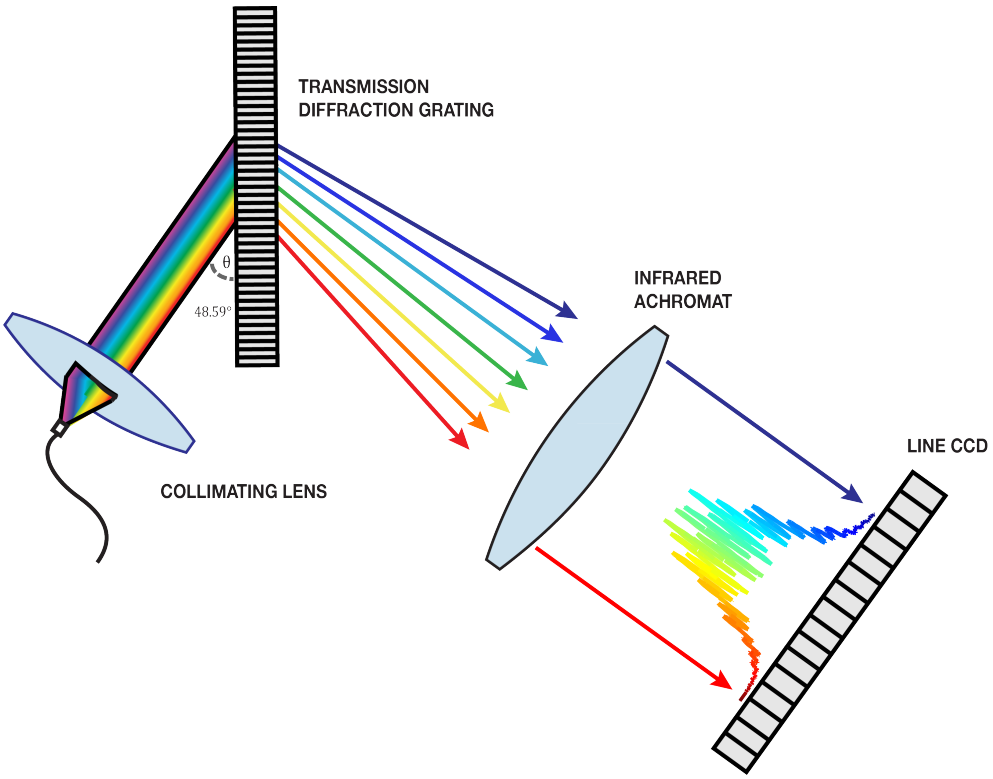

Figure 26 - Schematic of the spectrometer in the system.

A transmission grating is employed for separating the wavelength components. Incident light on the grating is spectrally dispersed and transmitted on the opposing side of the grating. The diffraction grating is governed by the grating equation:

$$\boldsymbol{m\lambda = d(\sin\alpha + \sin\ \beta)} \qquad \text{Equation 8}$$

where m is an integer diffraction order, λ is the wavelength, d is the groove spacing, and α and β are angles of the incident and diffracted rays. The right hand term represented by $d(\sin(\alpha) + \sin\ (\beta)$ is the path difference of rays from adjacent grooves. These relations are shown in Figure 27.

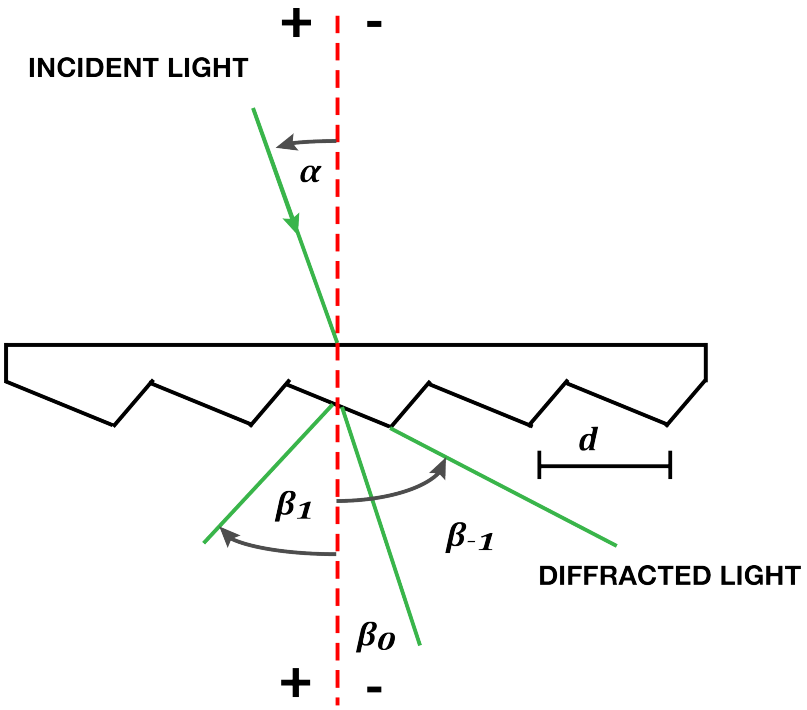

Figure 27 - Transmission diffraction grating.

The intensity spectrum is captured as a function of wavelength. The line CCD camera measures photoelectron charges as a function of exposure time τ. The number of photoelectrons n_e are related to the optical power and photoelectric current by the equation:

$$n_e = \frac{\eta P \tau}{h\nu_0}$$

where η is the detector quantum efficiency, h is Planck's constant and ν_0 is the center frequency of the light source [15].

A CCD camera intrinsically carries noise, including Johnson and dark noise, along with flicker noise. Flicker noise, also called 1/f noise, is dependent on the

frequency of acquisition. Flicker noise can be neglected with exposure times less than 1 ms. Additionally, the number of pixels in the line CCD camera means that the captured interference spectrum will be a discrete set of points *N*, where *N* is the number of detectors on the line camera. The captured spectrum and detector relates to the maximum imaging range that can be imaged using the system. The detected spectrum is approximated by the equation:

$$\Delta\Omega = 2\pi c \frac{\Delta\lambda}{\lambda^2}$$

where *c* is the speed of light, or $3\times10^8\ m/s$, $\Delta\lambda$ is the source bandwidth and λ is the source center wavelength. However, the captured spectrum is limited due to the number of pixels used in the camera.

Maximum penetration depth can be expressed as:

$$z_{max} = \frac{\lambda_0^2}{4n_{ave}\Delta\lambda} N$$

where n_{ave} is the average refractive index of the sample. Figure 28 shows the relationship between maximum penetration depth and bandwidth, which are inversely proportional to each other. For the device developed, assuming an average refractive index in the brain n_{ave} = 1.4, the theoretical maximum penetration depth is found to be 1.6 mm from the calculation:

$$z_{max} = \frac{(1310\ nm)^2}{4(1.4)(200\ nm)} 1024 = 1.6\ mm$$

As seen earlier, the spectrum range is inversely proportional to the penetration depth, and resolution is limited by the number of pixels on the line CCD camera. Thus, a greater spectral range provides a smaller imaging depth, however more features are mapped on to the pixels providing higher imaging resolution.

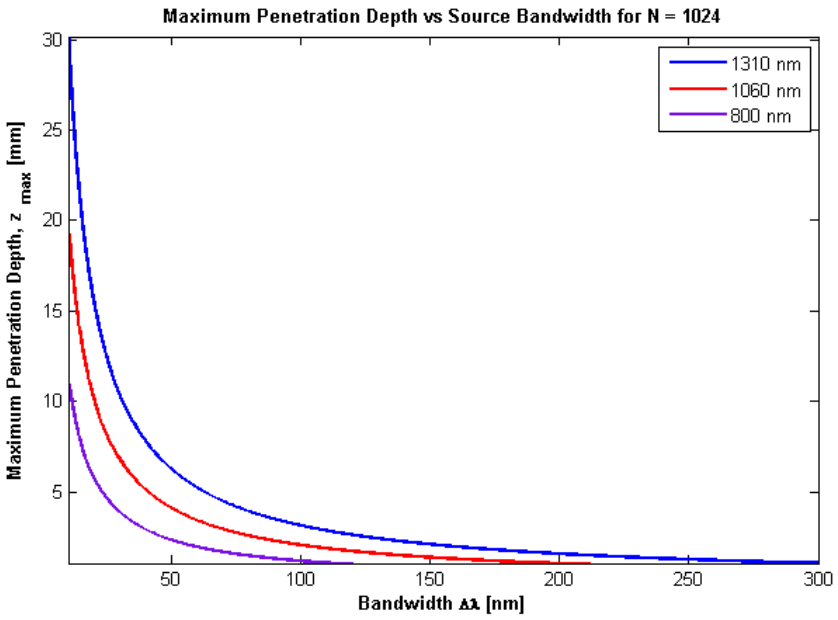

Figure 28- Maximum imaging depth for a detector with 1024 pixels.

3.5.2 Spectrometer Design: Diffraction Grating

A dispersive element is used to separate the wavelengths of light. A 1-inch transmission diffraction grating was selected with 1145 lines per mm with a center wavelength of 1310 nm (Wasatch Photonics, Inc., Logan, UT, USA). The wavelength elements are dispersed at varying angles, depending on the wavelength. The grating has an incident angle of 48.59°. A uniform grating efficiency is desirable in the grating response for S- and P-polarized waves.

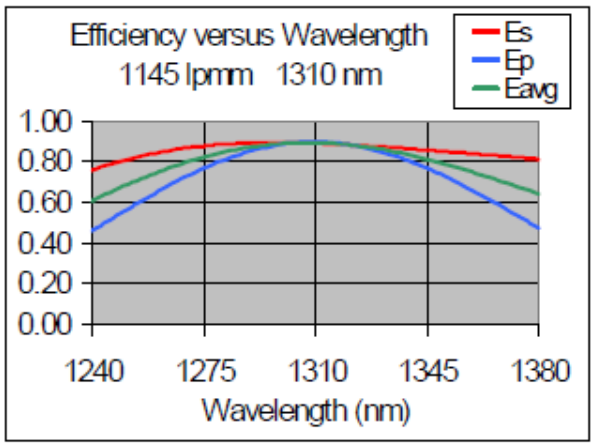

Figure 29 - Efficiency versus wavelength for the diffraction grating. Figure adapted from [22].

3.5.3 Spectrometer Design: Detector

A fast detector is required to simultaneously image the interference spectrum at a high speed. A line CCD camera (SU-LDH2 Goodrich Digital Line Scan Camera, Sensors Unlimited, Inc.) was selected with 1024 pixels at 12 bits. The camera has the ability to capture 91, 911 A-lines per second. Based on this scanning rate, the fastest integration time is 6 µs. A pixel height of 25µm was chosen to increase ease in alignment with 25µm pixel pitch. The camera has a desirable flat quantum efficiency region for wavelength ranges within the infrared region used by the source, as in Figure 30. A stable quantum efficiency region will ensure the most efficient integration time to ensure reliable scanning. At the time, in September 2012, the camera was the fastest available on the market.

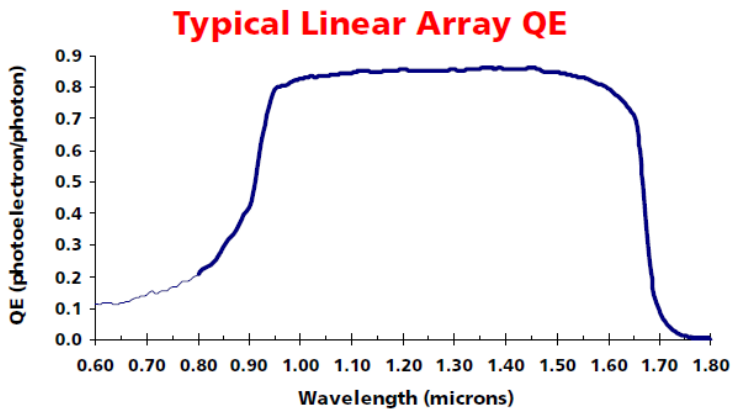

Figure 30 - Typical quantum efficiency of the line CCD camera. Figure adapted from [23].

3.5.4 Detection Optics

Beam collimation and focusing is achieved through optics in the detection arm before being projected for recording. Focusing optics will directly affect the quality of the recorded image. The detector in the arm records individual wavelength components in a finite space, and the space which the wavelength components of the beam occupy determines the sensitivity fall-off of the system. For these reasons, resolution, spectral response and spot-size should be considered in spectrometer optical design [12].

The spectral response of the detection arm considers the light path of travel before arriving at the detector. A non-uniform spectral response negatively affects the image by changing the axial resolution. Thus, changes between the coherence spectrum and source spectrum should be kept to a minimum and considered in the design.

An infrared achromatic lens was used to focus the diffracted beam for projection onto the CCD line camera. Achromatic lenses are useful to avoid

chromatic aberration while maintaining a diffraction-limited spot profile. Chromatic aberration results in distortion due to material dependent waveguide dispersion. For OCT systems, achromatic optics preserves the axial resolution and improves coupling efficiency [12].

3.5.5 Data Acquisition

After being recorded on the line CCD camera, data is sent to a computer for storage. Data acquisition is performed through the LabVIEW interface. Two National Instruments Data Acquisition Cards (DAC) were used, where data was saved as a 2D frame. The 2D images were acquired by the DAC and stored in a buffer during scanning, where the raw data was sequentially saved to a binary file for processing.

3.6 System Implementation

The OCT system implementation is shown in Figure 31. The OCT system is housed in a utility cart and is shown in Figure 31 in a surgery bay for an animal experiment. The OCT head is seen on the experiment table, above the animal. The maximum recording rate is 80,000 A-lines per second, limited by computer hardware. At faster recording rates, the computer's physical read/write time falls out of synchronization with the data acquisition.

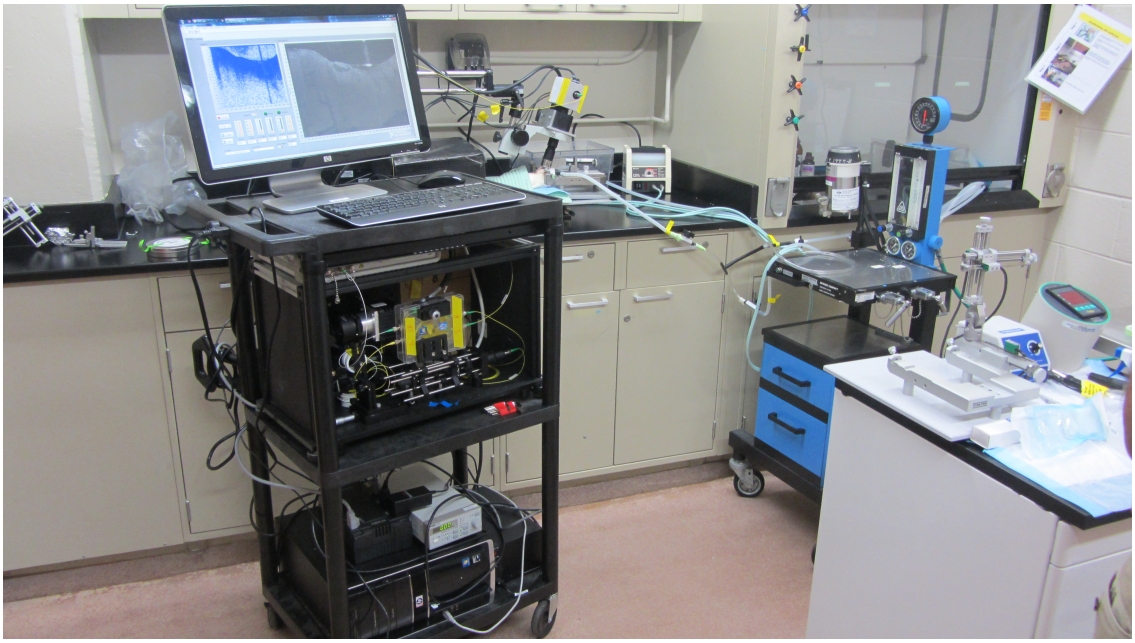

Figure 31 - OCT system during an optogenetic experiment in surgery bay.

Chapter 4

System Design: Software and Signal Processing

Chapter 4: System Design: Software and Signal Processing

Before performing more advanced image processing, a signal processing chain must be executed on the detected spectral interference pattern. In TD-OCT, the detected interference pattern, which was acquired in the time domain and captured as intensities on the photodetector, follows a minimal set of processing methods before reconstruction to a cross-sectional or volumetric image. This process typically involves demodulating the signal to achieve the A-line. In contrast, the SD-OCT signal processing chain is more sophisticated and more time consuming. This chapter will outline the standard signal processing chain, along with algorithms for advanced image processing including Doppler OCT and angiography that are used in this project.

Data from the detection arm is sent to a computer for processing. The algorithms were written in both MATLAB and C.

4.1 Pre-Processing

Rendering a useful image from the detected spectral interference pattern requires the wavelength domain signal be converted into the spatial domain. The end goal is to convert the starting spectrum into an axial scan, which is the depth reflectivity profile seen from TD-OCT imaging, accomplished by re-sampling and taking a Fourier transform of the spectrum. The signal processing chain for SD-OCT imaging is shown in Figure 32.

The interference spectrum is captured on a spectrometer using a line CCD camera. Since spectrometry measurements detect intensity as a function of

wavelength, the signal is expressed as $I(\lambda)$, with uniformly-spaced points. However, due to a non-linear relationship between λ and k, the Fourier transform will be unevenly spaced without re-sampling.

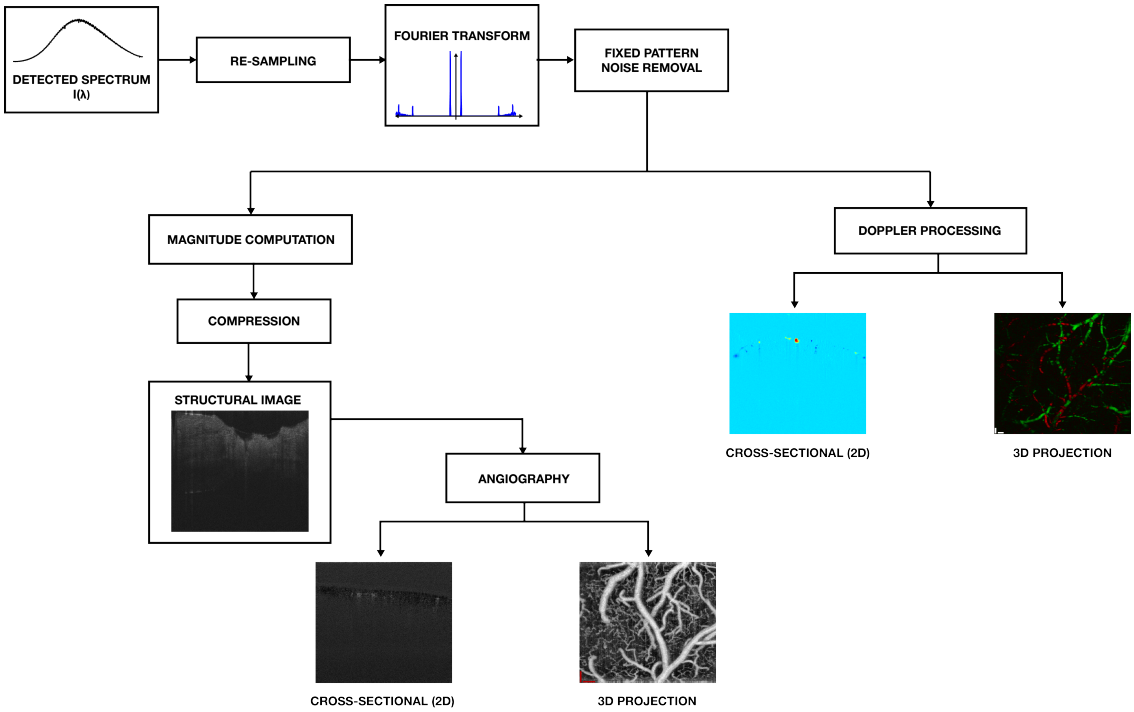

Figure 32 - Signal processing chain for SD-OCT images

First, the spectrum is re-sampled from λ to k-space prior to Fourier transformation. This conversion serves to attain uniformly spaced points after the spectrum is Fourier transform. The re-sampled signal $I(k)$ is then Fourier-transformed to achieve the depth reflectivity profile. It should be noted that a fast-Fourier transform (FFT) is used for its computational time advantage. Fourier transformation produces artifacts, mirroring the profile about the origin. The mirror artifact of the depth profile is redundant and discarded; thus only half the original

number of pixels is used. Once in the spatial domain, fixed pattern noise is removed. Source fluctuations and camera noise levels are active contributors to fixed pattern in the spatial domain. So, this noise is removed at each depth by subtracting the median of the 2D image at that depth. The FFT yields a complex depth profile; the magnitude of the complex signal is used to determine the structural image. Due to the absorption and logarithmic drop of SD-OCT sensitivity as depth increases, some non-linear transformations are needed to produce a uniform intensity across the depth. The last step is a reduction of the dynamic range to highlight structural features using a logarithmic compression.

4.2 Wavelength to Pixel Mapping

Prior to any signal processing, a spectrometer calibration is performed wherein the wavelength to pixel number relation is determined. The accuracy of the wavelength-to-*k*-space re-sampling is contingent on the accuracy of the pixel mapping process. The calibration process determines the relationship between pixel number and wavelength number. The objective is to determine the phase, and find pixel index values corresponding to evenly spaced phase values.

A strongly reflecting sample, in this case, a mirror is used. In ideal situation (having uniform sampling in the frequency space) the interference should be a sinusoidal. Of course amplitude of this sinusoidal is varying across the frequency, due to the variation in the source intensity. Hilbert transform of such a sinusoidal is almost a linear phase signal. This fact was used to calibrate signal. The calibration

process is as follows: first, the interference spectrum is band-pass filtered to remove the source spectrum and high-frequency noise. Then Hilbert transform of the signal is calculated. This signal is Fourier transformed where only the positive frequency is used. The magnitude is calculated, and the signal zero-padded and windowed. Finally, the mask is applied to the original Fourier transform of the signal. The resulting phase values are unwrapped and linearly interpolated to attain equally spaced samples. The results are shown in Figure 33.

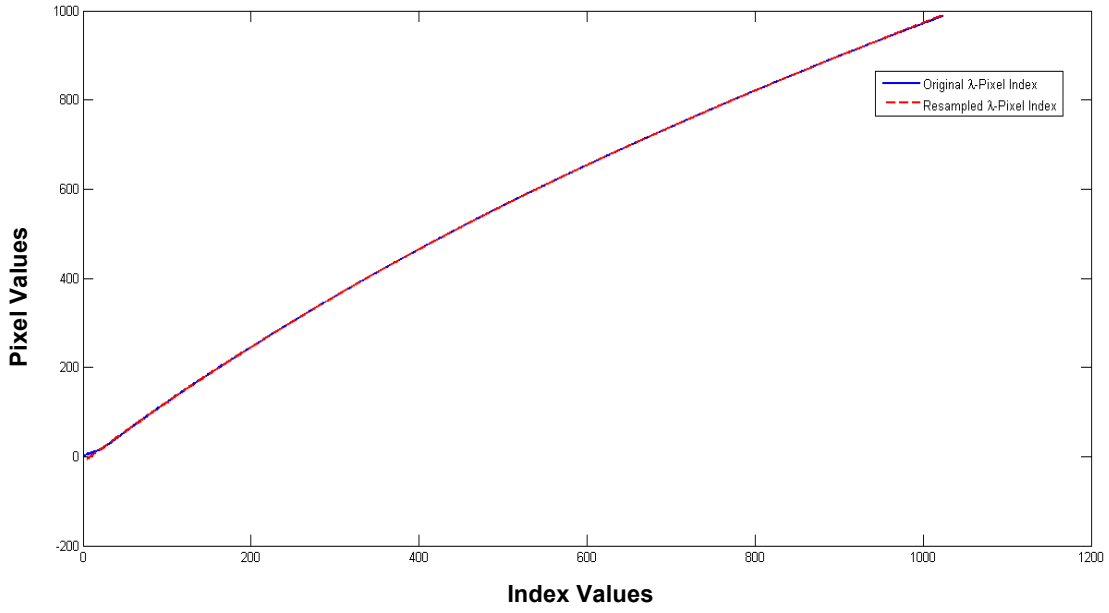

Figure 33 - λ-Pixel Mapping

4.3 Motion Compensation

Motion artifacts are inherent in imaging biological tissue as a result of animal motion (heartbeat and breathing), along with environmental motion such as table vibrations and galvanometer jitter. Motion artifacts may appear as vertical lines in

the image, distorting the view especially for high resolution imaging. A local motion compensation algorithm was developed to mitigate the effects of sample and mechanical variance observed within volumetric scans for angiography. Misaligned angiogram slices are corrected from multi-volumetric scans [19].

Supra-pixel motion was detected for each 5 A-lines and compensated for using cross-correlation maximization. Then sub-pixel motion was detected and compensated for, corresponding to two A-lines of the same transverse position for two separate B-scans. Since sub-pixel motion introduces a phase-shift in the axial direction, finding the phase shift in the axial direction estimates the sub-pixel motion between A-lines [24]. Shadowing effects due to scattering of RBCs was compensated for by a local phase compensation algorithm estimating the sub-pixel motion. Additional image enhancement may be used to improve the image further.

4.4 Angiography

Angiography using OCT is implemented by detecting the changes in moving scatterers. Visualization of vasculature networks is achieved by finding the changes in the red blood cells, changing the scatterer contrast with movement. Taking the difference between two A-scans captured at the same transversal position results in an angiogram. The scanning protocol for angiography requires a scanning rate typically at 40,000 A-lines per second.

Angiogram generation is dependent on continuity of adjacent scans from the same position, and errors significantly detract from the quality of an angiogram. Many factors contribute to noise in the angiogram, such as positional error and

photon shot noise. Animal motion (caused by heartbeat and breathing) and environmental vibrations, such as motion induced vibrational ripple on table surfaces and galvanometer motion, are attributed to positional error. Positional error results in decorrelation in the transversal direction. Decorrelation distorts the power spectrum signal, and results in a broadening of the signal. Depth and structural features are attributed to the phase component of the complex OCT signal, thus axial positional error results in a phase shift in addition to decorrelation. A local cross-correlation maximization algorithm is implemented to correct positional error before determining the angiogram, where

$$\boldsymbol{Angiogram} = |\boldsymbol{A_n} - \boldsymbol{A_{n-1}}| \qquad \textbf{Equation 9}$$

and *n* denotes the transversal position [19].

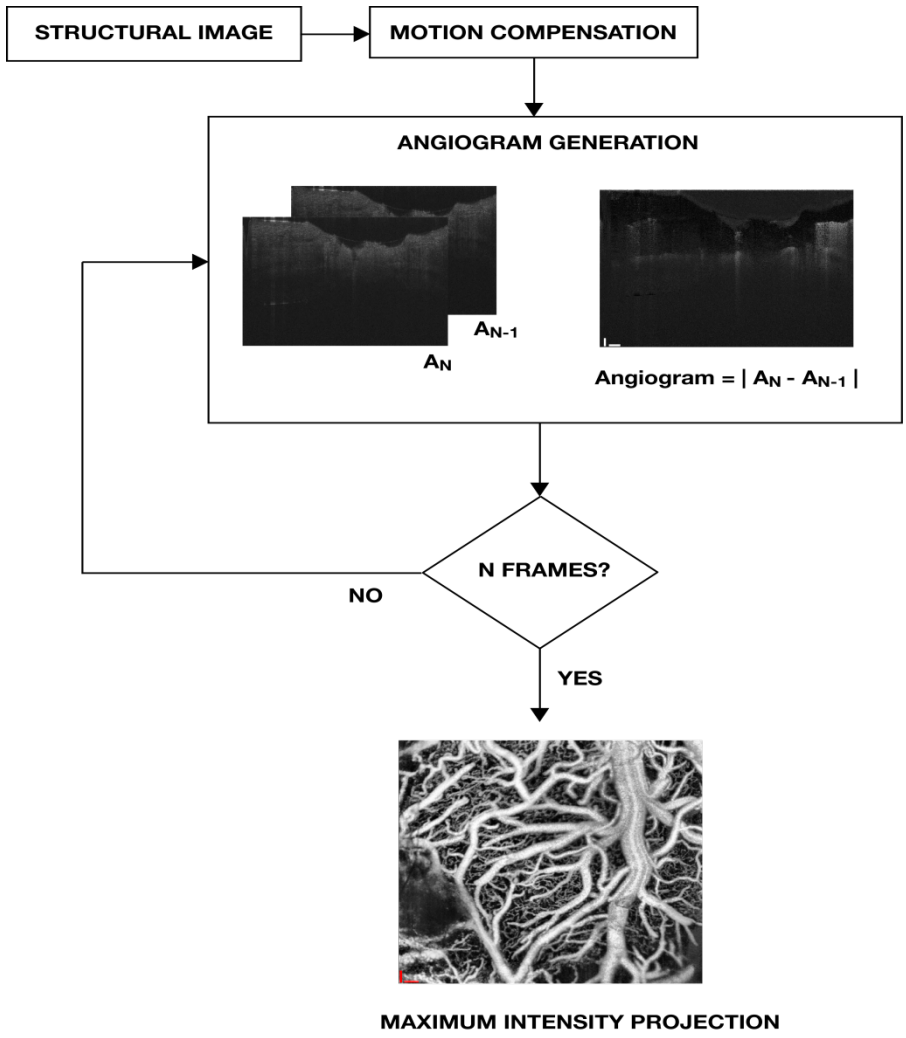

Figure 34 - Angiography processing flow chart.

To further improve the angiograms and compensate for motion artifacts, an additional step in the algorithm was included. For multiple 3D scans of the same volume, angiograms at each transversal position with the least motion are selected and averaged. A larger amount of pixel numbers relative to the average number of pixels for a feature is associated with increased motion. Thus, the average of the angiogram for each cross-section provided the metric for the amount of motion. A user-determined number *j* of cross-sectional images of the multi-volume 3D scans

with the least pixel values indicating the least motion, are selected for the angiogram. The *j* cross-sectional images are finally averaged for a 3D angiogram.

Angiograms are valuable in qualitative analysis of vasculature networks, however caution should be exercised when being used for quantitative data analysis. Changes in cross-sectional images are used to generate the angiogram, attributed to changes in movement of scatterers such as RBCs in the angiogram. An increase in intensity of the angiogram may not necessarily be the result of an increase in blood flow in vessels. Instead, this can be due to a change in the orientation of RBCs. Thus, another method must be used to quantify these velocity changes.

4.5 Doppler OCT

Doppler OCT is a method for determining quantitative fluid flow information based on interference of backscattered light from moving particles. Various Doppler OCT processing techniques have been developed [1]. In Doppler OCT, velocity estimation is determined by characterization of the Doppler frequency shift, f_D, which is associated with the phase of a complex OCT signal. The frequency shift is determined from cross-sectional structural images. The method of processing the structural images follow the same procedure described in Section 4.1 for OCT imaging. For the system, phase-resolved Doppler OCT (PR-DOCT) is selected for its faster processing and minimal computation requirement.

PR-DOCT calculates the phase change between adjacent scans to estimate fluid velocity. As stated earlier, velocity is related to the Doppler shift by the equation

$$f_D = \frac{2Vcos\theta}{\lambda_0} \qquad \text{Equation 10}$$

Phase change detection necessitates a complex OCT signal, which can be found from the Fourier transform of the original OCT signal since a Fourier transform is necessary in Fourier domain OCT imaging. The Doppler frequency shift is increased with an increase in the Doppler angle. When the Doppler angle θ is perpendicular to the direction of flow, the frequency shift detected will be zero. Practically, this means the incident beam illuminating the sample at an angle detects more of a frequency shift.

From the detected complex signal, the phase component of the signal can be found. The frequency shift for every pixel is the average phase shift of sequential A-scans. In other words, the frequency shift f_n is found as:

$$f_n = \frac{\Delta\phi}{2\pi T} \qquad \text{Equation 11}$$

$$= \frac{1}{2\pi T} \sum_{m=(n-1)M}^{nM} \sum_{j=1}^{N} \left[tan^{-1}\left(\frac{Im(\tilde{X}_{j+1}(t_m))}{Re(\tilde{X}_{j+1}(t_m))} \right) - tan^{-1}\left(\frac{Im(\tilde{X}(t_m))}{Re(\tilde{X}(t_m))} \right) \right]$$

Alternately, the shift can be re-written as:

$$f_n = \frac{1}{2\pi T}\tan^{-1}\left(\frac{Im\left[\sum_{m=(n-1)M}^{nM}\sum_{j=1}^{N}\tilde{X}_J(t_m)\cdot\tilde{X}_{j+1}^{*}(t_m)\right]}{Re\left[\sum_{m=(n-1)M}^{nM}\sum_{j=1}^{N}\tilde{X}_J(t_m)\cdot\tilde{X}_{j+1}^{*}(t_m)\right]}\right)$$

where $\tilde{X}(t_m)$ is the complex OCT signal and $\tilde{X}_{j+1}^{*}(t_m)$ is the complex conjugate of an adjacent scan. M is the window size in the axial direction for each pixel and N the number sequential scans for cross-correlation computation. T is the time difference between A-scans and $\Delta\phi$ is the minimum resolvable phase difference.

The dependence of PR-DOCT on the phase component makes the accuracy of this method susceptible to errors, particularly motion induced error which will cause possible change in the phase component. Phase stability will improve the minimum resolvable phase difference. SD-OCT systems have been documented to have a phase difference on the order of a few milliradians [1]. Thus, motion compensation should be implemented when calculating velocity. The spectrometer-based method found with SD-OCT reduces the amount of phase noise due to motion, since detection does not have any moving parts unlike other OCT modalities.

While faster A-line scan rates are desirable, the trade-off is a lower velocity sensitivity. Assuming a phase difference of $\Delta\phi = 10^{-3}$ radians, typical for FD-OCT systems, and an A-line scanning rate T of 80,000 A-lines per second, the minimum detectable velocity for a system with a central wavelength of 1310 nm is approximately 59.6 μm/s. Reducing T to be 40,000 A-lines per second, the minimum detectable velocity changes to 29. 8 μm/s. Additionally, flow direction is determined

by the sign of the detected velocity. A bi-directional flow can be detected using this method, with negative and positive velocity directions.

4.6 LabVIEW Software

A LabVIEW software was developed to accompany real-time image processing during a scanning procedure. The software was developed to be a user-friendly interface for ease of use and consists of two scanning modalities: 2D and 3D. A sample screenshot for cross-sectional imaging is shown in Figure 35. In the panel, the operator can evaluate system performance based on the spectral interference pattern and adjust the system variable coupler and choose to include an attenuator if necessary to improve the signal.

The main panel displays the structural cross-sectional image of the sample. The operator can select to view an A-line from any transversal position of the image. When the Doppler view is selected, the Doppler image is shown on the display left of the cross-sectional image. The Doppler display can be turned off by the user at any time to reduce the computation load for slower processors. The computer used for the system is Hewlett-Packard HPE-112y, 64-bit operating system with ADM Phenom™ II X4 925 Processor (2.8 GHz) and 8 GB RAM.

Control panels also give the user flexibility in adjusting the scanning protocol including hardware, scanning and image processing parameters. When optogenetic stimulation is turned on, clock signals are sent to pulse the arc lamp. In addition, the number of scans is determined by the user, along with the A-line scanning rate up to 80,000 A-lines per second. The angle of the scan pattern can be determined by the

user, and verified visually using the CMOS camera interface. The duty cycle of the linescan CCD camera can be adjusted to increase or decrease the exposure time of pixels.

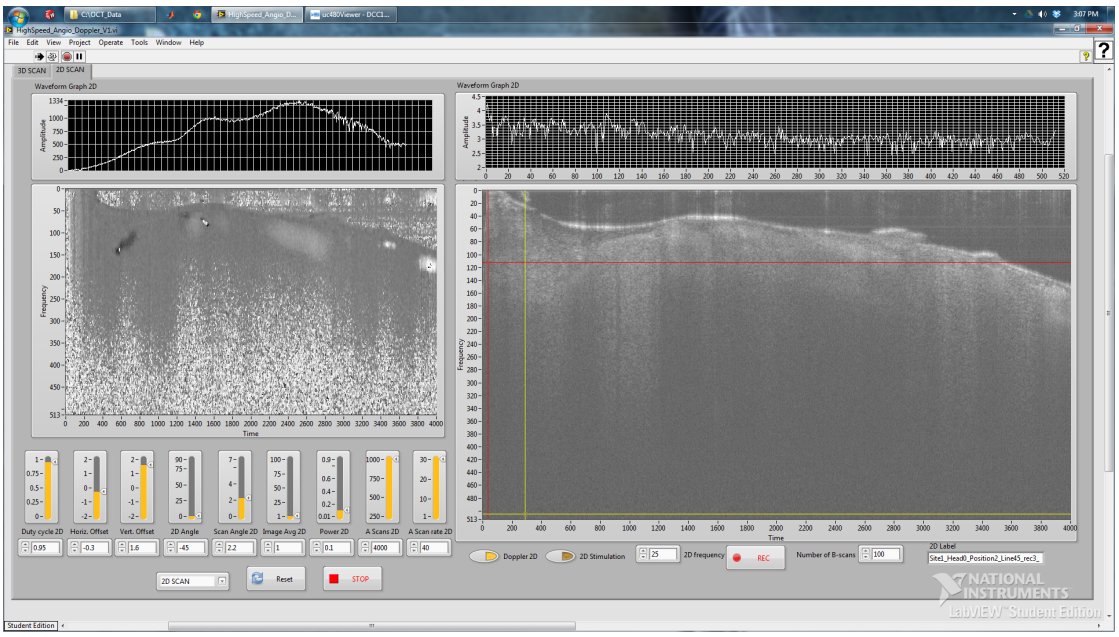

Figure 35 - LabVIEW interface of the developed OCT software.

Chapter 5

System Design: Image Enhancement and Analysis

Chapter 5: System Design: Image Enhancement, Representation and Analytics

In addition to standard data processing for cross sectional images, several algorithms can be applied in MATLAB for image enhancement and representation, including de-shadowing, additional background subtraction and contrast enhancement. Furthermore, automated analysis algorithms are developed for the images.

5.1 Shadow Removal

Blood vessel imaging suffers from shadow artifacts due to signal attenuation, scattering and absorption. The result of this is shadow artifacts in the structural images trailing vessels and veins. Since angiograms are based on the structural image, this artifact is observed in angiograms as well. Shadowing results in weakly reflecting structures in deeper regions which are obstructed by shadows of larger vessels and reduces visibility in depth. OCT signals are interferometric signals which measure the pulse-echo time delay. A method based on correction of attenuating sound waves was used to remove shadows in [25]. The original algorithm application was seen in macular imaging shadow correction and was adapted for vessel imaging in the brain.

Attenuation in an OCT signal is modeled by an exponential decay:

$$s(z) = Kr_s(z)e^{-2\alpha \int_{z_0}^{z} r_s(\omega) d\omega} \qquad \text{Equation 12}$$

where K is a coefficient, where α is the attenuation coefficient and $r_s(z)$ is the reflectivity profile. The exponential decay term $e^{-2\alpha \int_{z_0}^{z} r_s(\omega) d\omega}$ describes attenuation, which causes shadowing in the images and removal of the exponential term is the aim of shadow removal.

As in [25], the attenuated OCT signal is re-written to solve for the unattenuated form. Namely, the desired result is a nondecaying profile $\alpha r_s(z)$. The basis of this analysis is compensation of ultrasound imaging to isolate the local attenuation. The unattenuated profile is determined as:

$$\alpha r_s(z) = \frac{s(z)}{2 \int_z^{\infty} s(\omega) d\omega}$$

The compensated image is calculated and exponentiated to a certain number n. A higher value of the root, n, preserves more details from the original image including the shadows. In circumstances where more removal is desired, a higher n-value should be used. The original image is subtracted with the compensated image, K, and the results are normalized.

To test the algorithm, a value of $n = 0.5$ was used. Then, all pixels that have a value of less than zero are zeroed. Features are further enhanced by setting a clipping limit that will threshold the image, creating an improved contrast between background and feature.

Since structural images and angiograms are logarithmically compressed to show the features by reduction of dynamic range, a cross-sectional slice of a brain scan was used to test the performance of the algorithm, shown in Figure 36. In the image, the original angiogram was compressed to the power of 0.5. Adjusting the *n* parameter affects the amount of features that are removed. When *n* = 0.3, the shadow trails seen in the original image are removed (Figure 36(B)). Features above vessels are visible. When increasing the value of *n*, such as to *n* = 0.8, partial removal is observed where some shadows remain in the image.

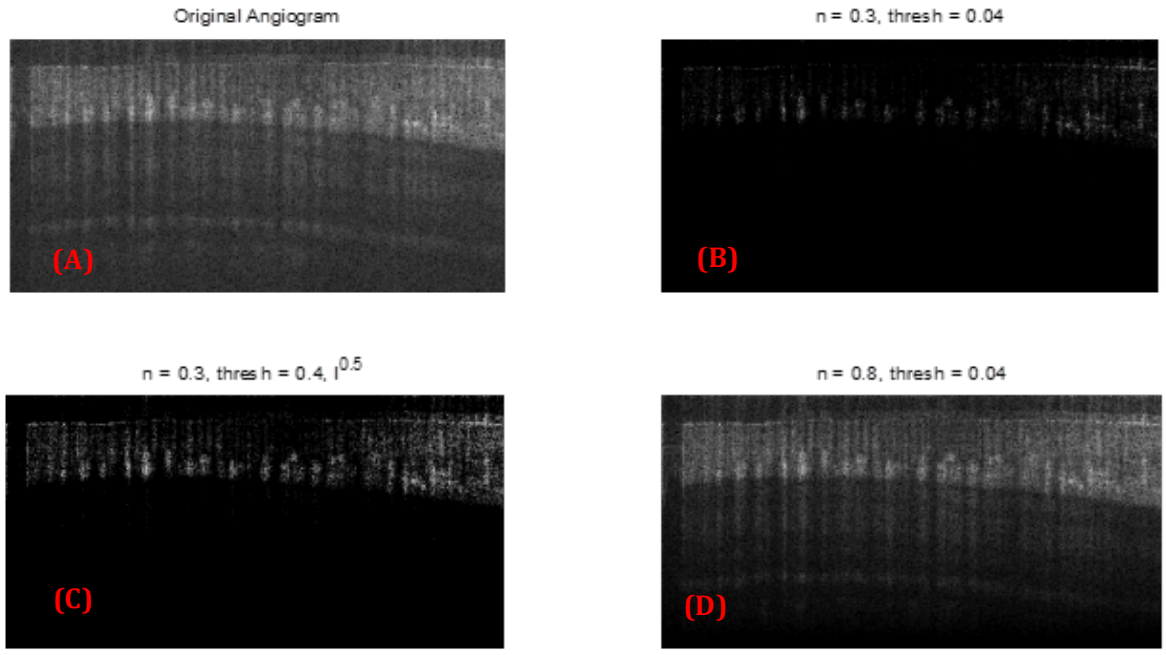

Figure 36 - (A, top left) Original angiogram image (B, top right) Deshadowed with *n* = 0.3 and a clipping limit of 0.04 (C, bottom left) Deshadowed with *n* = 0.03, with the same clipping limit and the final image is taken to the 0.5th power. (D, bottom right) Deshadowed with *n* = 0.8, with minimal deshadowing.

The lateral A-scan from the same point, taken from all four images in Figure 36, is shown in Figure 37 and represents the effects of the algorithm. The blue line represents the original angiogram, with a greater degree of variation in pixel intensities in comparison to the processed images. Line D is similar to the original, where minimal deshadowing peformed. Line C has higher intensities than Line B from exponentiating the final result to the 0.5^{th} power, increasing the intensity and decreasing the dynamic range of the image.

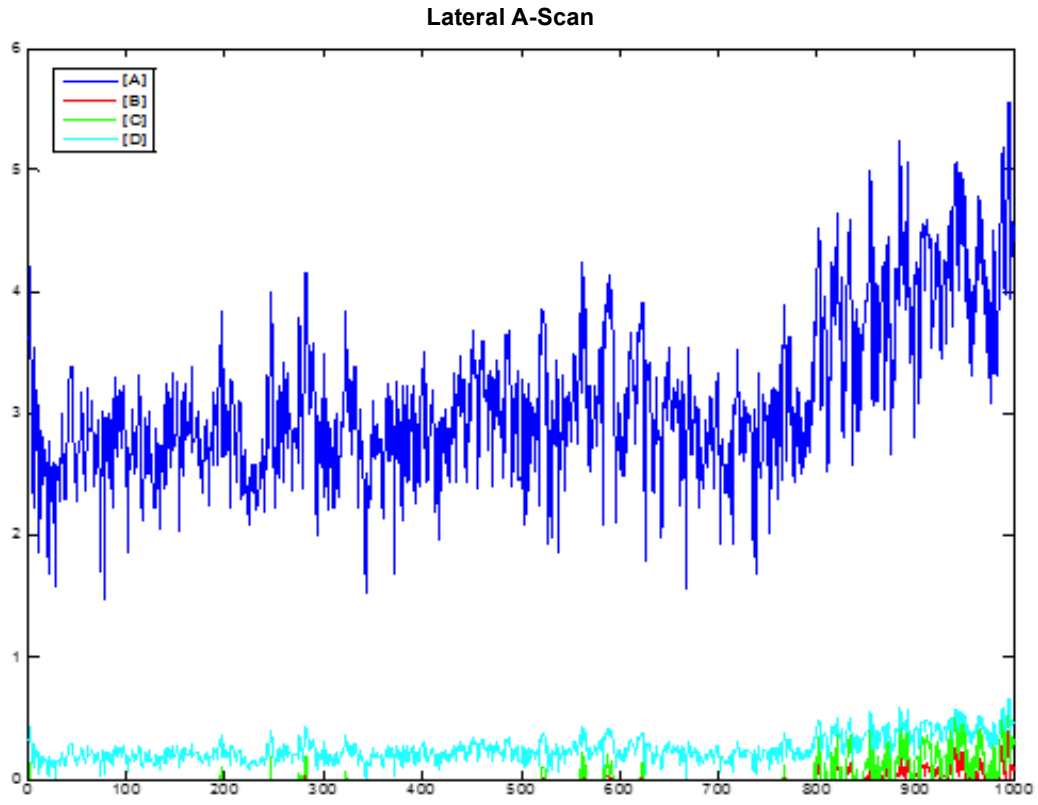

Figure 37 - Corresponding lateral A-scan for images in Fig. 35 from the same location.

Figure 38 is a comparison of the deshadowing of a cross-sectional image with superficial vessels and capillaries of a chicken embryo. The capillaries (indicated by

the red arrows) are preserved in the shadow removal. The vessel contour remains defined, and as the rest of the shadow is cleared, the stripe down pattern that may be a result of RBC orientation. The algorithm preserves pixel intensities that have high intensity and shows a sharp change from the background. Performance is limited for weak signals, where intensity is similar to the intensity of the shadows. In some cases, capillaries were visible, although very faint, but in others, is completely removed.

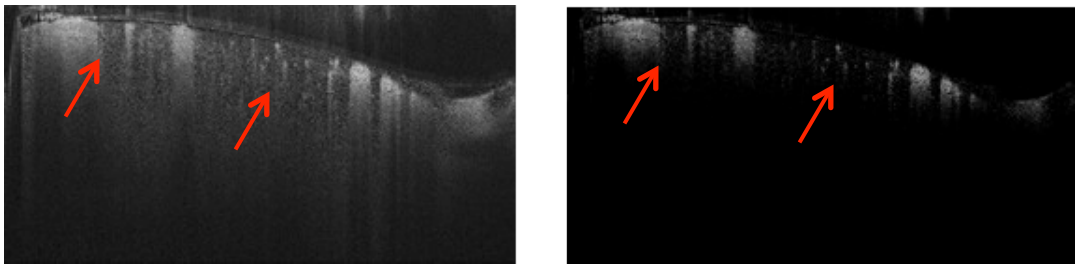

Figure 38 – Comparison of original (left) and deshadowed (right) angiogram.

Figure 39 shows 3D rendering of the original and processed angiograms. Figure 39(A) is the original angiogram, while Figure 39(B) shows the deshadowed angiogram. Some capillary details are lost, as highlighted by the yellow box. However, some regions are also "uncovered" by the algorithm, for example, areas with obstruction by perhaps the dura can be seen more easily and the corresponding vessels are visible, highlighted by the dashed yellow box. Figure 39(C) serves as a comparison when the *n* value is set higher.

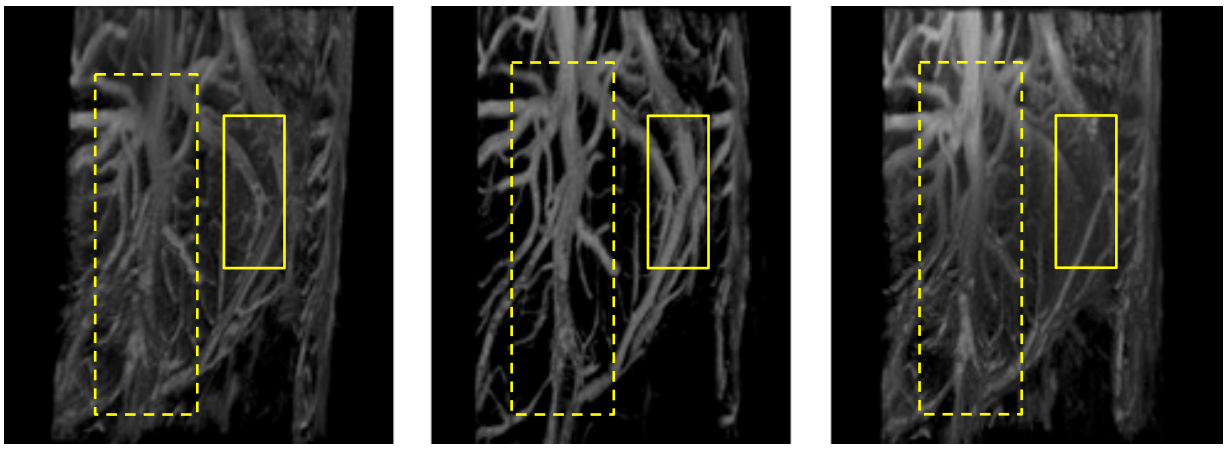

Figure 39 - (A, left) original (B, middle) deshadowed n = 0.28 (C, right) deshadowed n = 0.6, both with thresh = 0.05

5.2 Artifact Removal

Background subtraction was based on the rolling ball algorithm, tested to remove vertical line artifacts due to motion in angiograms. The performance depends on the choice of parameter value *R*, which is the radius of the rolling ball. The implementation of this code involves erosion and dilation of the binary image, and subtraction from the original image.

The results in Figure 40 show the vertical line removal. This is ideal for remaining artifacts that were not removed by the motion compensation, and/or the scanning protocol leading to averaging of several frames at the same position over time. The smaller radius is sensitive to larger structures and will eliminate those before any smaller structure; meanwhile, too large a radius will eliminate too much of the vessel and capillary structures. For this reason, this implementation of the algorithm should be minimized unless necessary; most of the deshadowing

algorithm will likely remove the background noise not accounted for in the compensation.

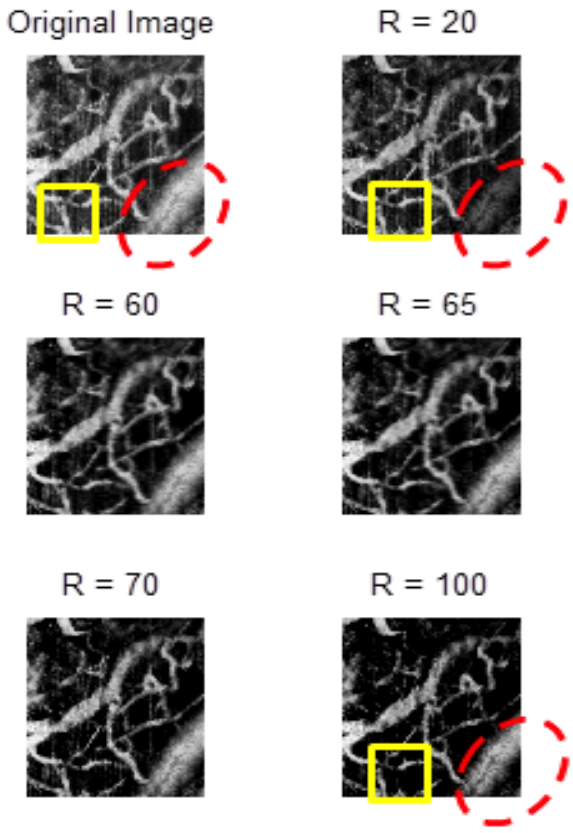

Figure 40 - Comparison of vertical artifact movement correction with varying radius size.

5.3 Depth Color-Coded Maximum Intensity Projection

Maximum intensity projection allows projection of data from the X, Y or Z direction. A color gradient is used, where each color is used to mark a depth position. Each row was assigned a color based on the corresponding colormap, creating an RGB matrix. Each R, G, B layer was individually projected as a 3D dataset, and the projected combinations of the RGB was combined to create the final

depth-encoded intensity projection. Contrast enhancement was applied to improve the image quality, including adjustment of contrast parameters by setting a clipping limit and the distribution of the image, in our case, a Rayleigh distribution.

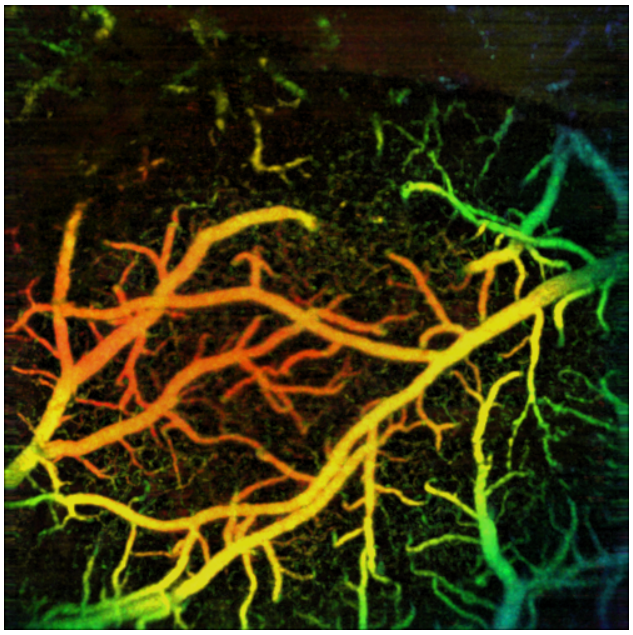

Figure 41 - Depth color-coded maximum intensity projection.

5.4 Velocity and Flow Analysis

The velocity line profile is determined as a 1D line along a vessel in a velocity image. The velocity line profile is useful in determining velocity changes occurring within a vessel, particularly during pre-, intra- and post-stimulus periods. An example of a velocity line profile is marked with a red line on the vessel within the Vessel Map in Figure 42.

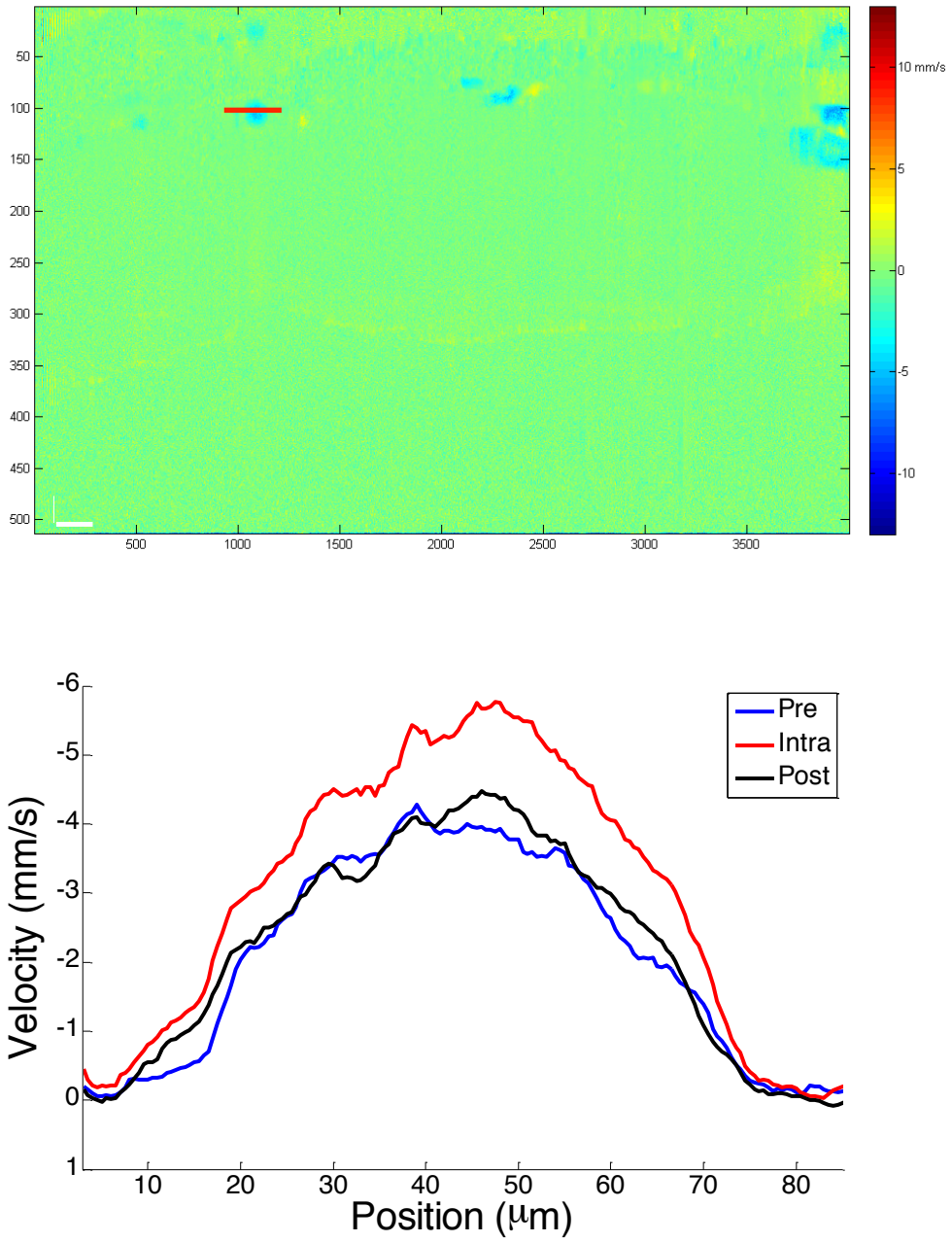

Figure 42 - (Top) Vessel map and (Bottom) velocity line profile of the vessel, indicated by the red line across the vessel.

The velocity line profile in Figure 42 indicates an increase in velocity during stimulation, while the velocity in the vessel before and after stimulation remains the same, with a maximum of -4.278 mm/s and -4.477 mm/s in in pre- and post-

stimulus respectively. Meanwhile, the maximum during stimulation is shown to be -5.773 mm/s.

For velocity analysis, the user is prompted to mark vessels within the image that will be analyzed further. To determine the velocity changes over time, the highest 10% velocities in a vessel are averaged and plotted. The average velocities show the changes occurring during a continuous segment of scanning before, during and after optogenetic stimulation according to the protocol. A sample velocity profile is shown in Figure 44, based on the vessel circled in red in Figure 43. Times when stimulation is turned on and off are marked with a green line. In these line profiles, the laser was turned on after 4 seconds of recording. The region was scanned with a laser on for 10 seconds. The grey lines in the velocity profiles are velocity profiles for each recording. The maroon line is the average of all recordings. In the second plot, all velocities are normalized to the pre-stimulus data, before the laser is turned on for stimulation.

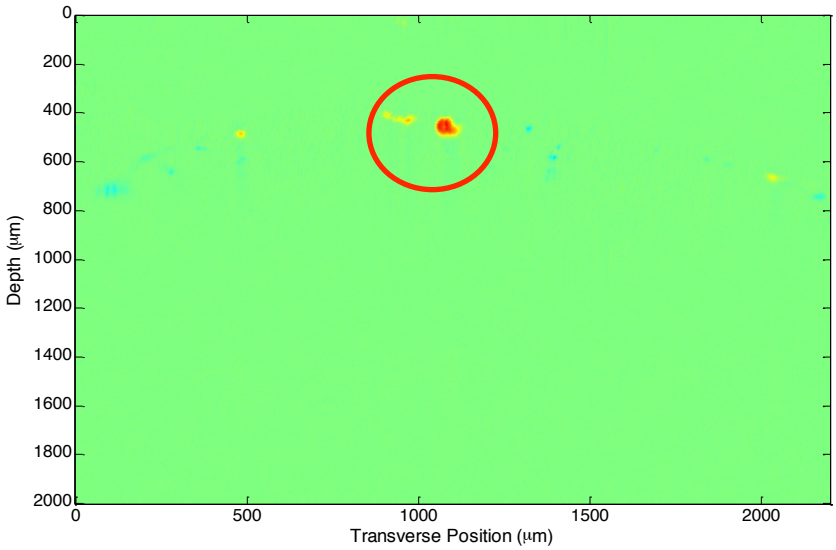

Figure 43 - Vessel map of a mouse brain scan.

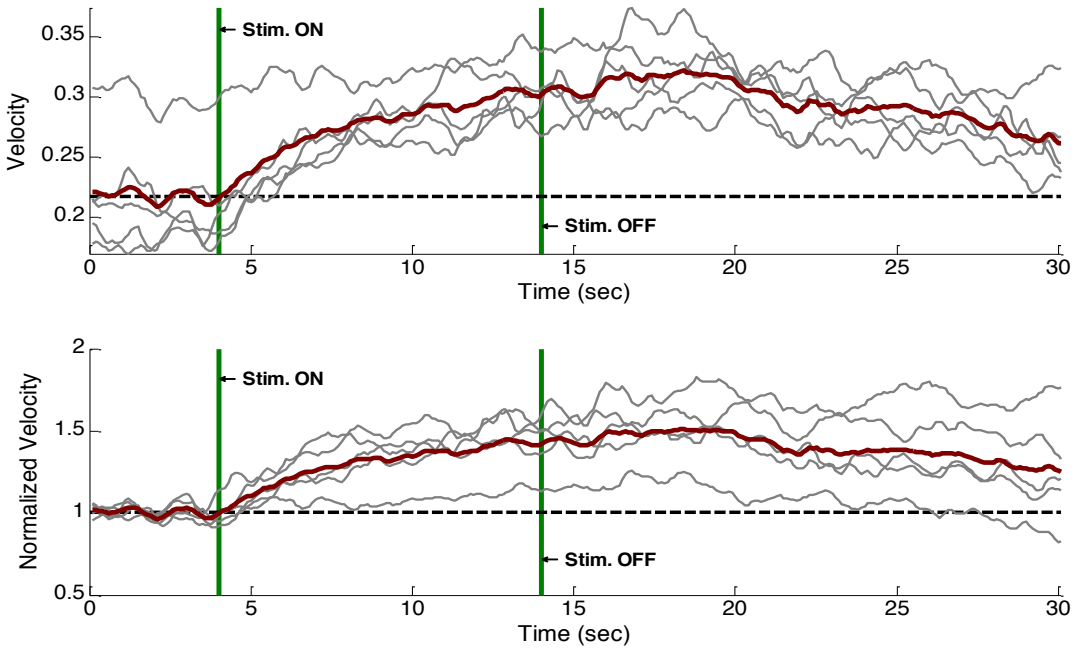

Figure 44 - Velocity line profile for the vessel circled in red.

Flow is defined as the rate of fluid motion across a volume over a period of time. Monitoring flow over time consists of a summation of velocities within a vessel cross-section plotted over time. Flow profiles are represented similarly to the velocity profile shown, with flow and normalized flow profiles for the recordings.

Chapter 6

Experimental Results and Analysis

Chapter 6: Experimental Results and Analysis

6.1 Animal Protocols

With the system, experiments were carried out at the University of Wisconsin-Milwaukee and the University of Wisconsin-Madison, where Sprague Dawley rats and transgenic mice were used respectively. All animal protocols were approved by the Institutional Care and Use Committee (IACUC) at University of Wisconsin-Milwaukee and University of Wisconsin-Madison.

Female Sprague Dawley rats (Charles River, USA) were obtained at around 250 grams and allowed food and water ad libitum. At least four weeks prior to the OCT experiments, the rats were injected with a virus that carries ChR2 vector. At the time of the OCT experiment, the rat was anesthetized with isoflurane and placed in the stereotaxic frame. The scalp was opened and the skull was exposed, and a dremel was used to perform a 3mm by 3mm craniotomy over the site of the injection. The dura was left intact. The OCT device was positioned over the animal for scanning. Throughout the entire procedure, the rat was kept under isoflurane anesthesia.

Transgenic Thy1::ChR2/H134R mice were bred at the University of Wisconsin-Madison. The H134R variant of ChR2 has slower off-kinetics and as a result provides more light sensitivity which is required for these experiments. The mice were approximately 25 grams. At the time of experiment, the mouse was anesthetized with ketamine and placed secured with metal plates. The scalp was opened and a craniotomy was performed over the selected regions of the brain. The

dura was left intact and the surface of the brain was kept moist with periodic administration of saline solution over the surface.

In both sets of animal experiments, the surface of the brain was illuminated with blue light (470 nm) for ChR2 stimulation.

6.2 OCT Scanning Protocols

The OCT scanning protocol used is determined based on the processing method. Angiography is used for imaging vasculature networks, while Doppler OCT imaging is used for detection of hemodynamic signals in vessels.

Angiography is performed for three-dimensional volumetric data sets. Since angiography is predominantly a qualitative imaging technique, three-dimensional protocols were used to image a cortical patch. A bi-directional scanning pattern was used and varied with acquisition of 1 frame or 10 frames of B-scans per position. Each B-scan consisted of either 500 or 750 A-lines. The user may define the total number of B-scans acquired. Increasing the A-line density would often result in artifacts for angiography.

For two-dimensional Doppler imaging, a higher density of A-lines per B-scan is desirable to improve the minimum resolvable velocity. Each frame may consist 2,000 to 4,000 A-lines, where the higher sampling density is desirable for velocity estimation. The A-lines are usually captured at a rate between 20,000 to 60,000 A-lines per second. The number of frames captured is 25-50 frames to ensure sufficient number of frames for speckle reduction. For three-dimensional Doppler imaging, 1,000 A-lines are captured for a select number of frames up to 10.

Higher frame density increases post-processing computation load proportionally. In Doppler imaging, the scanning head is positioned at an angle, unless an alternate scanning head limits this tilt.

Detecting hemodynamic signal changes consists of data acquisition with and without optogenetic stimulation in three scan periods: pre-stimulus, intra-stimulus and post-stimulus. The total scanning time for each scan in all modes is 30 seconds. During pre-stimulus, the arc lamp is turned off and the cortex is imaged for 4 seconds. The arc lamp is turned on during intra-stimulus and the surface is exposed to illumination for 2 or 5 seconds. The lamp is turned off in post-stimulus and the cortex is imaged for either 24 or 16 seconds, depending on the intra-stimulus time to total 30 seconds. Longer scanning times for post-stimulus aims to ensure the effects of stimulation are not being recorded. Figure 45 shows the typical set up of the Doppler scanning protocol with optogenetic stimulation. The scanning head is titled at a Doppler angle to detected velocity.

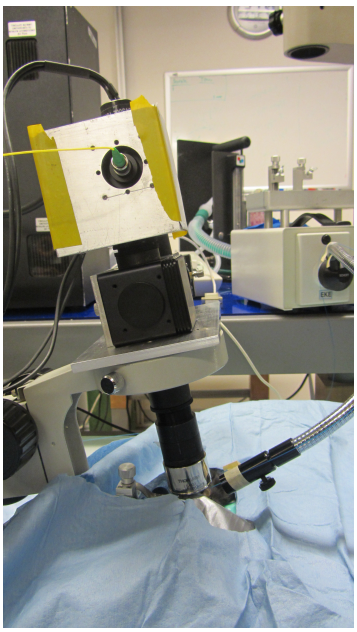

Figure 45 - OCT scan head titlted at an angle for Doppler scanning.

6.3 Optogenetic Experiments with a Rat

Early optogenetic-OCT experiments were performed on a rat. Three-dimensional angiography was performed over a cortical patch. In the earlier scan protocols, pre-stimulus was recorded for 3 seconds, intra-stimulus between 3 to 10 seconds, and post-stimulus for 10 seconds. A bright-field image recorded using the CMOS camera, was used for comparison with the OCT angiogram, shown in Figure 46 and Figure 47**,** respectively. A craniotomy was performed on the rat according to the approved protocol guidelines. For this image, 750 A-lines were scanned at a rate of 40,000 A-lines per second. A scan angle of 2 provides a 2mm x 2mm views of the cranial region. For each B-scan, 10 frames were recorded. Comparing the images, the main vessel, labeled “A” is visible in both images. However, capillary beds not visible in the bright-field image are distinctly visible in the angiogram. The OCT depth of field demonstrates increased uniformity when compared to the bright-field

image that begins to diminish focus radially outwards. One structural cross-sectional image is shown alongside the 3D angiogram projection. The structural images are the basis of determining the angiograms.

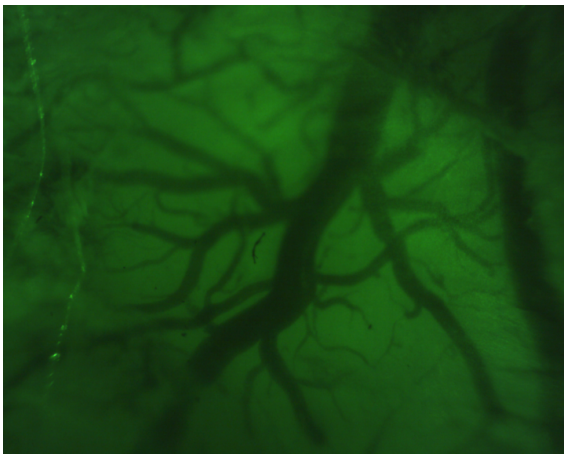

Figure 46 - Bright-field image of the 2 x 2 mm cranial region.

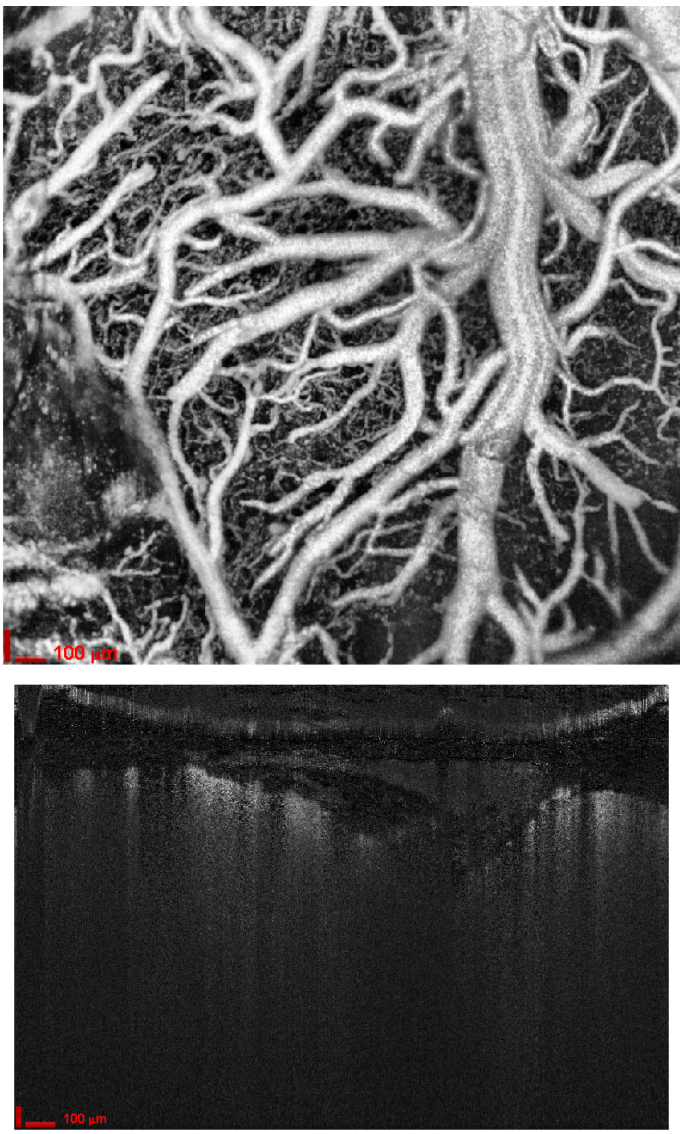

Figure 47 – (Top) 3D angiogram of the rodent brain surface (Bottom) Cross-sectional OCT image of the cortical surface.

6.3.1 Doppler OCT and Angiography Imaging with Optogenetics

In hemodynamic signal quantification between pre-stimulus, intra-stimulus and post-stimulus, several changes are desired for detection: differences in vessel diameter, velocity changes in the vessel, and the depth of the detected vessel or

capillary. The detected hemodynamic changes in a rat are reported with optogenetic stimulation. The detected vessels are shown in the vessel map in Figure 48.

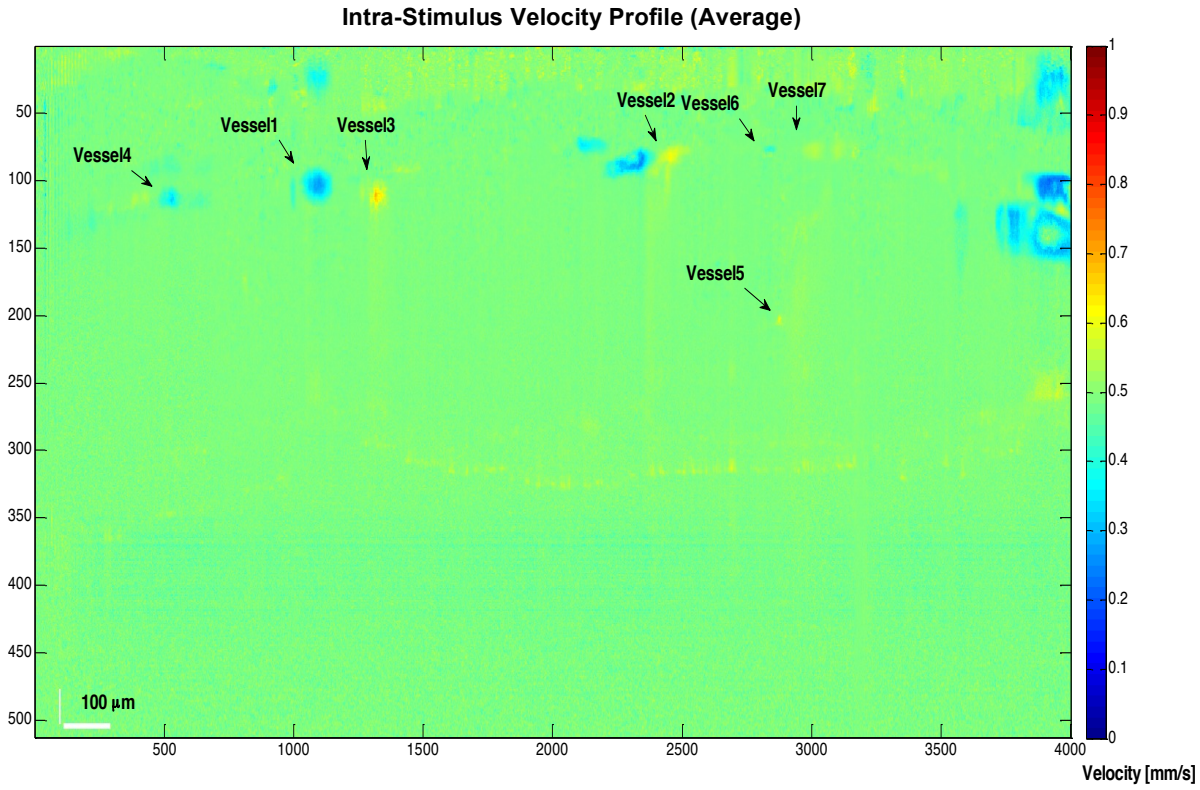

Figure 48 - Vessel map of Doppler image.

Velocity line profiles are compared for pre-stimulus, intra-stimulus and post-stimulus. The velocity line profile is taken from a selected central point along the vessel. Before comparison, the velocity images for the three cases are registered and aligned to compensate for animal motion.

In all three profiles from experimental results, shown in Figure 49, a laminar flow profile that can be described by a parabolic equation is demonstrated in all three cases of blood flow in the highlighted vessel. In both pre-stimulus (blue line) and post-stimulus (black line) cases, maximum velocity is approximately -4 mm/s.

Meanwhile, intra-stimulus (red line) has a maximum velocity of -6 mm/s. This signal is indicative of the change induced through optogenetic stimulation, where activity is induced by stimulating when ChR2 proteins. The size of the vessel is determined as the FWHM. At its smallest, the vessel size is approximately 35 μm, and during optogenetic stimulation increases to about 45 μm.

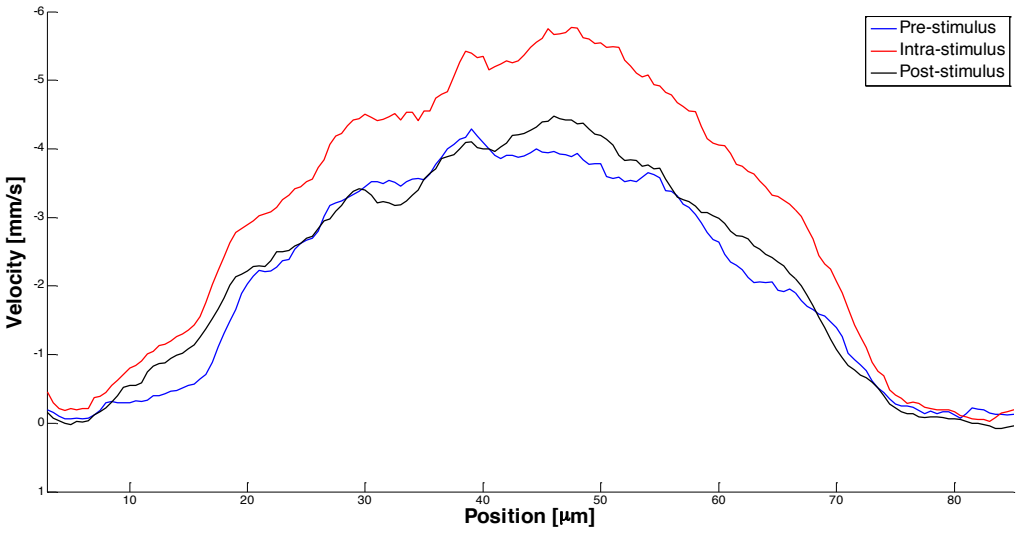

Figure 49 - Velocity line profile for Vessel 1.

Another vessel within the network is observed, highlighted in Figure 50**.** The detected capillary is 10 μm in diameter. Similar to the previously highlighted vessel, a maximum velocity of 2.5 mm/s is detected during optogenetic stimulation. The sign of the line profile indicates its motion in an opposing direction to the vessel seen earlier. The post-stimulus line profile indicates a drop in velocity magnitude, going from 2.5 mm/s to 1.7 mm/s.

Combining the three-dimensional data sets from Doppler imaging and angiography provides a visual representation of velocity. The ability to quantify

velocity volumetrically is limited by the Doppler angle. Since the direction of flow is unknown, flow perpendicular to the incident beam will not be detected. In this instance, combining angiograms and volumetric Doppler image provides a meaningful visual towards understanding blood flow in the vasculature network of the brain. Figure 51 shows the angiogram, velocity image and the superposition of the two images. Without the angiogram, velocity flow is difficult to distinguish. Overlaying the two provides contextual information into the velocity activity. For determining velocity values, a line profile at a desired point can be found to pin point velocity at a certain region.

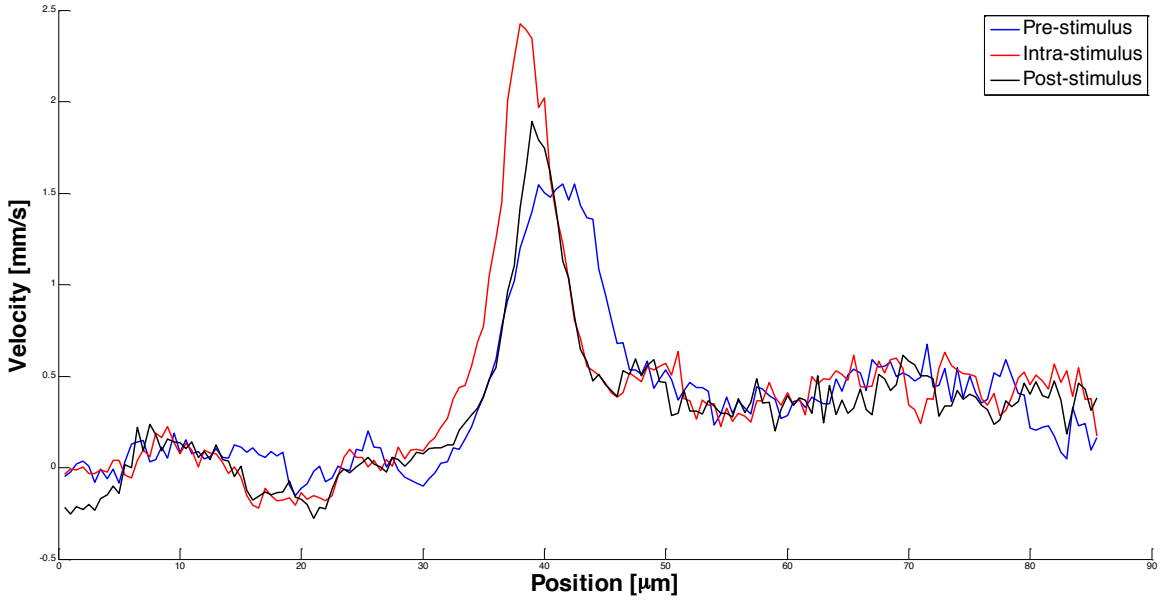

Figure 50 - Velocity line profile of Vessel 5.

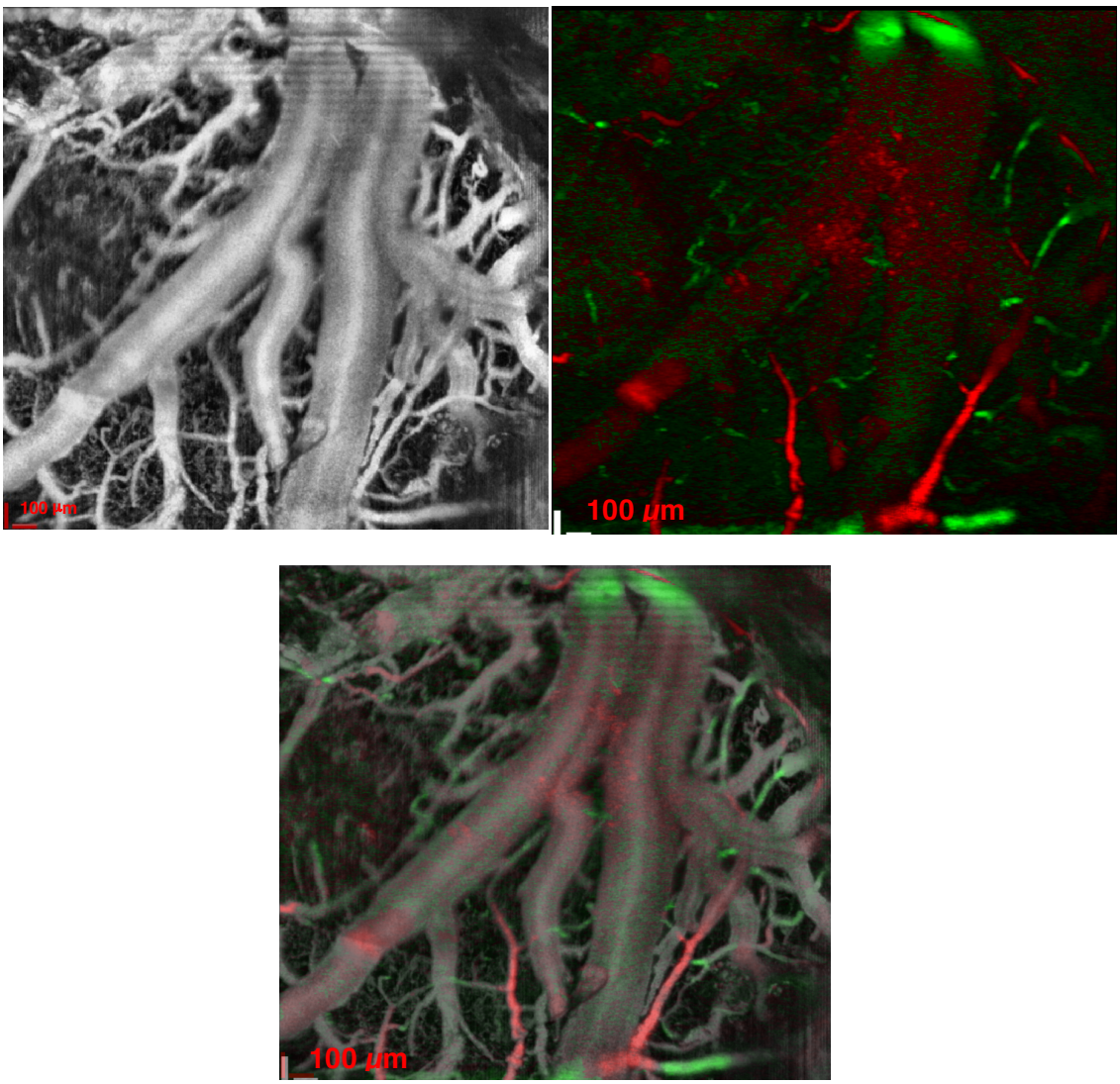

Figure 51 - Angiogram, Doppler velocity image and overlaid image of the two.

6.4 Transgenic Mouse Results

The transgenic mice experiments were performed according to animal facility protocols at the University of Wisconsin-Madison. A stereo-microscope was used in place of the six-axis boom stand head typically used in the system. This resulted in mounting the scanning optics base plate on the appropriate microscope. Since the microscope head is rigid, a Doppler angle could not be set and vessels longitudinal to the scan head was detected. A 473 nm laser was used for stimulation.

Vessel dilation was verified using bright-field image observations, shown in Figure 52. In particular, the middle cerebral artery (MCA) was found by inspection. The MCA is a branch of one of the two major blood suppliers of the brain. The internal carotid arteries supply cortical and subcortical regions.

Dilation is observed in the vein after stimulation, as shown with the blue arrows. There is an observable increase in contrast in the vein, indicating an increase of blood flow, possibly contributing to the darkening of the vein. The OCT field of view is shown in the black box, where regions of the dilating vein and the MCA are captured. In addition, a fluorescent image is captured using the CMOS camera which is installed on the OCT scanning path.

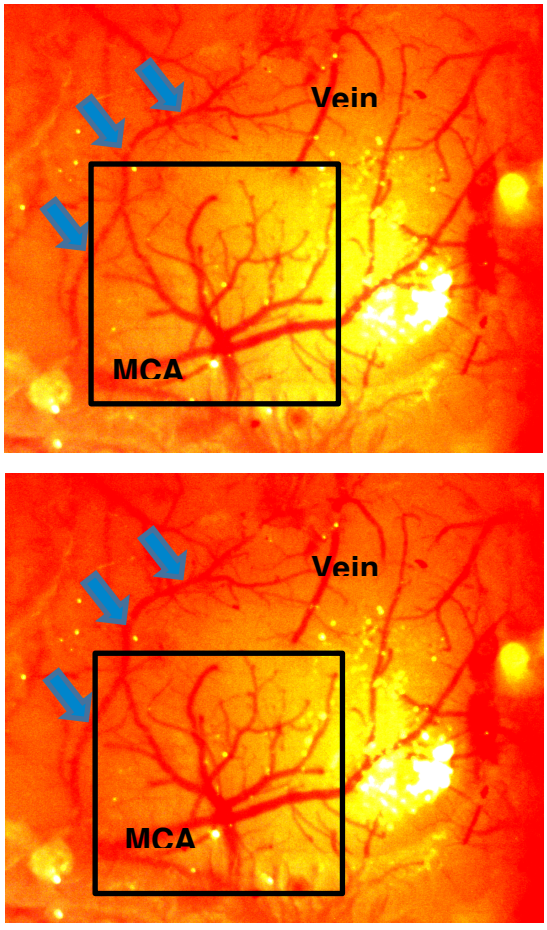

Figure 52 – Bright-field observations for (Left) pre-stimulus and (Right) intra-stimulus.

A selection of angiograms, which identify moving RBCs, of a transgenic mouse scan are shown in Figure 53, along with a 3D rendering of the volumetric angiogram data set done on ImageJ software [26]. Comparing the OCT image with the bright-field image, the MCA is identifiable on both images, however, the OCT image captures a higher number of capillaries and veins.

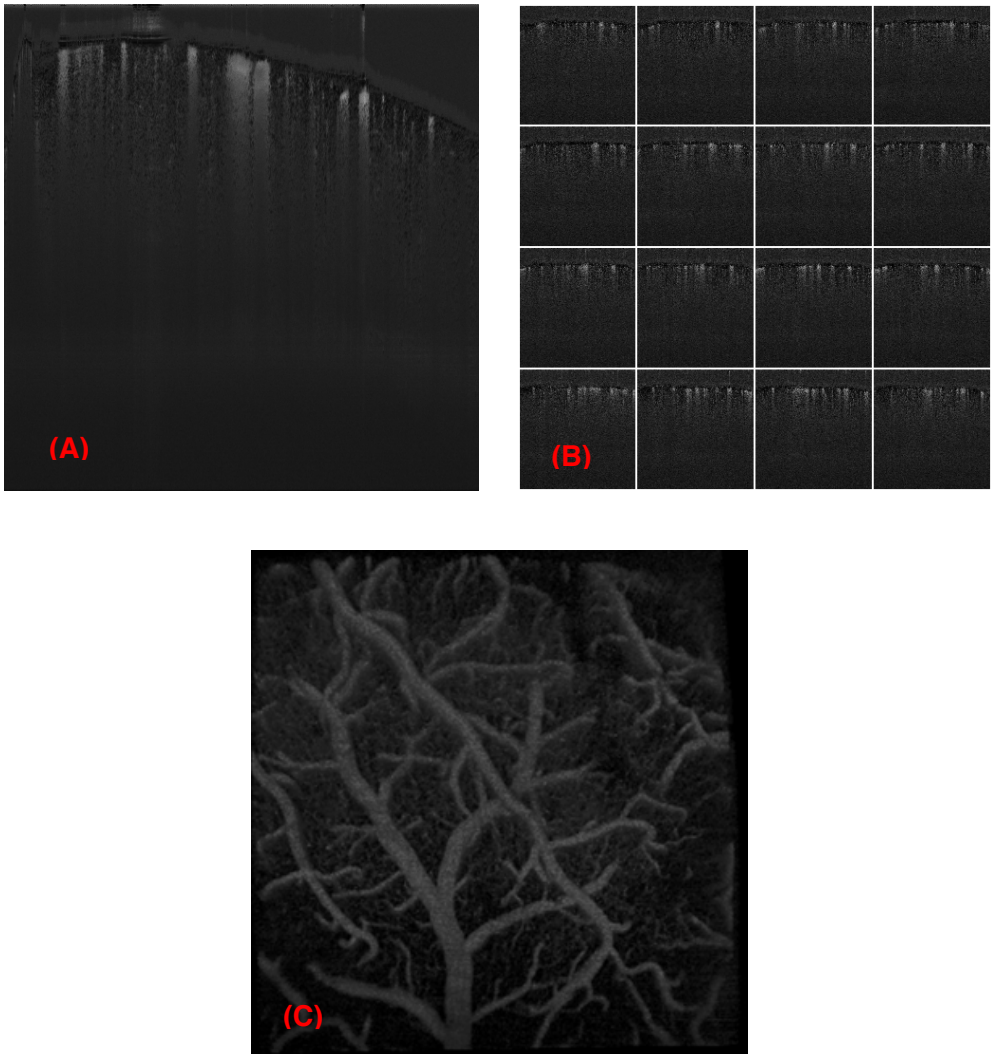

Figure 53- The sequential process of generating angiograms, (A) A cross-sectional angiogram (B) A set of angiograms (C) Volumetric rendering of the set of angiograms.

To determine the blood velocity changes inside a vessel, multiple 2D scans taken from the same position were recorded and processed. The 2D scan was taken along the path indicated by the red line in the microscope image of Figure 54, with the average velocity image shown alongside it.

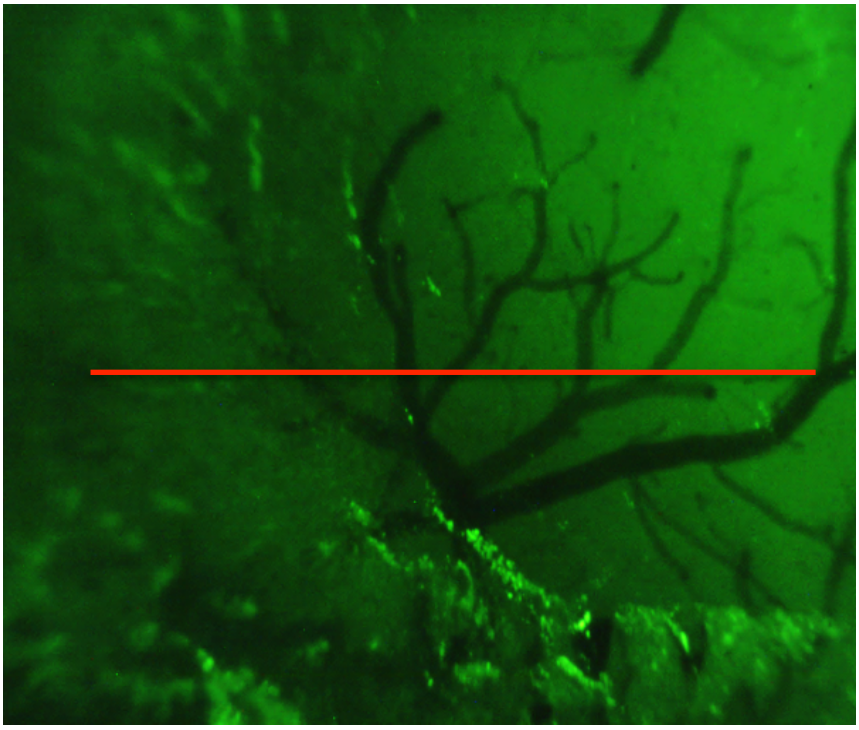

Figure 54 - Sample of a 2D scan path, indicated by the red line, for Doppler imaging.

6.4.1 Mouse 1 Results

Data was acquired for a transgenic mouse, labeled Mouse 1. Prior to angiography and Doppler scanning, dilation was verified by inspection before and during optogenetic stimulation in the bright-field image, shown in Figure 52.

A volumetric data set was acquired for angiograms, and a maximum intensity projection was determined along the depth, or the z-stack, between the ranges of 100-300 μm. The MCA and vein were identified and labeled accordingly in the

angiogram. In the optogenetic experiment, changes in the neighboring vasculature of the MCA and vein were detected in the angiogram projection. The observed changes identified during pre- and intra-stimulus were circled in red for four sites. Changes were observed during stimulus, where neighboring vessels had observable blood flow.

A 3D Doppler scan was also performed around the region. A maximum intensity projection along the z-stack was also performed for the Doppler image. Changes were identified in three sections of the Doppler intensity projection after optogenetic stimulation, though these are not the same sections of the angiogram. In the velocity images, an increase in blood flow is signified by the increase in intensity. Since the microscope head used for acquisition could not be adjusted, a Doppler angle could not be set for velocity measurements, this combination of empirical challenges limit our capability in quantification of velocity profiles. The velocity changes in the angiogram could not be detected in the Doppler images. This suggests the vessels may be perpendicular to the scan head, which would render them unidentifiable without a Doppler angle, which is a limitation of the velocity detection capability.

An overlay of the angiogram and velocity image shows the functional capability of neural activity detection during optogenetic stimulation. The bright-field image is shown to provide a comparison. The OCT images show high-resolution details and

have a higher vasculature density that is captured.

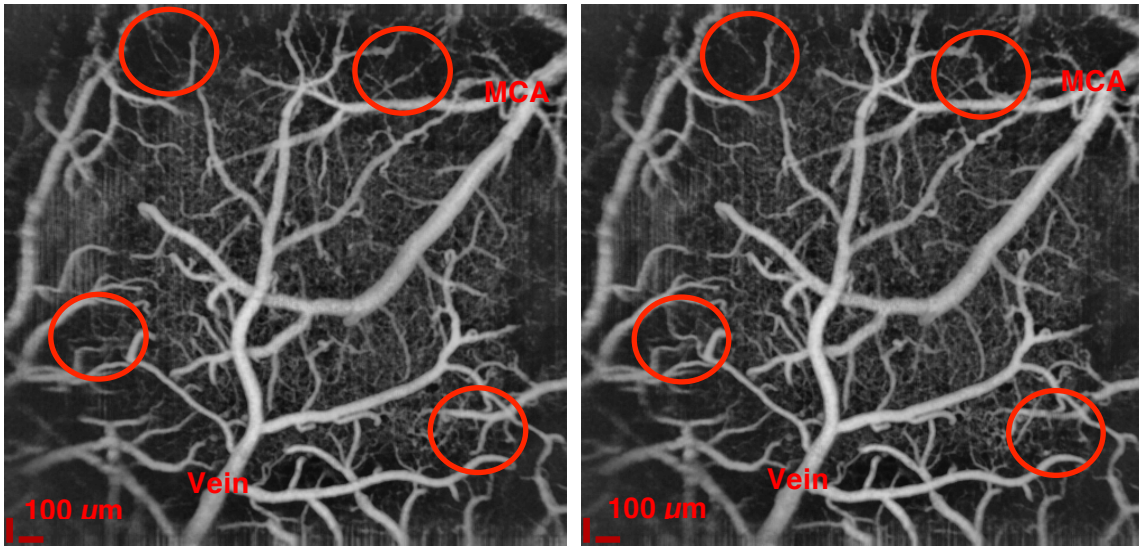

Figure 55 - 3D angiogram projection (left) pre-stimulus and (right) post-stimulus.

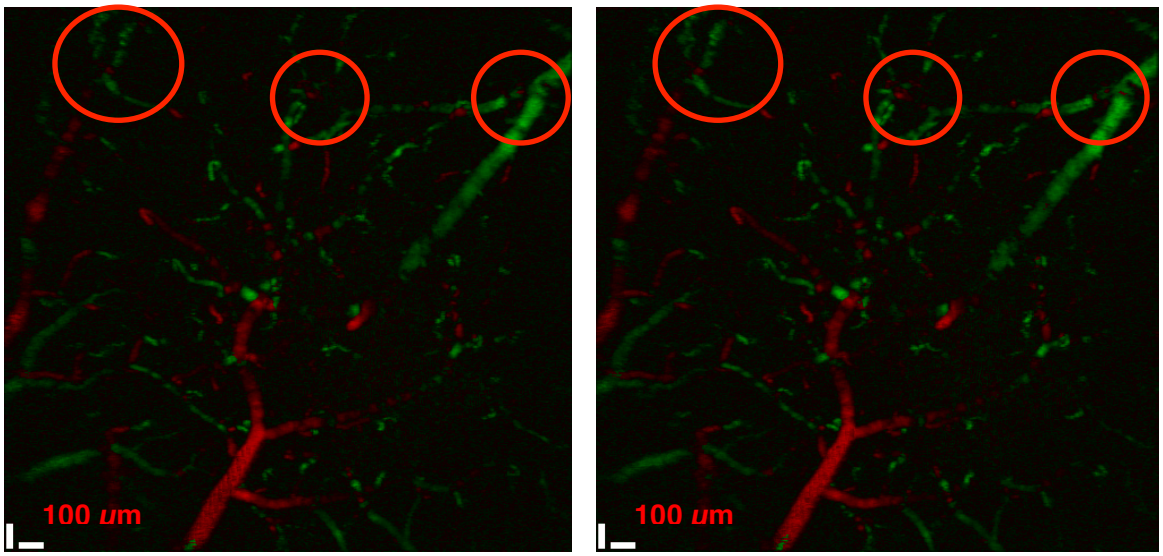

Figure 56 - 3D blood flow projection (left) pre-stimulus and (right) post-stimulus.

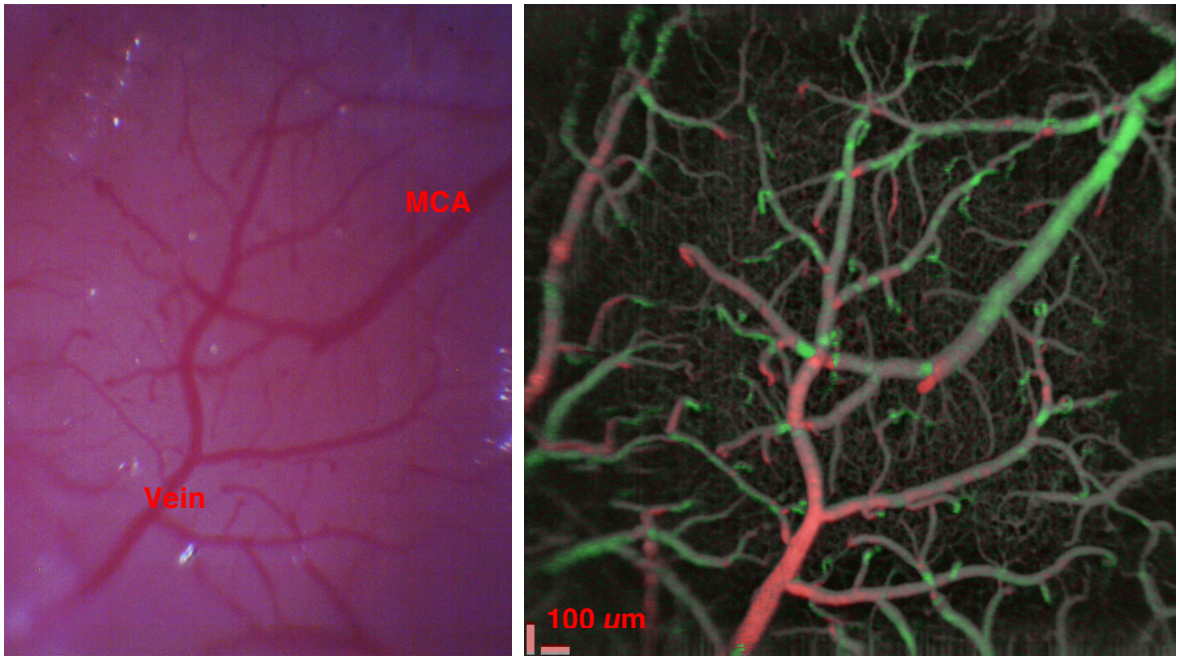

Figure 57 - (Left) Bright-field image and (Right) overlaid OCT and velocity image.

6.4.2 Mouse 4 Results

The scanning procedure was repeated over the same cortical patch, shown in Figure 58 for a transgenic mouse. A series of maximum intensity projections for Recording 2 and 3 during pre-, intra- and post-stimulus is shown in Figure 59. The angiograms highlight observed vessel dilation in red. The diameter changes in both recordings between pre-stimulus and post-stimulus are identical, with the diameter increase and decrease in surrounding vessels of the region. The capillary beds decrease in intensity during stimulation.

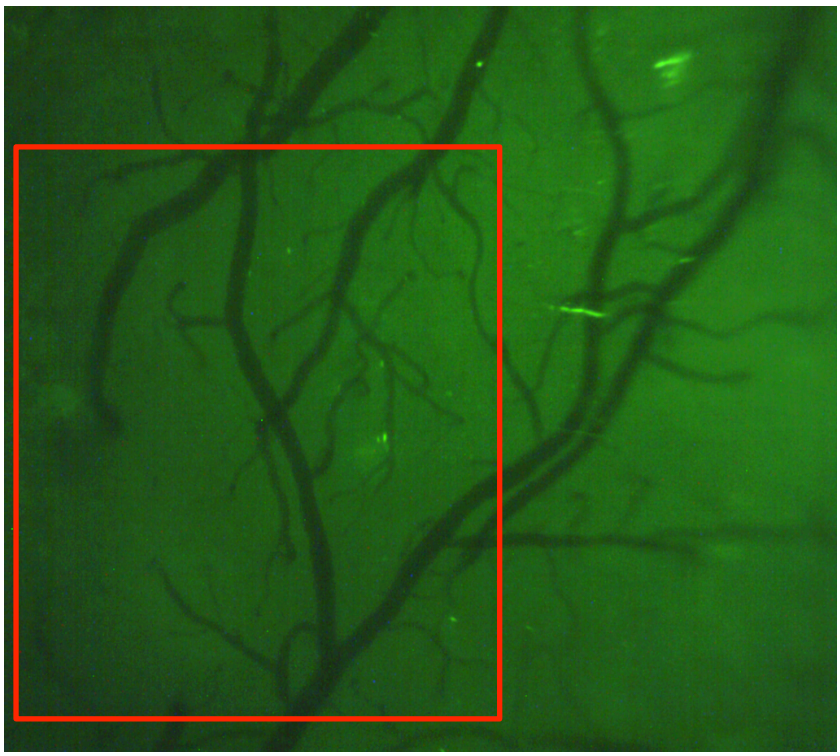

Figure 58 - Microscope image of the cortical patch. The red box indicates the 2 mm x 2mm OCT field of view.

Also shown are the angiograms and Doppler-angiogram overlays from the recording, highlighting the detected vessel changes. In the velocity images, positive velocity (red) describes RBCs moving towards the laser. Conversely, negative velocity (green) denotes RBCs moving away from the laser. Velocity at points highlighted with the red arrow in Figure 60 demonstrates the changes in blood velocity. For the main MCA branch, intra-stimulation velocity drops to 2.77 mm/s. The pre- and post-stimulus velocities are consistent with each other at 2.84 and 2.85 mm/s respectively. The velocity at the top-left position indicated by the arrow follows this pattern, with 0.771 mm/s, 1.02 mm/s and 0.517 mm/s for pre-, intra- and post-stimulus.

The vessel diameter change ratio was calculated for intra-stimulus and post-stimulus with respect to the pre-stimulus diameter. The MCA divides into two branches, labeled branch 1 and branch 2. The sections center is marked with a red line along the section. Generally, the results from three recordings show an increase in the average thickness during stimulation in comparison with post-stimulus thickness. An 8% diameter change was observed in the main MCA branch identified in the image. Branch 1 had more than 10% change, while Branch 2 demonstrated an 8% change. The main changes were occurring in branch 1. Figure 62 and Figure 63 counts the changes in the diameter according to the lines labeled at the central region of the vessel for branch 1 and branch 2, respectively.

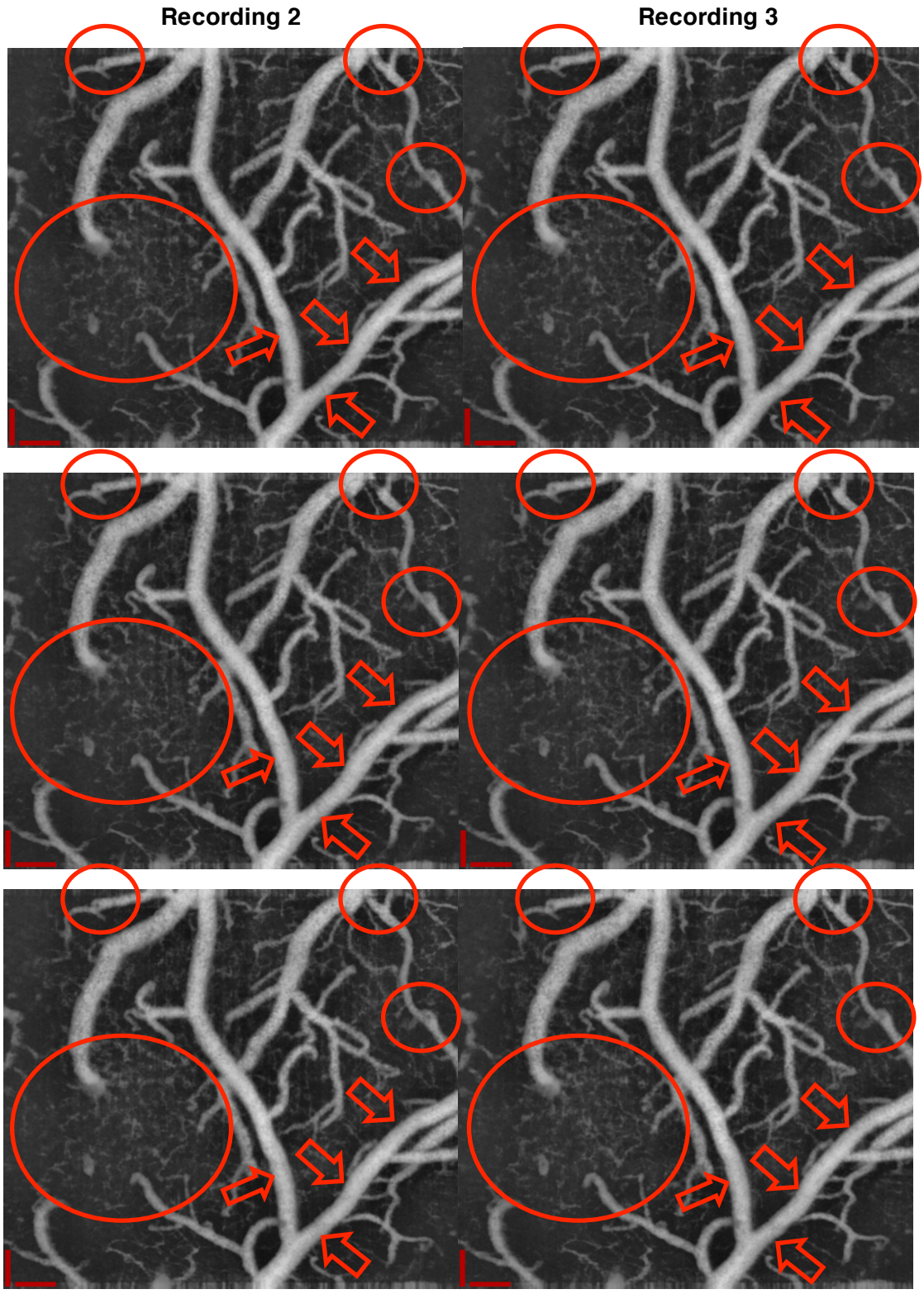

Figure 59 - Comparison of Recording 2 and 3 of pre-, intra- and post-stimulus data.

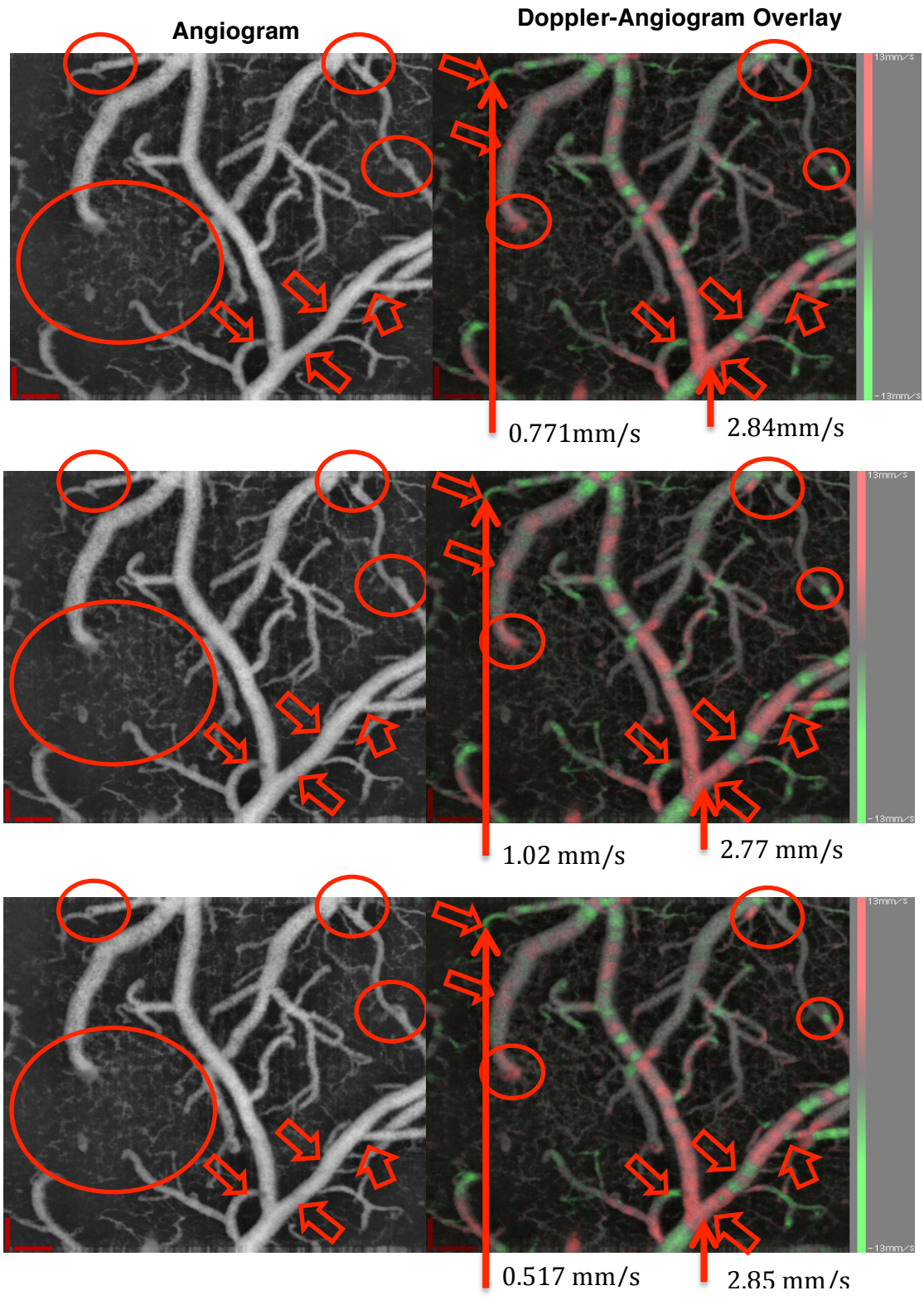

Figure 60 - Angiogram and Doppler-angiogram overlay for pre-, intra- and post-stimulus.

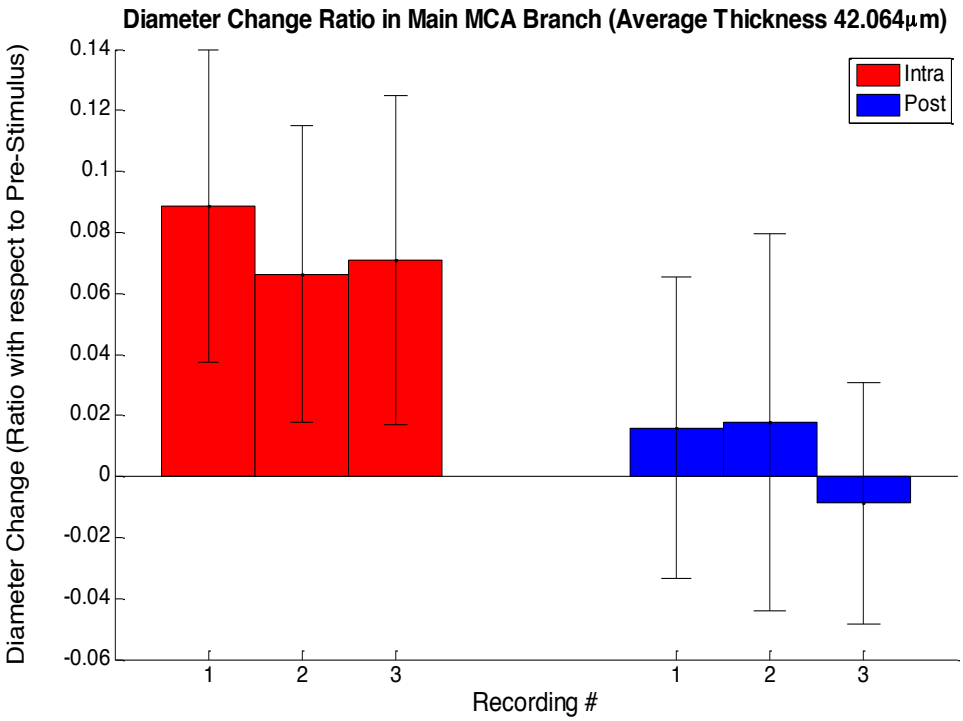

Figure 61 - Diameter change ratio in the main MCA

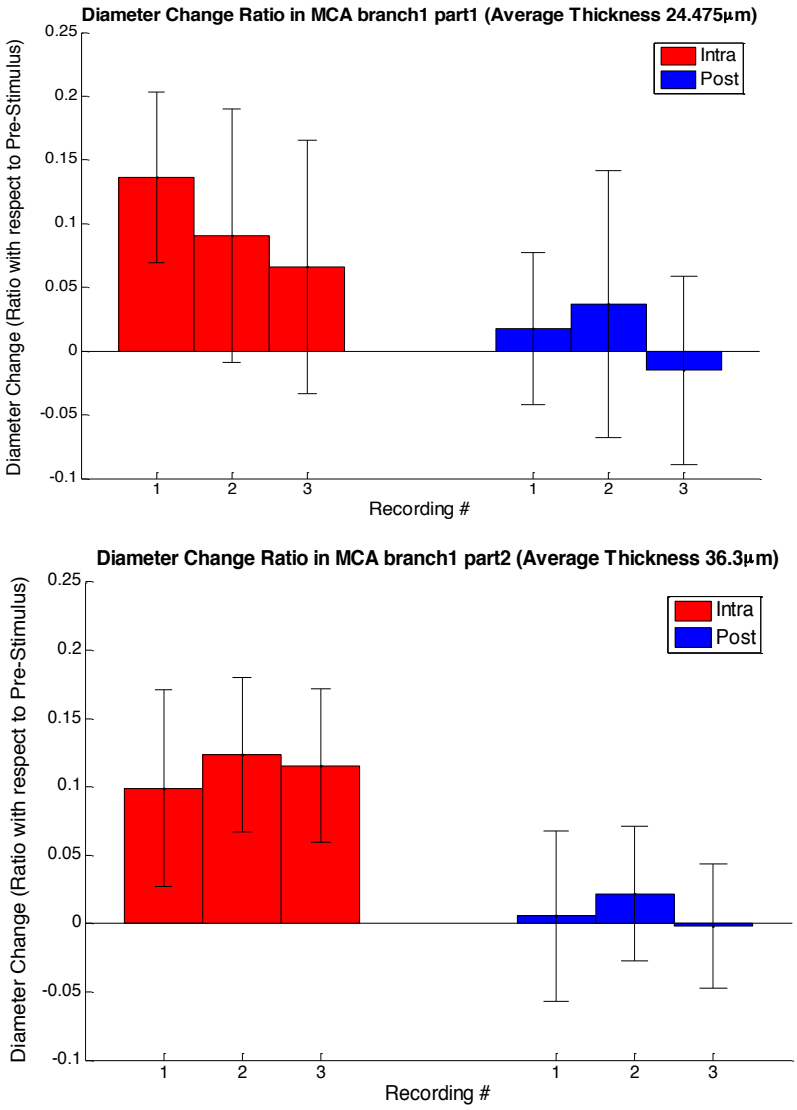

Figure 62 - Diameter changes in branch 1 of MCA.

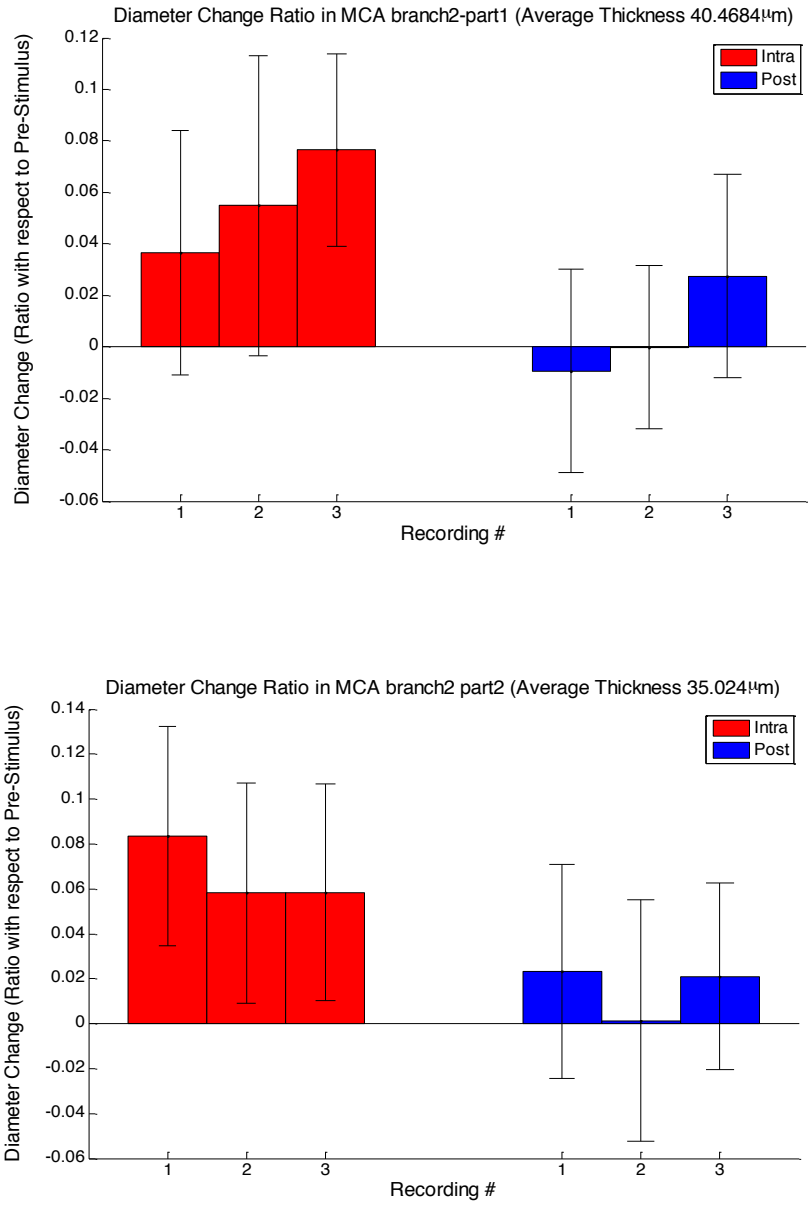

Figure 63 - Diameter changes in the MCA branch 2.

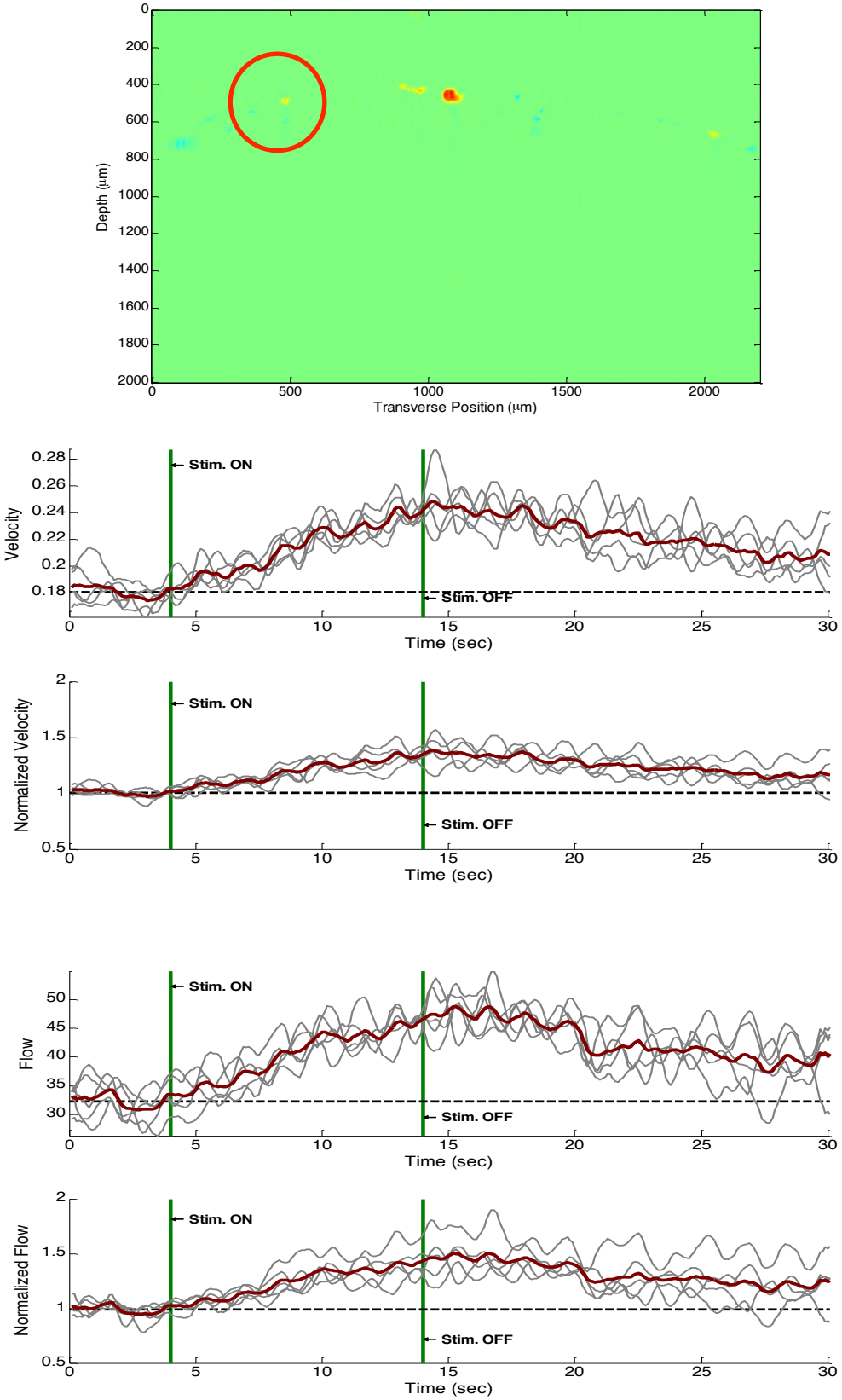

Figure 64 - Changes in flow and velocity for the vessel circled in red on the vessel map.

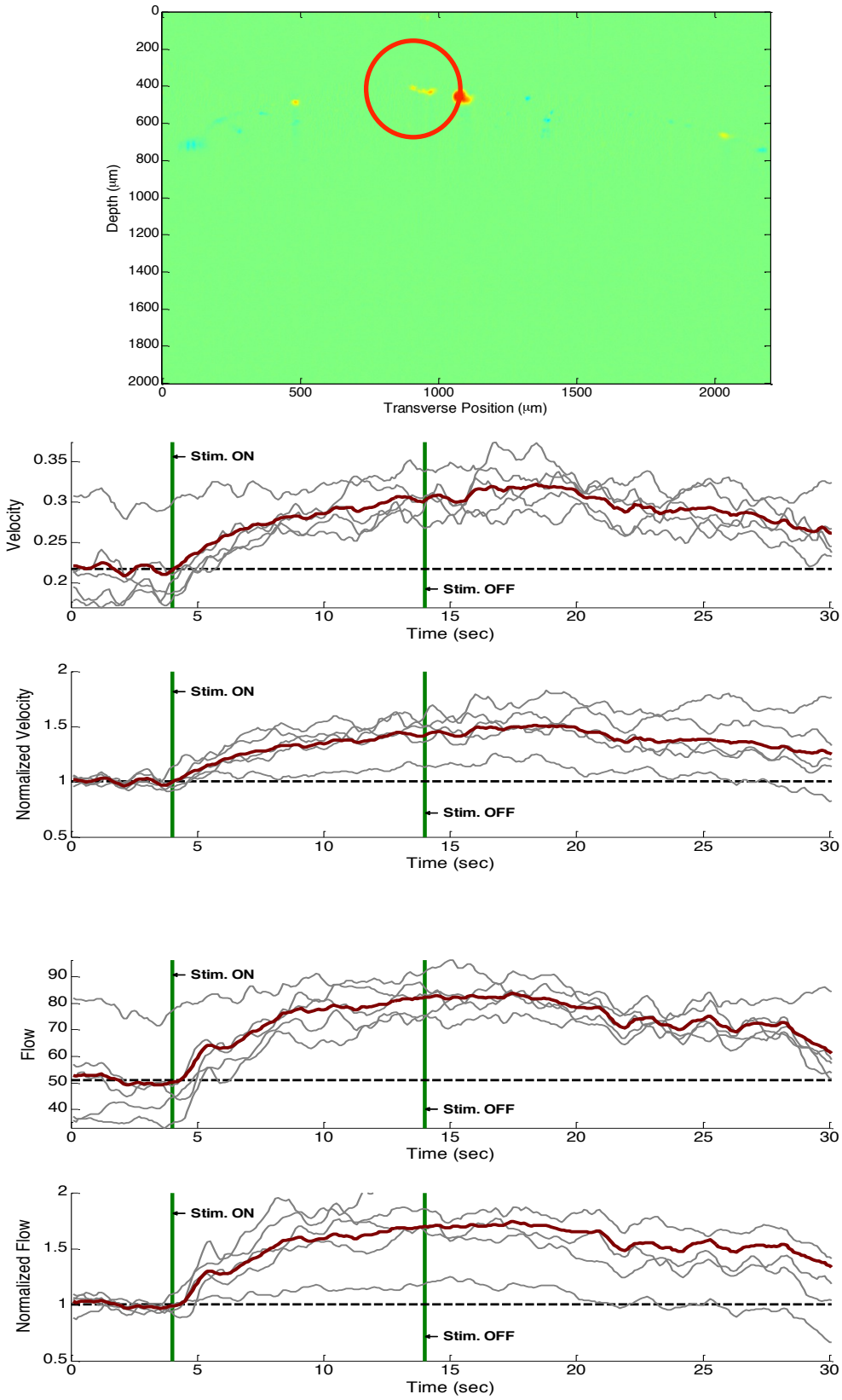

Figure 65 - Changes in flow and velocity for the vessel circled in red on the vessel map.

Chapter 7

Future Work and Conclusion

Chapter 7: Future Work and Conclusion

A spectral-domain OCT system was designed to obtain the ability to quantify changes in the hemodynamic signals and perform angiography in vasculature networks in the brain to study the effect of optogenetic stimulation on hemodynamic signals mostly in the cortical circuitries in rodents. The developed system produces angiograms through imaging of moving scatterers to create contrast for imaging of vasculature networks in the brain. The system can also produce Doppler images as a functional tool to provide quantitative information of blood flow changes. The system utility has been demonstrated for in surgery settings to non-invasively image regions of a rat and mouse brains when stimulated with optogenetics. Experiments were performed in both virally transfected rats and transgenic mice, in which excitatory neuron can be stimulated by exposing the tissue to blue light. The maximum scanning rate of the system is 80,000 A-lines per second with a maximum imaging field of view of 3 mm x 3 mm. The axial resolution is between 4 – 5 μm, depending on the sample, and lateral resolution is approximately 6 μm.

The presented results showed preliminary data from our recent experiments. Initial results presented verified the system functionality in small rodents. Furthermore, the velocity line profile verifies an amplitude change with its laminar flow profile. In comparison to microscope images, the OCT system images cortical regions with higher resolution, and resolves micrometer capillaries. To reach more conclusive results, the experiments must be repeated on both transgenic and control (Wild-type) mice. This part of the study is currently in progress, along with

our collaborators at the University of Wisconsin-Madison. The optogenetic OCT experiments scheduled are set for at least 3 control mice and 3 transgenic mice.

7.1 Craniotomy vs. Thin Skull Experiment Protocol

The current experimental protocol uses a craniotomy for scanning. However, the craniotomy presents a problem with motion within the brain due to swelling. These micromotions reduce the system resolution, as a result, small capillaries are less visible in developed images. Detecting capillaries deeper in the cortex will be challenging when the inherent signal loss is coupled with signal reduction due to motion. Bleeding around the cortical region occurs periodically with a craniotomy, and is especially problematic for OCT scanning due to absorption of the infrared signal by blood. Finally, exposing the brain requires periodic administration of saline re-hydration around the cortical region.

To address this problem, the use of a thin skull instead of craniotomy is being explored. The thin skull procedure reduces the skull thickness to approximately 40 – 50 μm. However, initial results from this procedure have been promising. The thin skull offers a reduction in motion in addition to minimizing of signal-reducing bleeding in the cortical region. However, blue light for optogenetic stimulation cannot penetrate bone as well as the infrared light, and needs to be further studied. Furthermore, a study on the repeatability of results in both transgenic and control mice is necessary. Our results shown earlier have demonstrated repeatability in vessel diameter changes when a cortical patch of a transgenic mouse is stimulated with light. Minimal optical power levels should ideally be used to avoid inadvertent

thermal damage to cells, and the levels used can be included in the scope of future studies using the system.

7.2 Hemodynamic Signal Monitoring

OCT has sufficient resolution to visualize and quantify blood velocity changes in vessels, as demonstrated with our system, for hemodynamic signal monitoring. However, the limitations of the imaging system for optogenetic experiments should be explored. As mentioned earlier, angiography is predominantly a moving scatterer-dependent imaging technique. While vasculature networks can be imaged, caution should be exercised in its data analysis and interpretation. Angiography is susceptible to errors based on the RBC within the vessel. Vessel diameter measurements, which are angiography-based, may be limited in its sensitivity as a result of factors including undetected regions of the vessel, and changes of RBC orientation. Thus, interpretation of smaller vessel and capillary regions should be more conservative [27].

D-OCT has been shown to quantify velocity in vessels, thus D-OCT techniques were combined with optogenetics to monitor the hemodynamic changes in vessels. However, the technique detects vessels longitudinal to the incident beam, and the minimal resolvable velocity depends on the OCT sampling density. Multiple Doppler angles of the scanning head would be beneficial in capturing the velocity changes in more vessels.

7.3 Studies with Optogenetics and Animal Disease Models

In the future, the system can be used in studies with optogenetic animal disease models of neurological disorders. Optogenetic mouse models, such as epilepsy, have been demonstrated previously [28]. With growing research in optogenetics, more opsin variants are being developed that may contribute to future animal disease models [29]. While, animal models may not accurately portray the complexity of disease pathology in humans, determining disease characteristics in neurological disorders may contribute towards treatments in humans.

Our OCT system, which allows imaging and stimulation simultaneously, holds potential as a tool for circuit mapping towards this goal. Additionally, verification of neural activity and stimulation can be done concurrently with existing imaging methods, or gold standard detection techniques. For example, studies using mouse models of epilepsy can be verified using ECoG, considered the gold standard for neural signal detection. Combining this, with OCT angiography and hemodynamic signal monitoring holds promise in helping researchers characterize cellular activities within the brain hemodynamic changes corresponding to disease models with high resolution and precision in stimulation and imaging.

Works Cited

[1] S. J. Madsen, Optical Methods and Instrumentation in Brain Imaging and Therapy, New York: Springer, 2013.

[2] C. Iadecola, "Neurovascular regulation in the normal brain and in Alzheimer's disease," *Nature Reviews Neuroscience,* vol. 5, no. 5, pp. 347-360, 2004.

[3] R. Pashaie, P. Anikeeva, J. H. Lee, R. Prakash, O. Yizhar, M. Prigge, D. Chander, T. Richner and J. Williams, "Optogenetic Brain Interfaces," *IEEE Reviews in Biomedical Engineering,* In Print.

[4] A. F. Fercher, W. Drexler, C. K. Hitzenberger and T. Lasser, "Optical Coherence Tomography - Principles and Applications," *Reports on Progress in Physics,* vol. 66, no. 2, pp. 239-303, 2003.

[5] M. F. Bear, B. W. Connors and M. A. Paradiso, Neuroscience: Exploring the Brain, Baltimore: Lippincott Williams & Wilkins, 2001.

[6] E. S. Boyden, F. Zhang, E. Bamberg, G. Nagel and K. Deisseroth, "Millisecond-timescale, genetically targeted optical control of neural activity," *Nature Neuroscience,* vol. 8, pp. 1263-1268, 2005.

[7] F. Zhang, M. A. Aravanis, A. Adamantidis, L. d. Lecea and K. Deisseroth, "Circuit-breakers: optical technologies for probing neural signals and systems," *Nature Reviews Neuroscience,* vol. 8, no. 8, pp. 577-81, 2007.

[8] F. Zhang, L.-P. Wang, M. Brauner, J. F. Liewald, K. Kay, N. Watzke, P. G. Wood, E. Bamberg, G. Nagel, A. Gottschalk and K. Deisseroth, "Multimodal fast optical interrogation of neural circuitry," *Nature,* vol. 446, no. 7136, pp. 633-639, 2007.

[9] T. Knöpfel and E. Boyden, Optogenetics: Tools for Controlling and Monitoring Neuronal Activity, Amsterdam: Elsevier, 2012.

[10] "Fluorescence Imaging Filters," Thorlabs, Inc., 2013. [Online]. Available: http://www.thorlabs.com/newgrouppage9.cfm?objectgroup_id=2990&pn=MD515. [Accessed 1 November 2013].

[11] "Basic Concepts in Fluorescence," Molecular Expressions, 8 April 2009. [Online]. Available: http://micro.magnet.fsu.edu/primer/techniques/fluorescence/fluorescenceintro.html. [Accessed 31 October 2013].

[12] W. Drexler and J. G. Fujimoto, Optical Coherence Tomography: Technology and Applications, Berlin: Springer, 2008.

[13] M. E. Brezinski, Optical Coherence Tomography: Principles and Applications, Amsterdam: Academic, 2006.

[14] P. H. Tomlins and R. K. Wang, "Theory, Developments and Applications of Optical Coherence Tomography," *Journal of Physics D: Applied Physics,* vol. 38, no. 15, pp. 2519-535, 2005.

[15] R. Leitgeb, C. K. Hitzenberger and A. F. Fercher, "Performance of fourier domain vs. time domain optical coherence tomography," *Optics Express,* vol. 11, no. 8, pp. 889-94, 2003.

[16] "Beckman Laser Institute & Medical Clinic," University of California-Irvine, [Online]. Available: http://dosi.bli.uci.edu/research/. [Accessed 1 November 2013].

[17] R. Ramaswami and K. N. Sivarajan, Optical Networks: A Practical Perspective, San Francisco: Morgan Kaufmann, 2002.

[18] V. Shidlovski, "Superluminescent Diodes. Short overview of device operation principles and performance parameters," SuperlumDiodes, 2004. [Online]. Available: http://www.superlumdiodes.com/pdf/sld_overview.pdf. [Accessed 1 November 2013].

[19] V. J. Srinivasan, J. Y. Jiang, M. A. Yaseen, H. Radhakrishnan, W. Wu, S. Barry, A. E. Cable and D. A. Boas, "Rapid volumetric angiography of cortical microvasculature with optical coherence tomography," *Optics Letters,* vol. 35, no. 1, pp. 43-45, 2010.

[20] "Extended Broadband SLD Light Source," Thorlabs, Inc., 2013. [Online]. Available: http://www.thorlabs.com/newgrouppage9.cfm?objectgroup_id=1760. [Accessed 1 November 2013].

[21] M. C. Teich, Fundamentals of Photonics, New York: Wiley, 1991.

[22] Wasatch Photonics, Inc., Wasatch Photonics, Inc., [Online]. Available: http://wasatchphotonics.com/wp-content/uploads/2012/02/Specsheet-1145-lmm-1310-nm.pdf. [Accessed 10 10 2013].

[23] Goodrich, Inc. , [Online]. Available: http://www.sensorsinc.com/downloads/SULDH2.pdf. [Accessed 10 10 2013].

[24] J. Lee, V. Srinivasan, H. Radhakrishnan and D. A. Boas, "Motion correction for phase-resolved dynamic optical coherence tomography imaging of rodent cerebral cortex,"

Optics Express, vol. 19, no. 22, pp. 21258-70, 2011.

[25] M. J. Girard, N. G. Strouthidis, C. R. Ethier and J. M. Mari, "Shadow removal and contrast enhancement in optical coherence tomography images of the human optic nerve head," *Investigative Ophthalmology & Visual Science,* vol. 52, no. 10, pp. 7738-748, 2011.

[26] C. A. Schenider, W. S. Rasband and K. W. Eliceiri, "NIH Image to ImageJ: 25 years of image analysis," *Nature Methods 9,* pp. 671-75, 2012.

[27] V. J. Srinivasan, E. T. Mandeville, A. Can, F. Blasi, M. Climov, A. Daneshmand, J. H. Lee, E. Yu, H. Radhakrishnan, E. H. Lo, S. Sakadzic, K. Eikermann-Haerter and C. Ayata, "Multiparametric, Longitudinal Optical Coherence Tomography Imaging Reveals Acute Injury and Chronic Recovery in Experimental Ischemic Stroke," *PLOS ONE,* vol. 8, no. 8, pp. 1-13, 2013.

[28] E. Krook-Magnuson, C. Armstrong, M. Oijala and I. Soltesz, "On-demand optogenetic control of spontaneous seizures in temporal lobe epilepsy," *Nature Communications,* vol. 4, 2013.

[29] K. M. Tye and K. Deisseroth, "Optogenetic investigation of neural circuits underlying brain disease in animal models," *Nature Reviews Neuroscience,* vol. 13, pp. 251-266, 2012.

[30] V. Gradinaru, K. R. Thompson, F. Zhang, M. Mogri, K. Kay, M. B. Schneider and K. Deisseroth, "Targeting and Readout Strategies for Fast Optical Neural Control In Vitro and In Vivo," *Journal of Neuroscience,* vol. 27, no. 52, pp. 14231-4238, 2007.

[31] V. J. Srinivasan, S. Sakadžić, I. Gorczynska, S. Ruvinskaya, W. Wu, J. G. Fujimoto and D. A. Boas, "Quantitative cerebral blood flow with optical coherence tomograph," *Optics Express,* vol. 18, no. 3, pp. 2477-494, 2010.

[32] N. A. Nassif, B. Cense, B. H. Park, M. C. Pierce, S. H. Yun, B. E. Bouma, G. J. Tearney, T. C. Chen and J. F. de Boer, "In vivo high-resolution video-rate spectral-domain optical coherence tomography of the human retina and optic nerve," *Optics Express,* vol. 12, no. 3, pp. 367-76, 2004.

[33] M. Wojtkowski, V. J. Srinivasan, T. H. Ko, J. G. Fujimoto, A. Kowalczyk and J. S. Duker, "Ultrahigh-resolution, high-speed, Fourier domain optical coherence tomography and methods for dispersion compensation," *Optics Express,* vol. 12, no. 11, pp. 2404-422, 2004.

[34] A. M. Rollins and J. A. Izatt, "Optimal interferometer designs for optical," *Optics Letters,* vol. 24, no. 21, pp. 1484-86, 1999.

[35] J. M. Geary, Introduction to Lens Design: With Practical ZEMAX Examples, Richmond: Willmann-Bell, 2002.

[36] G. Liu, Selected Topics in Optical Coherence Tomography, InTech, 2008.

[37] C. Dorrer, N. Belabas, J.-P. Likforman and M. Joffre, "Spectral resolution and sampling issues in," *Journal of the Optical Society of America B,* vol. 17, no. 10, pp. 1795-1802, 2000.

[38] S. Makita, Y. Hong, M. Yamanari, T. Yatagai and Y. Yasuno, "Optical coherence angiography," *Optics Express,* vol. 14, no. 17, pp. 7821-40, 2006.

[39] R. K. Wang and S. Hurst, "Mapping of cerebro-vascular blood perfusion in mice with skin and skull intact by Optical Micro-AngioGraphy at 1.3μm wavelength," *Optics Express,* vol. 15, no. 18, pp. 11402-412, 2007.

[40] Y. Jia, M. R. Grafe, A. Gruber, N. J. Alkayed and R. K. Wang, "In vivo optical imaging of revascularization after brain trauma in mice," *Microvascular Research,* vol. 81, no. 1, pp. 73-80, 2011.

[41] A. D. Aguirre, Y. Chen, J. G. Fujimoto, L. Ruvinskaya, A. Devor and D. A. Boas, "Depth-resolved imaging of functional activation in the rat cerebral cortex using optical coherence tomography," *Optics Letters,* vol. 31, no. 23, pp. 3459-61, 2006.

[42] J. M. Schmitt, A. Knüttel, M. Yadlowsky and M. A. Eckhaus, "Optical-coherence tomography of a dense tissue: statistics of attenuation and backscattering," *Physics in Medicine and Biology,* vol. 39, no. 10, pp. 1705-20, 1994.

[43] G. Buzsáki, C. A. Anastassiou and C. Koch, "The origin of extracellular fields and currents--EEG, ECoG, LFP and spikes," *Nature Reviews Neuroscience,* vol. 13, no. 6, pp. 407-420, 2012.